

COMPUTER AIDED MODELING OF WRINKLING
AND ITS PREVENTION

A THESIS SUBMITTED TO
THE GRADUATE SCHOOL OF NATURAL AND APPLIED SCIENCES
OF
MIDDLE EAST TECHNICAL UNIVERSITY

BY

MEHMET ALİ PİŞKİN

IN PARTIAL FULFILLMENT OF THE REQUIREMENTS
FOR
THE DEGREE OF MASTER OF SCIENCE
IN
MECHANICAL ENGINEERING

SEPTEMBER 2005

Approval of the Graduate School of Natural and Applied Sciences

Prof. Dr. Canan Özgen
Director

I certify that this thesis satisfies all the requirements as a thesis for the degree of Master of Science.

Prof. Dr. Kemal İder
Head of Department

This is to certify that we have read this thesis and that in our opinion it is fully adequate, in scope and quality, as a thesis for the degree of Master of Science.

Prof. Dr. Bilgin Kaftanoğlu
Supervisor

Examining Committee Members

Prof. Dr. Metin Akkök	(METU,ME) _____
Prof. Dr. Bilgin Kaftanoğlu	(METU,ME) _____
Prof. Dr. Suha Oral	(METU,ME) _____
Prof. Dr. Haluk Darendeliler	(METU,ME) _____
Prof. Dr. Alpay Ankara	(METU,METE) _____

I hereby declare that all information in this document has been obtained and presented in accordance with academic rules and ethical conduct. I also declare that, as required by these rules and conduct, I have fully cited and referenced all material and results that are not original to this work.

Mehmet Ali Pişkin

ABSTRACT

COMPUTER AIDED MODELING OF WRINKLING AND ITS PREVENTION

PİŞKİN, Mehmet Ali

M.S., Department of Mechanical Engineering

Supervisor: Prof. Dr. Bilgin KAFTANOĞLU

September 2005, 111 Pages

Deep-drawing operations are performed widely in industrial applications. It is very important for efficiency to achieve parts with no defects. Wrinkling is a kind of defect caused by stresses in the flange part of the blank during metal forming operations. It is required that the flange of a workpiece in deep drawing operation should deform in its plane without wrinkling otherwise it will impair the quality of the product. To avoid wrinkling appropriate blank-holder force or drawbead can be applied.

In this work, finite element method is used to obtain the wrinkling behavior. A four noded five degree of freedom shell element is formulated. Isotropic elasto-plastic material model with Von Mises yield criterion is used. By using this shell element, the developed code can predict the bending behavior of workpiece besides membrane behavior. Simulations are carried out with four different element sizes and two different shapes (circular and rectangular). The thickness strain and nodal displacement values obtained

are compared with results of a commercial finite element program and results of previously conducted experiments.

Keywords: Wrinkling, Deep Drawing, Sheet Metal Forming, Finite Element Method, Computer Aided Metal Forming.

ÖZ

BURUŞMANIN BİLGİSAYAR DESTEKLİ MODELLENMESİ VE ÖNLENMESİ

PİŞKİN, Mehmet Ali

Yüksek Lisans, Makina Mühendisliği Bölümü

Tez Yöneticisi: Prof. Dr. Bilgin KAFTANOĞLU

Eylül 2005, 111 Sayfa

Derin çekme operasyonları endüstriyel uygulamalarda yaygın olarak kullanılmaktadır. Verimlilik için hatasız parçalar elde etmek çok önemlidir. Buruşma, metal şekillendirme operasyonunda taslağın flanaj bölgesindeki gerilmelerden kaynaklanan bir hata tipidir. Derin çekme operasyonunda iş parçasının flanaj bölgesinin bulunduğu düzlemde deforme olması gerekmektedir. Aksi takdirde, bu elde edilecek ürünün kalitesini düşürücü bir faktör olacaktır. Buruşmaları önlemek için uygun baskı plakası kuvveti ya da pot çemberi kullanılabilir.

Sonlu elemanlar metodu kullanılarak buruşma davranımları elde edilmiştir. Dört nodlu, beş serbestlik derecesine sahip olan bir kabuk elemanı formüle edilmiştir. Von Mises akma kriteri ile izotropik ve elasto-plastik malzeme modeli kullanılmıştır. Geliştirilen yazılım, bu kabuk elemanını kullanarak parçanın membran davranımlarının yanında bükülme davranımlarını da elde edilebilir. Dört farklı eleman boyu ve iki farklı şekil

(yuvarlak ve dikdörtgen) için simülasyonlar yapıldı. Elde edilen kalınlık gerilimleri ve nod deplasmanı sonuçlar ticari bir sonlu eleman programının ve önceden gerçekleştirilmiş deneylerin sonuçlarıyla karşılaştırılmıştır.

Anahtar Kelimeler: Buruşma, Derin Çekme, Metal Levha Şekillendime,
Sonlu Elemanlar Yöntemi, Bilgisayar Destekli Metal
Şekillendirme

To my family and beyonce

ACKNOWLEDGMENTS

I would like to express my deepest gratitude and appreciation to my supervisor Prof. Dr. Bilgin Kaftanoğlu who inspired, encouraged and supported me at all levels of this study.

I sincerely thank to my brother Coşar Pişkin for his great effort on editing, spell check, corrections and motivation.

Finally, my greatest thanks go to my family and beyonce who shaped me with their never-ending patience.

TABLE OF CONTENTS

PLAGIARISM	iii
ABSTRACT	iv
ÖZ	vi
ACKNOWLEDGMENTS	ix
TABLE OF CONTENTS	x
TABLE OF FIGURES	xii
CHAPTER	
1.INTRODUCTION	1
2.SURVEY OF LITERATURE	8
3.OBJECT OF THE PRESENT STUDY	24
4.THEORY	28
4.1 General Approach for Determination of Wrinkling	28
4.2 Displacement Based Finite Element Method	28
4.3 Strain–Displacement Matrix	35
4.4 Matrix Representing Constitutive Relations	42
4.5 Contact Algorithm	47
4.6 Solution Scheme	50
4.7 Comparison of Implicit and Explicit Methods	56

5.THEORETICAL RESULTS	57
5.1 Results for square cup drawing with blank–holder (element size 3 mm)	61
5.2 Results for square cup drawing with blank–holder (element size 2 mm)	63
5.3 Results for square cup drawing with blank–holder (element size 1 mm)	65
5.4 Comparison of square cup drawing with blank holder case with experimental results	67
5.5 Results for circular cup drawing (element size 5 mm)	69
5.6 Results for circular cup drawing (element size 3 mm)	73
5.7 Results for circular cup drawing (element size 2 mm)	77
5.8 Results for circular cup drawing (element size 1 mm)	81
5.9 Results for square cup drawing (element size 3mm)	85
5.10 Results for square cup drawing (element size 2mm)	89
5.11 Results for square cup drawing (element size 1mm)	93
5.12 Comparison of square cup drawing case with experimental results	97
5.13 Simulations with changing blank holder load	99
6.DISCUSSION	101
7.CONCLUSION.....	105
8.SUGGESTIONS FOR FUTURE WORK	106
REFERENCES	107

TABLE OF FIGURES

Figure 1.1 Automotive parts manufactured using sheet metal forming.....	2
Figure 1.2 Several sheet metal forming methods.....	2
Figure 1.3 Deep-drawing.....	3
Figure 1.4 Several defect types in deep-drawing.....	4
Figure 1.5 Sample products manufactured using deep-drawing.....	6
Figure 4.1 Typical elasto-plastic and rigid plastic curves.....	42
Figure 4.2 Point data description of tool surface with global search of contact.....	48
Figure 4.3 A mass–spring–damper system.....	51
Figure 5.1 Die–punch sets for circular and square cup drawing.....	57
Figure 5.2 Deformed shapes at a) 1mm b) 5mm c) 10mm d) 15mm drawing depths.....	62
Figure 5.3 Deformed shapes at a) 1mm b) 5mm c) 10mm d) 15mm drawing depths.....	64
Figure 5.4 Deformed shapes at a) 1mm b) 5mm c) 10mm d) 15mm drawing depths.....	66
Figure 5.5 Thickness strain distribution along line connecting center of blank and midpoint of side at 5 mm drawing depth.....	67
Figure 5.6 Thickness strain distribution along diagonal line at 5 mm drawing depth.....	67
Figure 5.7 Thickness strain distribution along line connecting center of blank and midpoint of side at 10 mm drawing depth.....	68

Figure 5.8 Thickness strain distribution along diagonal line at 10 mm drawing depth	68
Figure 5.9 Orientation of circular blank with element size 5 mm	69
Figure 5.10 Deformed shapes at a) 1mm b) 5mm c) 10mm d) 15mm drawing depths	70
Figure 5.11 Displacement of node 1 in x-direction for 5 mm element size	71
Figure 5.12 Displacement of node 2 in y-direction for 5 mm element size	71
Figure 5.13 Displacement of node 3 in z-direction for 5 mm element size	72
Figure 5.14 Orientation of circular blank with element size 3 mm	73
Figure 5.15 Deformed shapes at a) 1mm b) 5mm c) 10mm d) 15mm drawing depths	74
Figure 5.16 Displacement of node 1 in x-direction for 3 mm element size	75
Figure 5.17 Displacement of node 2 in y-direction for 3 mm element size	75
Figure 5.18 Displacement of node 3 in z-direction for 3 mm element size	76
Figure 5.19 Orientation of circular blank with element size 2 mm	77
Figure 5.20 Deformed shapes at a) 1mm b) 5mm c) 10mm d) 15mm drawing depths	78
Figure 5.21 Displacement of node 1 in x-direction for 2 mm element size	79
Figure 5.22 Displacement of node 2 in y-direction for 2 mm element size	79
Figure 5.23 Displacement of node 3 in z-direction for 2 mm element size	80
Figure 5.24 Orientation of circular blank with element size 1 mm	81
Figure 5.25 Deformed shapes at a) 1mm b) 5mm c) 10mm d) 15mm drawing depths	82
Figure 5.26 Displacement of node 1 in x-direction for 1 mm element size	83
Figure 5.27 Displacement of node 2 in y-direction for 1 mm element size	83

Figure 5.28 Displacement of node 3 in z-direction for 1 mm element size.....	84
Figure 5.29 Orientation of square blank with element size 3 mm.....	85
Figure 5.30 Deformed shapes at a) 1mm b) 5mm c) 10mm d) 15mm drawing depths.....	86
Figure 5.31 Displacement of node 1 in x-direction for 3 mm element size.....	87
Figure 5.32 Displacement of node 2 in y-direction for 3 mm element size.....	87
Figure 5.33 Displacement of node 2 in z-direction for 3 mm element size.....	88
Figure 5.34 Orientation of square blank with element size 2 mm.....	89
Figure 5.35 Deformed shapes at a) 1mm b) 5mm c) 10mm d) 15mm drawing depths.....	90
Figure 5.36 Displacement of node 1 in x-direction for 2 mm element size.....	91
Figure 5.37 Displacement of node 2 in y-direction for 2 mm element size.....	91
Figure 5.38 Displacement of node 2 in z-direction for 2 mm element size.....	92
Figure 5.39 Orientation of square blank with element size 1 mm.....	93
Figure 5.40 Deformed shapes at a) 1mm b) 5mm c) 10mm d) 15mm drawing depths.....	94
Figure 5.41 Displacement of node 1 in x-direction for 1 mm element size.....	95
Figure 5.42 Displacement of node 2 in y-direction for 1 mm element size.....	95
Figure 5.43 Displacement of node 3 in z-direction for 1 mm element size.....	96
Figure 5.44 Thickness strain distribution along line connecting center of blank and midpoint of side at 4 mm drawing depth.....	97
Figure 5.45 Thickness strain distribution along diagonal line at 4 mm drawing depth.....	97
Figure 5.46 Thickness strain distribution along line connecting center of blank and midpoint of side at 10.5 mm drawing depth.....	98

Figure 5.47 Thickness strain distribution along diagonal line at 10.5 mm drawing depth.....98

Figure 5.48 Deformed shapes at 15 mm drawing depth for a) 25kgf b) 50 kgf
c) 100 kgf d) 150 kgf e) 200 kgf f) 215 kgf.....100

CHAPTER 1

INTRODUCTION

In manufacturing, there are four main methods to achieve a product [1]. One of them is casting, in which the molten material is poured into a die. So the product is directly shaped in one step. Complex shapes, however, are hard to produce with this method, sometimes it is impossible. Another method is metal cutting processes. In this method, material is removed from the original piece by machining. In metal cutting, a lot of material is wasted. Besides, there may be some difficulties to achieve a complex shape. Tools must be appropriately selected. Manufacturing can also be done by material addition, such as welding. This type of manufacturing is not applicable to all types of materials. The fourth method is metal forming. There are some advantages of metal forming on other techniques. There is little material wasted in metal forming. Also, very complex shapes can be achieved and the material strength is improved. The disadvantage of metal forming, however, is that several steps may be required to achieve the final product.

There are methods in metal forming: direct and indirect extrusion, drawing of tubes and wires, rolling, forging, deep-drawing, etc... Most of these methods are widely used in industry. These methods can be used to manufacture a wide range of products. For example, extrusion can be used to manufacture complex shapes from a block of material. Using a mandrel, a tube can also be produced by forward extrusion. Rolling can be used to produce sheet metal.

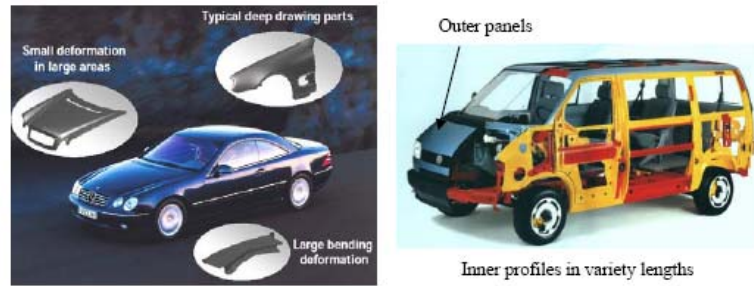


Figure 1.1 Automotive parts manufactured using sheet metal forming

Deep-drawing is a metal forming method, which is used to manufacture products from sheet metal. It is a very common method in the industry for the applications requiring sheet metal. Very complex shapes can be achieved using deep-drawing. Deep-drawing is used to produce many different products, such as automotive parts, cans, sinks, housing, etc... The application areas are getting larger everyday. Besides, the needs of current applications are changing. For example, in automotive industry, general trend is to use thinner metals and some polymers. Therefore, it is very important to continue the researches in this area to make the deep-drawing process capable of satisfying these new needs.

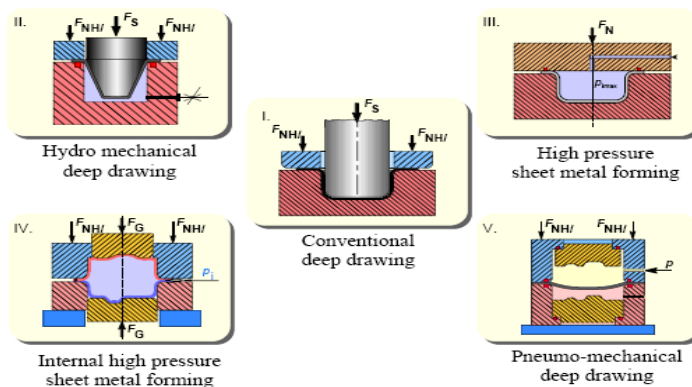


Figure 1.2 Several sheet metal forming methods

In the deep-drawing process, a blank is placed on a die. A punch is used to draw the blank. Almost in every application, a blank-holder is used. These are the basic tools of deep-drawing. Selection of appropriate tools is a very important point for the success of the process. The shape of the final product directly depends on the shape of punch and die. The corner radii of die and punch have an important effect on the process. For example, punch load increases with sharper die corner radius.

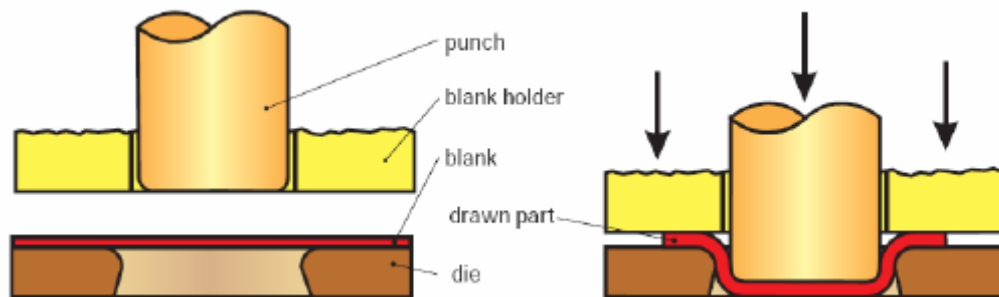


Figure 1.3 Deep-drawing

Deep-drawing process must be investigated in five parts for five different regions. The explanation of what happens in which region is as follows:

➤ The region between the die and the blank-holder is called as the flange region. This region covers the part from the rim to the start of die curvature. In this region pure radial drawing occurs. There is a circumferential compressive stress and a radial tensile stress state in this region. This is the only region that the material gets thicker.

➤ Over the die profile, sliding and bending of the material occurs. In this region, in the radial direction tensile stresses occurs, whereas compressive stress is observed in the circumferential direction. As mentioned above, radius of the curvature of die profile has effect on the punch load. For a sharper radius, more plastic bending work is done, therefore the punch load increases. In this region, material gets thinner due to bending under tensile stresses in the radial direction.

➤ In the region between die and punch, generally there is no contact of the material with either of punch and die. This is a transition region between die and punch. In this region radial tensile stresses act on the material. Material gets thinner and tearing or necking can take place in this region.

➤ Bending and sliding of the material takes place over the punch profile. As the radius of die corner is, radius of punch profile is an important parameter for deep-drawing. Selection of this radius can cause or prevent necking and tearing of material in this region. Again thinning of material takes place. Biaxial tensile stresses act in this region.

➤ Over the punch head, sliding and stretching of the material occurs. In this region, thinning of the material occurs. The limiting drawing ratio (LDR) depends on the load carrying capacity of this region. The maximum load carrying capacity is determined by the plastic instability taking place in this region. However, plastic instability depends on the friction properties between the punch and material. Equ-biaxial tensile stresses act in this region.

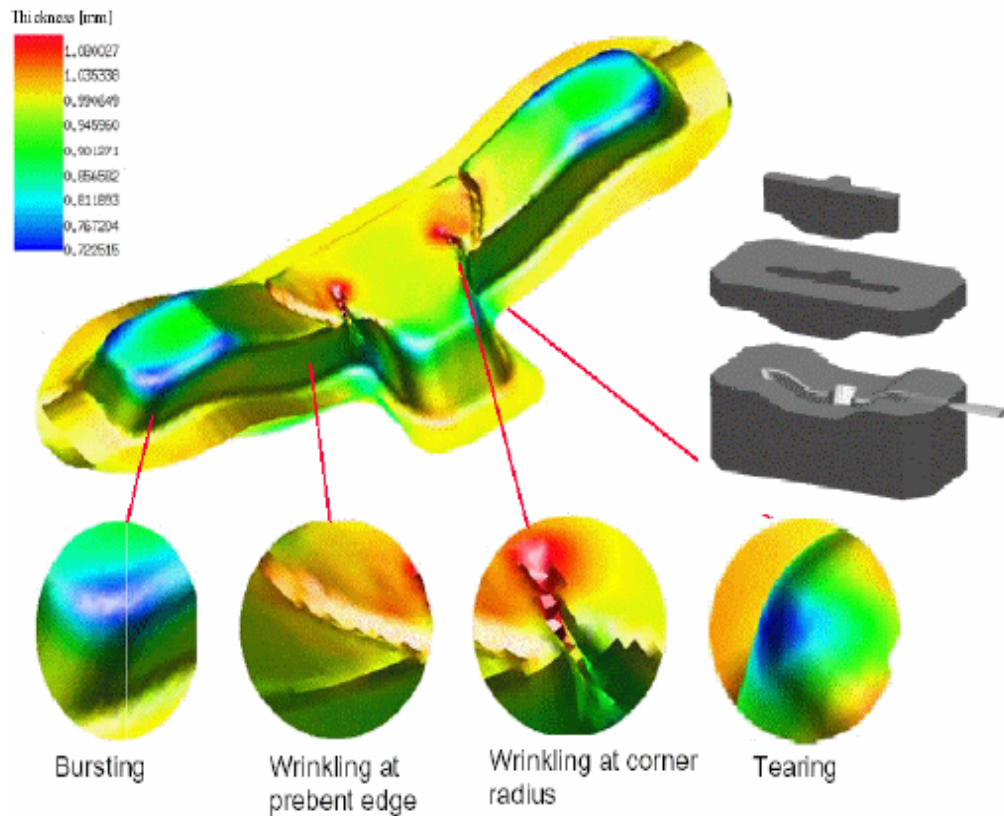


Figure 1.4 Several defect types in deep-drawing

As described above, there are several failure types in a deep-drawing operation. Different failures occur in different regions. As stated above, necking and tearing generally occur over the punch head and punch profile and between punch and die. In flange region, however, a different failure type, wrinkling, can be observed. On a completely drawn part, earing can also be seen on the walls of the cup due to planar plastic anisotropy.

Tearing and necking are caused by the tensile stresses and they are types of tensile instabilities. Wrinkling, however, differs from these failure types. Wrinkling, occurring in the flange region, takes place under pure radial drawing. As stated above, there is a circumferential compressive stress state in the flange region. When the radial drawing stress exceeds a certain value,

compressive stress in the circumferential direction becomes too high, so plastic buckling occurs. This plastic buckling gives a material a wavy shape.



Figure 1.5 Sample products manufactured using deep drawing

Wrinkling is an undesired deformation, so it must be prevented. There are two different approaches for prevention of wrinkling. The first one is using blank-holder. In this approach, a flat tool set is used to prevent the collapse of the material into waves. Two types of blank-holding application exist: clearance type blank-holders, pressure type blank-holders. In clearance blank-holding, the clearance between the blank-holder and the die is kept at a constant value. Therefore, the material is kept at a constant thickness, and the wave development is prevented. This can be assumed as a plane strain

case. In pressure type blank-holding, some mechanism is used to arrange the clearance between blank-holder and die, so as the material gets thicker, blank-holder plate can move freely to supply necessary space for thickness of material. The force needed to prevent wrinkling is calculated and applied with the blank-holder plate to the material. So wrinkling is prevented, whereas the material is able to get thicker. Neglecting the blank-holder force, this case can be assumed as a plane-stress problem.

Second way of prevention of wrinkling is using drawbeads. In drawbead applications, material is forced to flow through a groove with the help of the male of the groove on the blank-holder. When material moves through the groove, compressive stresses decrease because of the tensile forces acting. So wrinkling is prevented by reducing the compressive stresses below the critical value.

Prediction of wrinkling is a very important process for a deep-drawing operation. Knowing if the part wrinkles or not, completely affects the selection of tools used in manufacturing. Unnecessary precautions taken can bring undesired results. For example, using blank-holder increases the punch load. In total, expenses of process may increase. On the other hand, if wrinkling cannot be predicted, precautions cannot be taken, so product quality decreases, and mostly, produced parts becomes unacceptable. So the designer should know about the wrinkling behavior of a given blank.

CHAPTER 2

SURVEY OF LITERATURE

A survey of previous work held on sheet metal forming and especially wrinkling in deep drawing is presented. Besides the researches on those areas, studies on solution methods like finite element method is investigated. The researches started very early in both areas, especially in sheet metal forming, in history, but work on wrinkling is seen to be done mostly in recent years. This is because as sheet metal types used in industry become thinner, wrinkling appears as a primary problem, the need for research on this area increases. In this chapter, these researches are revised.

Kaftanoğlu [2] developed a method for flange wrinkling in axisymmetrical deep drawing using the energy method. In this approach, wrinkling occurs if the plastic work done for deep drawing is higher than the plastic work done for wrinkling. For this purpose, using von Mises yield criteria, a plastic analysis is done for the flange part of the blank, assuming plane stress conditions. For the calculation of work done for wrinkling, wrinkles are assumed to be a sine curve in shape. So the amplitude of the wrinkles are calculated, then using the plastic bending moment, work done for wrinkling is obtained. Using these procedures, plastic work versus reduction strain curves are obtained for both deep drawing and wrinkling. When the slope of the wrinkling curve is greater than deep drawing curve, wrinkling does not occur, since the energy required is greater than deep drawing. Considering the peaks of the wrinkles as plastic hinges, the blank-holder force needed to suppress wrinkling is found in terms of wave number. Experiments are conducted to verify the numerical results with several

materials and for several initial blank diameters. Experimental results are in very good agreement with numerical results.

Ramaekers et al. [3], made a research on the deep drawability of a round cylindrical cup. The limiting drawing ratio is tried to be related with some process parameters like anisotropy factor, strain hardening exponent, etc... Upper and lower bound methods are used to obtain theoretical models. Using the theoretical model proposed for deep drawing, estimation for the limiting drawing ratio is tried to be achieved. Some experiments are conducted to verify the model developed. Comparing the results, it is seen that an agreement between the model for deep drawing and experiments. However, a precise prediction of the limiting drawing ratio could not be achieved. The friction coefficient is seen to be an important factor for the drawability of large size products. The study showed that decreasing friction coefficient, increases limiting drawing ratio.

Kang and Im [4], in 1997, proposed an iterative scheme for finite element analysis of wrinkling for anisotropic and isotropic flexible membranes or fabric structures. They formulate a wrinkling criterion using the one developed by Roddeman et al. based on the principal stresses and strains. Wrinkling initiation is predicted by comparing the second Piola–Kirchoff stress and Green Lagrangian strain. They developed a finite element code by just applying minor differences to the existing total Lagrangian codes for membranes. Numerical examples for torsion of a membrane and quasi–static inflation of an automobile airbag are performed.

Cao and Boyce [5] examined wrinkling and tearing type of failures in sheet metal forming. For prediction of wrinkling, they used a method proposed by Cao and Boyce. The criterion is based on the energy conservation and minimum work to suppress the wrinkling. Total strain energy values for a perfect plate and for buckling plate are recorded. Then

the force/pressure needed to suppress the wrinkling is calculated using the energy difference and wrinkling amplitude. In prediction of tearing, existing forming limit diagrams are used in correspondence with the local strain histories near possible tearing regions. They also developed a technique named variable binder force in which blank–holding load varies in controlled manner, not a constant blank–holding load was used. A control algorithm is proposed for variable binder force technology. Two examples are used: conical cup drawing and square cup drawing. Finite element models of both cases are analyzed by commercial program ABACUS. Comparison with the experimental results shows that the method is capable of predicting wrinkling and tearing. The control algorithm for variable binder force is tried in both cases, and 16% extra cup forming height is provided for conical cup drawing.

Yang et al. [6] searched a way to predict the initial blank shape for an operation without fracture and wrinkling. A two stage method is proposed for optimum blank design. In the first stage, they used ideal forming theory, developed by Chung and Richmond, to make an initial estimate for the blank shape. The internal plastic work is calculated using the effective stress and effective strain that is defined using Hill's theory. Then this work is optimized in the initial blank stage, so the optimum blank shape is obtained. However, friction forces, blank–holding force, lubrication, etc. are not considered, so the blank shape is not finalized in this stage. In second stage, using the obtained blank shape, a deformed shape is calculated with finite element analysis. As the initial shape is not completely true, there are some shape errors in the deformed shape. Using a deformation path iteration method, shape errors are tried to be minimized to achieve the optimum blank shape. The finite element code used is developed by Yang et al. A square cup drawing is used to obtain some numerical results. It is shown that after two modifications to the blank shape obtained by ideal forming theory, the deformed shape almost completely matches with the target shape.

Cao [7], in 1999, developed a method for the prediction of wrinkling using the energy method. In this method, wrinkling criterion proposed by Cao and Boyle [5] is used. This criterion assumes that the initiation of wrinkling is a local phenomenon and depends on the material properties, stress state and sheet thickness. Therefore, the flange wrinkling problem in deep drawing is reduced to the wrinkling problem in a rectangular plate. Then, as stated above, using the energy difference, the binder pressure is determined. Cao, proposed an analytical model for flange wrinkling to calculate the energy values, instead of calculating them by experimental means (using strain histories) or finite element analyses. The material is modeled as planar isotropic. Calculating the energy values with the help of this analytical model, binder pressure is given by previously developed wrinkling criterion. Then analytical model for side wall wrinkling is also developed. Results obtained using analytical model for flange wrinkling are compared with the numerical results of the previous work, which were validated by experiments. There is a good agreement between analytical and numerical results, especially in the prediction of critical buckling stress. Experiments held for side wall wrinkling show that cup forming height prediction of the analytical solution is excellent.

Rosochowski et al [8] simulated the wrinkling behavior in deep drawing of conical cups. In this research, a comparison is made between the static–explicit and dynamic–explicit finite element analyses. For the simulations, commercial finite element programs are used. For static–explicit analysis ITAS3D is chosen, whereas for dynamic–explicit analysis ABAQUS/Explicit is preferred. As this is a comparative study, the simulation parameters are tried to be chosen similar, e.g. using the same finite element mesh. However, because of the differences between approaches and between the programs, there are some parameters that do not match exactly, e.g. properties of elements. The simulations are held for different parameters. It is seen that there are quite important differences between the results of two approaches. The number and location of the wrinkles are different for two programs. Actually the results with different parameters for

the same program don't match. Changing the mesh, e.g. number of elements, changes the results drastically. With ITAS3D, with one of the meshes used, wrinkling doesn't occur. Experiments are also made to verify the results of both programs. The number, distribution and shape of the wrinkles, don't match with the experimental results for both programs.

In 2001, Yang et al. [9, 22] analyzed the wrinkling behavior of the deep drawing of an elliptical and circular cup using finite element analysis. Bifurcation theory is introduced for the finite element analysis. Finite element formulation is based on the incremental deformation theory and elastic-plastic material modeling. The stiffness matrix vanishes at the initiation of wrinkling. Wrinkling behavior is analyzed by the introduction of the continuation method, proposed by Riks, into the elastic-plastic finite element method. A two-face-contact scheme and blank-holder control algorithm are employed. Five analyses are performed for different parameters, for elliptical cup drawing. The changing parameter is the minor axis length of the ellipse. So the aspect ratio is able to be investigated. In two of these analyses wrinkling took place. It is seen that wrinkling is severe near the major axis. Analyses show that with the increasing aspect ratio, fracture takes place before the wrinkling initiates. For cylindrical cup drawing process, several experiments are conducted for different blank-holder forces. It is shown that, mesh is effective on the analysis. Effects of material properties and friction are also observed. Authors stated that, results are in good agreement with experimental data considering the difficulties and sensitivity of the wrinkling analysis.

El-Morsy et al. [10] analyzed the warm deep drawing of magnesium alloys. Two models are used to search the effect of heat transfer on drawability. In the first model, punch is assumed to be at room temperature, whereas blank-holder and die are heated to 573 K. The blank is at room temperature initially. So heat transfer occurs among die, blank, blank-holder and punch. In the second model, however, besides die and blank-holder,

punch and blank is also at 573 K, therefore no heat transfer takes place. Two different punch speeds are used to investigate the effect of punch speed on the temperature distribution. In finite element modeling, a circular blank is generated using 4 node 2 dimensions quadrilateral axisymmetric elements in two layers, and blank is generated using shell elements. Die and punch are modeled as rigid surfaces. It is seen that in the first model, localized thinning occurs in the early stages of the process. In the second model, however, blank is drawn successfully. The cup resultant height is greater in the second model. So the effect of heat transfer on deep drawability of magnesium alloys seems to be in positive way. Comparing two punch speeds, with the lower punch speed a cup with a greater height is obtained. This is concluded that more heat transfer can occur with a lower punch speed. No experiments are conducted to verify the numerical results.

Deshpande and Nalawade [11] developed a program for the analysis of deep drawing of cylindrical cups. The analysis is based on the slab method. The model takes into account the effect of bending and unbending, thickness change, and friction. Strain hardening is considered for the modeling of material, but anisotropy is neglected. Experiments are conducted with pure aluminum blanks to compare the outputs of the program with empirical data. The program can calculate the stress–strain distribution in several regions, and can plot the punch load and punch travel diagram. Radial stress distributions are compared with results of Woo (1964), and seem to match almost completely. The maximum punch load against punch travel output deviates less than 10% from the results of experiment, and with increasing blank diameter deviation decreases drastically. These outputs are also compared with the finite element analysis of Huang and Chen (1996), and the results match.

Alves et al. [12] studied the effect of mesh refinement on the prediction of wrinkling and earring. In the simulations, circular blanks of 1 mm thickness and 90 mm radius for aluminum alloy and 105 mm radius for mild

steel are drawn. In this study 8 node elements are used. Four different in-plane mesh refinements are applied. These refinements are based on the die profile radius, element size to die radius ratios of 1.00, 0.75, 0.50, 0.25 are chosen. Also, all refinement schemes are carried out with 1, 2 and 3 layers of finite elements. For the earing profile, number of layers has negligible effects. However, the earing profile highly depends on the refinement. The radius of the outer profile decreases about 10% when finite element ratio decreases from 1.00 to 0.25. In wrinkling prediction, authors concluded that mesh refinement must be better than the earing profile simulation.

Cho and Yang [13] proposed a mesh refinement algorithm for sheet metal forming analysis. In opposite to traditional mesh refinement algorithms, no transition elements are produced, so higher accuracy is able to be achieved. In the simulations triangular shell elements are used. Comparing with traditional algorithms, no sudden increase in mesh number occurs in this scheme. This reduces the computational time.

Selman et al. [14] studied the adaptive mesh refinement in prediction of wrinkling. In this work, the analysis of Hutchinson (1985) and its extension by Neale (1989) is used. However, as Hutchinson's approach is limited to contact free wrinkling, a new method is proposed by the authors for wrinkling with contact (geometric wrinkling indicator). For the error estimation, the study presented by Bonet (1994) is applied. Simulations of production of a hemispherical cup are performed for both contact free wrinkling using Hutchinson's approach and wrinkling with contact using geometric wrinkling indicator. It is concluded that usage of an adaptive mesh refinement is necessary for decreasing the computational time, however, for proper approximation of the curvatures and thickness, an error estimation routine must be applied.

Lejeune et al. [15] studied on the prediction of wrinkling in metal forming. A theory is developed based on the formulation of Nordlund and Häggblad. In this approach wrinkling is characterized by strong local out of plane rotations. Then the developed theory is implemented in the finite element code. To calculate the incremental deformations, updated Lagrangian formulation is used. In this work LMARC is used as a finite element program. To show the validity of the theory, Yoshida Buckling Test is simulated by the finite element code. Besides, simulations of stamping process are performed for wrinkling prediction in metal forming operations. Numerical results obtained for all simulations are not satisfactory. Some predictions are done by the authors for the reasons of such results, and it is told that a new criterion is being studied by the authors considering the problems of this theory.

Nakamura et al. [16] studied the optimum design of drawbead in sheet metal forming using finite element method and descritized optimization methods. Response surface method is used to increase optimizing efficiency. Parameters for this design procedure are chosen as bead length and bead position. A dynamic explicit finite element code using an updated Lagrangian formulation is used. Blank is modeled using shell elements. For material modeling, elasto–plastic behavior is chosen, where strain hardening is taken into account according to Swift’s law. Experiments are conducted for the verification of the results of numerical analysis. A rectangular and stepped cup production is simulated and experimentally carried out. It is concluded that as the bead length increases, the material becomes more resistive, and wrinkling tendency decreases. With the increasing bead length, however, the strains become larger and thickness decreases. Comparing with experimental results, it is seen that the developed system can determine the suitable bead design.

Weili et al. [17] proposed a simplified method for the simulation of wrinkling. Based on a study about contact algorithm by the authors, later

steps of the contact algorithm such as modification of node position and implementation of the boundary conditions are presented. In stead of applying a blank–holder force, blank–holder gap is used. To verify the results of simulation, for processes are simulated and corresponding experiments are conducted: square cup drawing, drawing of hemispherical part, drawing of a cylindrical cup and production of a real auto panel, rear–side frame. For these examples, medium carbon steel is chosen as blank material. No initial imperfection is applied. Comparing the results of experiments with the numerical results, they seem to be in agreement. Authors concluded that, the presented method could reflect the wrinkling behavior successfully.

Cao and Wang [18] presented an analytical model for plate wrinkling under tri–axial loading. The model is based on the wrinkling criterion developed by Cao and Boyce formerly. However, Cao and Boyce used their criterion combined with the finite element method, whereas Cao and Wang used the criterion in an analytical approach. The critical buckling stress and wavelength are treated as functions of normal pressure. The stress and wavelength are calculated combining the energy conservation and plastic bending theory. The obtained results match with the results of Cao and Boyce’s numerical approach. Results are also in agreement with experimental data of conical cup drawing and square cup drawing. When compared according to computational time, the analytical method has a very important advantage over the numerical method. Numerical computation requires more than two hours, where less than one second is enough for the analytical method to find the same results using the same parameters and same computer. Therefore computational cost becomes very low compared to finite element analysis.

Chu and Xu [19] studied on the elastoplastic analysis of flange wrinkling in deep drawing. Flange wrinkling is considered as a bifurcation problem. Analysis of a circular cup drawing process is performed. The anisotropy effect is taken into account modeling the material. Flange is

modeled as an annular plate. A radial stress is applied from the inner edge of the plate. For the critical drawing stress, a closed form solution is developed based on the plastic deformation theory and nonlinear plastic stress field. The results are compared with those of Senior's one dimensional theory (1956). No experiments are conducted, however experimental results obtained by Senior are considered. Considering the critical stress, presented theory predicts higher values than Senior's. However, these values are closer to the experimental values of Senior. Same behavior is obtained when number of wrinkles is compared. The theory developed by authors gives a higher number of wrinkles, which fits better with the experimental data. It is stated that critical drawing stress value depends on the shear stress applied on the flange. Neglecting the shear stress, results with the underestimation of the critical drawing stress.

Zeng and Mahdavian [20] investigated the wrinkling behavior in deep drawing at elevated temperatures and compared with cold forming operation. Wrinkling criteria was developed using the equality of moments: When buckling moment becomes equal to total of the restraint moments (restraint moments due to blank-holder force and at die radius, and moment due to resistance of the metal to bending, induced in the metal itself) wrinkling occurs. The analysis was made for two cases – with and without using blank-holder. Experiments were conducted at both ambient temperature and elevated temperature for the verification of the theoretical results. Considering the case without blank-holder, number of wrinkles depends only on the drawing geometry, with increasing temperature number of wrinkles remain same. The results of experiments are in agreement with theoretical results. When blank-holder used, however, number of wrinkles are no more independent from temperature. Increasing temperature, increases number of wrinkles formed. The agreement between theoretical and experimental results is satisfactory, again.

Morimoto and Nakamachi [22], developed a technique for the elastic/crystalline viscoplastic finite element analysis of deep drawing process. In this work, the approach to determine the yield function indirectly is not used. Instead, crystalline plasticity theory is applied. Constitutive equations are presented for the construction of an elastic/crystalline viscoplastic model. 8-node 3 dimensional elements are used. The results are in agreement with the conducted tensile tests, to compare the mechanical behavior of the material with obtained results of analysis.

Nordlund and Häggblad [23] presented an algorithm for the prediction of wrinkle tendencies in the early stages of the computations of explicit sheet metal forming simulations. To find the initiation of wrinkling, local value of the second order increment of internal work is used. The procedure is applied only for explicit scheme, but it is told that it can also be used with an implicit technique. Authors stated that the wrinkling indicator presented can work for both unperturbed structures and structures with perturbation, so it is not limited to bifurcation type of wrinkles. Material model, loading conditions and contact conditions are not effective on the work of the algorithm. To simulations are performed to demonstrate the performance of the procedure: Yoshida buckling test and fluid forming of a cup. No experiments are conducted for the verification of the results of numerical analysis, so it is not obvious if results are satisfactory compared to a real application.

Yang et al. [24] investigated the effect of anisotropy on wrinkling in sheet metal forming. Using the bifurcation theory, finite element analysis was applied for this study. Continuum based resultant shell elements considering the anisotropy were used for modeling. Post-bifurcation behavior was analyzed, after finding the instability limit by incremental analysis. Material was modeled with elastic-plastic behavior. For the investigation of effect of anisotropy on wrinkling, a square plate subjected to biaxial stress (compression in one direction and tension in other direction) was simulated for various different anisotropy parameters. According to the results of this

simulation, it was seen that tendency for plastic buckling of the sheet metal decreases with the increase in the normal anisotropy value. No experiments are carried out.

Wang and Cao [25] proposed a method to predict the side wall wrinkling in sheet metal forming processes. Analytical approach was combined with finite element method. A modified energy approach was used to present a wrinkling criterion. Critical buckling stress was calculated as a function of material properties, geometry parameters and current in-plane stress ratio, using the analytical model. The wrinkling initiation can then be assessed by comparing the calculated critical stress values with the compressive stress values obtained from finite element analysis. For the verification of the results of proposed method, experimental data from Yoshida buckling test, aluminum square cup forming and aluminum cup forming were collected. The predicted values showed excellent agreement with the experimental values. The method does not take into account the friction.

Cao and Boyce [26] investigated the elastic and elastic-plastic sheet subjected to edge compression and lateral constraints. Using energy conservation in correlation with finite element method, a wrinkling criterion was established. Initial imperfections are used for finite element analysis. By the presented approach, the need for refined meshes can be overcome as the critical buckling stress can be calculated as a function of applied normal pressure, simply maintaining the required binder pressure depending on the compressive state. A sensitivity study for the imperfection is conducted also. Simulations showed that they are sensitive to imperfections. Sensitivity to geometric imperfection was more than the material imperfection. The simulations were found to be able to predict the correct buckling mode and stress.

Correia and Ferron [27] developed a bifurcation analysis to predict the wrinkling behavior in deep drawing processes of anisotropic sheet metals. Based on a local analysis, wrinkling limit curves were obtained which depend on the material anisotropy and local geometry. For the verification of the analysis, finite element simulation of a conical cup drawing process was performed. Number of wrinkles, critical stress levels and wavelengths of wrinkles were predicted by bifurcation analysis, and these predictions match well with the results of finite element analysis for transverse isotropic materials. With the increasing anisotropy, critical stress level slightly decreases. The effect of anisotropy on stress state and sheet curvature developed on the walls was more important. Authors concluded that for increasing anisotropy, initiation of wrinkling was expected to be seen for larger punch strokes.

Wang et al. [28] performed a wrinkling analysis in shrink flanging. The analysis is simplified as buckling of a curved sheet. A stress based wrinkling criterion is developed using the energy approach. The critical buckling stress was calculated as a function of material properties and geometric properties. Some experiments were performed for the verification of the theory. The predictions of the presented approach seemed to be in good agreement with experimental results. It is found that number of waves decreases with the increase in flange length.

Hemitian and Wild [29] investigated the effect of tooling imperfection on the initiation of wrinkling in deep drawing of thick sheets. Two types of tooling imperfections were considered: punch displacement, which is the linear misalignment of the punch and die, and blank tilting, which is the angular misalignment of the blank. Finite element simulation was carried out for this analysis. In this research, commercial finite element analysis program MARC was used. 4-node thick shell elements were used in the model. The entire 360° of the blank were developed for the model not to prevent the nonsymmetrical wrinkles. Considering the results of simulations, it was

concluded that the displacement of the punch has a negligible effect on the wrinkling initiation, without using a blank-holder. Blank tilting, however, was found to be an important parameter for the wrinkling behavior of thick sheet blank.

Xiong and Xiu [30] studied the compressive instability in sheet metal forming. An energy method was proposed for the analysis. The work done by the internal force in plastic bending was presented. Some simplifications were made considering the geometry of the wave in the analysis of flange buckling. Before the wrinkling occurs, half wave is assumed to be a rectangular plate, whereas after wrinkling, wrinkle is simplified to a sine wave. Results of the presented theory were compared with the experimental results of Wang (1990). A satisfactory agreement was found between them. The buckling of a shell in cup deep drawing process through a conical die was also analyzed. A comparison was made between the theoretical results and experimental data of Sowerby et al. (1982). Again the results match with the experiments.

Lee and Cao [31] proposed a shell element formulation for multi-step inverse analysis. The developed algorithm was applied to the analysis of deep drawing process of both thin sheets and relatively thick sheets. Two numerical examples were carried out, one with a thin sheet, the other with a thick sheet. No experiments were conducted, instead, incremental finite element simulations were performed using the commercial program ABAQUS using shell and solid elements. These simulations were considered as experiments, and were used to verify the results of the presented numerical method. Also, comparison with the older inverse analysis results in literature was carried out. It is seen that more accurate results were achieved with this method. Old methods generally use membrane elements, so the new algorithm has the advantage of considering the bending and unbending effects. Accurate initial blank size and strain distribution were provided.

Evangelista et al. [32] introduced a modification of the Marciniak–Kuczynski method for deep drawing process. Finite element method was used for this study. The developed method was simulated by finite element analysis of a round cup and a square cup. Predictions of forming limit diagrams considering the necking criterion were also done. Little deviations were seen between the predicted diagrams and the diagrams in the literature. No experiments were conducted or no comparisons made with previous work for the validation of the method for round and square cup drawing.

Cao et al. [33] studied on the buckling of sheet metals subjected to controlled boundary conditions. A wedge strip test was designed to observe the wrinkling behavior of sheet under various boundary constraints. With easy change of boundary conditions, different buckling modes were able to achieve. Three different boundary constraints were applied. The results were compared with the numerical results of Cao and Wang [24], which was obtained by using energy approach and finite element method in combination. Results were in good agreement with each other.

Yang et al. [34] presented a method for shell elements to consider the thickness stress caused by contact to improve the solution accuracy. The yield criterion generally used with shell elements based on the plane stress condition was modified to include the effect of transverse stress. The algorithm was applied to bilinear 4–node quadrilateral shell elements. Uniaxial compression, biaxial tension, bending and stretching of a sheet and cylindrical cup drawing were simulated. A dynamic explicit code was used in the simulations, which was generated only for sheet metal forming by Chung et al. (1999). Instead of carrying out experiments, obtained results were compared with the numerical solutions of commercial program ABAQUS, which has static implicit code, using continuum elements. Almost same efficiency was obtained with the commercial program. It was also shown that

in prediction of wrinkling and forming limit diagrams, considering the thickness stress is an important factor.

CHAPTER 3

OBJECT OF THE PRESENT STUDY

The deep drawing process is applied with the intention of manufacturing a product with a desired shape and no failures. The final product shape after deep drawing is defined by the tools, the blank and the process parameters. An incorrect design of the tools and blank shape or an incorrect choice of material and process parameters can yield a product with a deviating shape or with failures. A deviating shape is caused by elastic springback after forming and retracting the tools. The most frequent types of failure are wrinkling, necking (and subsequently tearing), scratching and orange peel.

Without extensive knowledge of the influences of all these variables on the deep drawing process, it is hardly possible to design the tools adequately and make a proper choice of blank material and lubricant to manufacture a product with the desired shape and performance. As a result, after the first design of the tools and choice of blank material and lubricant, an extensive and time consuming trial and error process is started to determine the proper tool design and all other variables, leading to the desired product. This trial and error process can yield an unnecessary number of deep drawing strokes, or may even require redesigning the expensive tools. To reduce this waste of time and cost, process modeling for computer simulation can be used to replace the experimental trial and error process by a virtual trial and error process.

The prime objective of an analysis is to assist in the design of a product. To design or select the tools and the equipment, such design essentially consists of

- predicting the material flow,
- determining whether it is possible to form the part without surface or internal defects,
- predicting the forces and stresses necessary to execute the forming operation.

Wrinkling is a common mode of failure in sheet-metal forming. It may occur in any stage of a forming process depending on many factors such as blank geometry and holding conditions, punch and die face geometry, tool sheet interface friction and lubrication, material properties and thickness. In press forming of large sized parts such as automobile panels, wrinkles are likely to develop before failures appear. This surface defect is unacceptable in finished components for functional or visual reasons.

Most of the previous work on wrinkling was performed for axisymmetrical parts and analytical solution methods for maximum of two dimensions were applied. There is a small number of works for antisymmetric workpieces, which applied finite element method for the solution. The effects of blank holder force and drawbeads were not taken into account. Also by the application of bifurcation analysis only the initial mode of wrinkle but not its permanent shape after wrinkling was obtained by the previous finite element solutions of nonaxisymmetrical problems.

In this work, wrinkling problem occurring in the flange region in sheet-metal forming operations is going to be considered. Finite element method

based on energy formulation will be used for the derivation. Unlike previous studies a general approach that includes nonaxisymmetric parts will be considered. Nonlinear work hardening material model is going to be used to represent the deformation characteristics of the part. Frictional effects occurring between the die and the blank are also going to be considered.

In the flange region there are two possible modes of deformation; drawing and wrinkling. Bending effect is considered as the cause of wrinkling. In finite element formulation a shell element which is capable of considering drawing and wrinkling modes of deformation is going to be formulated. As the result of the analysis, the deformed, wrinkled shape of the workpiece is going to be obtained. The agreement between theory and the experimental results is also going to be tested.

The present study focuses on the following aspects:

- The consideration of a general theory
- Application of finite element method to obtain a general solution method that is applicable to any kind of geometries (axysymmetric or nonaxysymmetric)
- Consideration of shell assumptions to obtain the effect of bending behavior
- Solution with and without blank holder force application
- Obtaining theoretical blank–holder force needed for the workpiece to prevent wrinkling

As a conclusion, this study is based on explicit formulation of time step integration. An explicit finite element code is generated Axisymmetric and non-axisymmetric blanks are defined by using quadrilateral shell elements with 4 nodes and 5 d.o.f s at each node. Dynamic equilibrium equations with the given boundary conditions are constructed. Gaussian quadrature is applied to calculate the integrals numerically. Isotropic elastoplastic material model with Von Mises yield criterion is used. Updated Lagrangian formulation is adopted to calculate displacements. Stresses are related with strains by constitutive laws. Contact algorithm is developed using penalty function method. The analysis is made for deep drawing of square, rectangular, and circular cups with the blank-holder. Results are compared with the available experiments

In Chapter 2, survey of previous work on deep-drawing operations considering wrinkling are already presented. The numerical procedures and finite element analysis tools used in this subject are also searched, and presented in the same chapter.

In Chapter 4, finite element method procedure is described, which is used to analyze the wrinkling problem and the numerical methods to solve the stiffness equations of finite element method are presented.

In Chapter 5, comparison of the experimental results and numerically obtained results is made. The discussion of the results is presented in Chapter 6.

In Chapter 7, conclusions of the whole work are presented. In Chapter 8, suggestions are offered for future researches in this area.

CHAPTER 4

THEORY OF FINITE ELEMENT METHOD

4.1 General Approach for Determination of Wrinkling

There are so many different theories developed for both deep drawing analysis and wrinkling phenomenon. There are very different approaches to analyze the behavior of material during deformation process. These different approaches are presented in the previous chapters.

In this study, for the analysis of wrinkling, the work of Kaftanoğlu [1] was chosen as the basis, which uses the energy approach. Determination of whether wrinkling occurs or not is carried out by calculating the energy of the deep drawing and wrinkling, then comparing the calculated energy values. If the energy of the deep drawing is larger than the energy required for wrinkling, work piece tends to wrinkle. The approach explained above is implemented in a finite element solution.

4.2 Displacement Based Finite Element Method

There are several different techniques applied in finite element method. Most of these techniques use an energy balance. This is the requirement of the law of conservation of energy. According to this law, it can be said that the work done by the external forces must be equal to the work done by the internal forces, which can be shown as

$$W_{int} = W_{ext} \quad (4.1)$$

In the above equation, internal work is a result of internal stresses and strains, whereas external work is composed of body forces, surface forces and concentrated forces, such that

$$W_{int} = \int_V \tau \varepsilon dV \quad (4.2)$$

$$W_{ext} = \int_V f^B U dV + \int_S f^S U dS + \sum_i F^i U^i \quad (4.3)$$

In equation (4.2) τ and ε are the internal stress and strain respectively. In equation (4.3), f^B , f^S , F^i are body forces, surface forces, concentrated forces respectively, where U and U^i are the displacement and displacement at the application point of F^i .

The internal stresses in a body are related to the strains in the same body with some constitutive relationship. Writing in vector form, this relationship can be presented as

$$\tau = \mathbf{C} \varepsilon \quad (4.4)$$

Using equation (4.4), internal work in equation (4.2) can be rewritten in vector form

$$W_{int} = \int_V \varepsilon^T \mathbf{C} \varepsilon dV \quad (4.5)$$

In displacement based finite element analysis, displacement field in an element is tried to be expressed as a function of displacements of nodes of the element, which are called nodal point displacements. The functions relating the displacement of a point in the element and the nodal point displacements are known as shape functions. On the other hand, strains of an element can be calculated using the displacement information, i.e.

derivatives of displacements give the strain values. Therefore a relation is also known between the strain and displacement parameters. Using this relation and the assumed shape functions, strain and nodal point displacements can be directly related. This relation is shown as

$$\boldsymbol{\varepsilon} = \mathbf{B}\mathbf{u} \quad (4.6)$$

In equation (4.6), \mathbf{u} is the nodal point displacement vector of the element, and matrix \mathbf{B} is known as the strain–displacement matrix.

After defining the nodal point displacements and the relation of them with strains, nodal point displacement matrices can be implemented in to the work equations. Using equation (4.3) and inserting nodal point displacements in that equation, the vector notation for external work can be expressed as,

$$W_{ext} = \int_V \mathbf{u}^T \mathbf{f}^B dV + \int_S \mathbf{u}^T \mathbf{f}^S dS + \mathbf{u}^T \mathbf{F} \quad (4.7)$$

In the same way, internal work in equation (4.5) can also be rewritten as follows:

$$W_{int} = \int_V \mathbf{u}^T \mathbf{B}^T \mathbf{C} \mathbf{B} \mathbf{u} dV \quad (4.8)$$

Expressing equation (4.1) in terms of equation (4.7) and equation (4.8) gives the following equality:

$$\int_V \mathbf{u}^T \mathbf{B}^T \mathbf{C} \mathbf{B} \mathbf{u} dV = \int_V \mathbf{u}^T \mathbf{f}^B dV + \int_S \mathbf{u}^T \mathbf{f}^S dS + \mathbf{u}^T \mathbf{F} \quad (4.9)$$

The elemental nodal point displacement vector can also be related with the global nodal point displacement vector:

$$\mathbf{u}^{(m)} = \mathbf{H}^{(m)} \mathbf{U} \quad (4.10)$$

In this equation, the superscript (m) shows the number of the element, and \mathbf{U} is the global nodal displacement vector. Using equation (4.10) and considering the fact that global nodal displacement vector is independent of the integration variables, equation (4.9) can be rewritten to include the assemblage of the elements of the whole structure

$$\begin{aligned} \sum \left(\int_{V^{(m)}} \mathbf{B}^T{}^{(m)} \mathbf{C}^{(m)} \mathbf{B}^{(m)} dV^{(m)} \right) \mathbf{U} = \\ \sum \left(\int_{V^{(m)}} \mathbf{H}^T{}^{(m)} \mathbf{f}^{B^{(m)}} dV^{(m)} \right) + \\ \sum \left(\int_{S^{(m)}} \mathbf{H}^T{}^{(m)} \mathbf{f}^{S^{(m)}} dS^{(m)} \right) + \sum \left(\mathbf{H}^T{}^{(m)} \mathbf{F}^{(m)} \right) \end{aligned} \quad (4.11)$$

In the above equation, the integral in the summation term on the left hand side, is called the elemental stiffness matrix of an element. Therefore, the summation on the left hand side gives the global stiffness matrix of the whole structure. For the whole structure, this equation can be briefly written as:

$$\mathbf{KU} = \mathbf{F} \quad (4.12)$$

where \mathbf{K} is the global stiffness matrix, \mathbf{F} is the total global force vector of the system.

In equation (4.11), it should be noted that integrations are evaluated for each element separately, therefore while evaluating these integrations, local coordinate systems can be used. In the assemblage procedure, however, necessary coordinate transformations must be carried out. Using local coordinate systems helps a lot in the evaluation procedure, as the integrals would become very complicated after transformation to the global coordinates. Therefore, first elemental stiffness matrices are calculated, and

then they are transformed to the global coordinate system before assemblage.

In the above discussion, nonlinear components of the equation are neglected. In large displacement – large strain problems, however, there is a nonlinearity in the governing equations; therefore an incremental or iterative solution scheme is required. To include the effect of nonlinearity in the stiffness matrix, the overall stiffness matrix can be divided into two parts, such that

$$\mathbf{K} = \mathbf{K}_L + \mathbf{K}_{NL} \quad (4.13)$$

where \mathbf{K}_L is equivalent to the \mathbf{K} matrix in equation (4.12). The nonlinear component of the stiffness matrix can be written as,

$$\mathbf{K}_{NL} = \sum_V \int \mathbf{B}_{NL}^T \boldsymbol{\tau} \mathbf{B}_{NL} dV \quad (4.14)$$

In equation (4.14), \mathbf{B}_{NL} is the nonlinear strain–displacement matrix, and $\boldsymbol{\tau}$ is the stress configuration of the body. In incremental analysis, incremental displacements are used in the solution procedure, so incremental strain–displacement matrix is used. This gives the incremental stiffness matrix, which is also known as tangential stiffness matrix, and a left superscript \mathbf{t} is used to denote it, e.g. ${}^t\mathbf{K}$. Using the updated Lagrangian formulation and writing in incremental form, the general equation is

$$\left({}^t\mathbf{K}_L + {}^t\mathbf{K}_{NL} \right) \Delta \mathbf{U}^{(i)} = {}^{t+\Delta t}\mathbf{R} - {}_{t+\Delta t}^{t+\Delta t}\mathbf{F}^{(i-1)} \quad (4.15)$$

In equation (4.15), the left superscript refers to the configuration of the quantity, the left subscript indicates the quantity is measured with respect to which configuration. The right superscript shows that the quantity corresponds to which iteration. $\Delta \mathbf{U}$ is the incremental displacement vector,

\mathbf{R} is the externally applied nodal force vector, and \mathbf{F} is the nodal point forces corresponding to the element stresses in that configuration which can be written as

$$\mathbf{F} = \int_V \mathbf{B}^T \boldsymbol{\tau} dV \quad (4.16)$$

for an element, where $\boldsymbol{\tau}$ is the stress vector.

Using equations (4.11), (4.13), (4.14) and (4.16), equation (4.15) can be rewritten as follows:

$$\begin{aligned} & \left(\sum_{V^{(m)}} \int \mathbf{B}^{T(m)} \mathbf{C}^{(m)} \mathbf{B}^{(m)} dV^{(m)} + \right. \\ & \left. \sum_{V^{(m)}} \int \mathbf{B}^{T(m)}_{NL} \boldsymbol{\tau}^{(m)} \mathbf{B}^{(m)}_{NL} dV^{(m)} \right) \Delta \mathbf{U}^{(i)} = \\ & \mathbf{R} - \sum_{V^{(m)}} \int \mathbf{B}^{T(m)} \mathbf{L} \boldsymbol{\tau}^{(m)(i-1)} dV^{(m)} \end{aligned} \quad (4.17)$$

Up to this point, static equilibrium conditions are considered. The above equation is the equilibrium statement at any specific time. If the loads are applied rapidly, inertia effects must also be considered. This means that system becomes a dynamic one. Using d'Alembert's principle, inertia forces can be treated as a part of body forces. To apply this principle, element accelerations must be known. The accelerations can be calculated by using the same relation used between elemental nodal point displacement vector and global nodal point displacement vector:

$$\ddot{\mathbf{u}}^{(m)} = \mathbf{H}^{(m)} \ddot{\mathbf{U}} \quad (4.10a)$$

This equation can be used to rewrite the internal body force equation:

$$\mathbf{R}^B = \sum \left(\int_{V^{(m)}} \mathbf{H}^{\tau(m)} \left(\mathbf{f}^{B(m)} - \rho^{(m)} \mathbf{H}^{(m)} \ddot{\mathbf{U}} \right) dV^{(m)} \right)$$

Using the second term in brackets, mass matrix of the whole structure can be assembled:

$$M = \sum \int_{V^{(m)}} \mathbf{H}^{\tau(m)} \rho^{(m)} \mathbf{H}^{(m)} dV^{(m)} \quad (4.18)$$

Using the new body force, equation (4.11) can be written as

$$\begin{aligned} & \sum \left(\int_{V^{(m)}} \mathbf{B}^{\tau(m)} \boldsymbol{\tau}^{(m)} dV^{(m)} \right) = \\ & \sum \left(\int_{V^{(m)}} \mathbf{H}^{\tau(m)} \left(\mathbf{f}^{B(m)} - \rho^{(m)} \mathbf{H}^{(m)} \ddot{\mathbf{U}} \right) dV^{(m)} \right) + \\ & \sum \left(\int_{S^{(m)}} \mathbf{H}^{\tau(m)} \mathbf{f}^{S(m)} dS^{(m)} \right) + \sum \left(\mathbf{H}^{\tau(m)} \mathbf{F}^{(m)} \right) \end{aligned} \quad (4.19)$$

Then, this equality can be simply represented as:

$$\mathbf{M} \ddot{\mathbf{U}} = \mathbf{R}_{\text{ext}} - \mathbf{R}_{\text{int}} \quad (4.20)$$

This is the general equation for the displacement based non-linear finite element analysis for a large displacement – large strain problem, using the updated Lagrangian formulation.

As a dynamic effect, damping forces can also be included in the above formulation. The damping forces are proportional to the velocities of the elements. Similar relations can be used to calculate the velocities as in displacements or accelerations, but it is difficult to calculate the damping matrices for the finite element calculations, because damping properties are frequency dependent. General approach is to calculate damping matrix of the general assembly using constructed mass matrix and the stiffness matrix. Rayleigh damping scheme uses a linear combination of mass and stiffness matrices:

$$\mathbf{C} = \alpha \mathbf{K} + \beta \mathbf{M}$$

In this equation, α and β are called stiffness and mass proportional constants, respectively. Empirical values of these constants are between 0.001 and 0.01 according to experiments. Therefore, the damping matrix can be neglected in finite element calculations safely. By not modeling the damping effect, efficiency of calculations in analysis increases. Considering these arguments, analysis of damping is not included in this study.

4.3 Classical Shell Theory

In this study, classical shell theory is chosen as basis. There are several assumptions in this theory. The stress through the thickness of the shell is zero. Material particals that are originally on a straight line perpendicular to the mid-surface of the shell remain on a straight line during deformation. In the Kirchoff theory, shear deformations are neglected, whereas in the Mindlin theory shear deformations are included, therefore line originally normal to the mid-surface does not does not remain perpendicular to the mid-surface during deformations. There are some difficulties in these approaches that the element must satisfy the convergence requirements.

Using the assumption of Mindlin theory, displacement components of a point are as follows:

$$u = z\beta_x(x, y) \quad v = -z\beta_y(x, y) \quad w = w(x, y)$$

where β_x and β_y are the rotations of the normal to the undeformed middle surface in the x-z and y-z planes, respectively.

The analysis of thin walled structures requires a reduction from three to two dimensions. This may be carried out before or together with discretization using either a plate or shell theory. Despite the fact that in both cases the continuum is degenerated to a surface structure, the term degeneration is used for the latter approach. The simplicity in accommodating arbitrarily large deformation and rotation problems is a favorite advantage to degenerated curved shell elements.

Considering a plate undergoing large deflections, it is recognized that as soon as the plate has deflected significantly, the action of the structure is really that of a shell; i.e. the structure is now curved and both membrane and bending stresses are significant.

4.4 Strain–Displacement Matrix

In this study, a shell element is decided to be used. A 4–node element, which has a five degree of freedom at each node, is going to be developed in this section. There will be three translational and two rotational degrees of freedom, and the third degree of freedom, which is warping, will be neglected. By this element, both membrane and bending behaviors can be simulated.

Assume a local coordinate system that is attached to the element consists of r , s and t -axes. First of all, a general function should be obtained to give the position values of a point in the element. If the function is able to be derived such that the variables are the nodal point positions, it is possible to obtain the position of any point in the element by just knowing the position of the four nodes of the element. Such a function is

$${}^t x_i = h_j {}^t x_i^j + \frac{t}{2} a_j h_j {}^t V_{ni}^j \quad i = 1, 2, 3 \text{ and } j = 1, 2, 3, 4 \quad (4.21)$$

In equation (4.21), the superscript for x denotes the node number and subscript for the direction. ${}^t V_{ni}^j$ is the x_i -axes component of the unit vector normal to the mid-plane of the shell element in t -direction at time t . a_j is the thickness of the shell at node j . h is named the shape function and relates the nodal positions to the coordinates of any point in the element. In this study, the shape functions proposed by Bathe [37] are used. These are, in terms of local coordinates (according to the numbering of nodes in the figure):

$$\begin{aligned} h_1 &= \frac{1}{4}(1+r)(1+s) \\ h_2 &= \frac{1}{4}(1-r)(1+s) \\ h_3 &= \frac{1}{4}(1-r)(1-s) \\ h_4 &= \frac{1}{4}(1+r)(1-s) \end{aligned} \quad (4.22)$$

Displacement at time t is represented by Bathe [37] as follows:

$$\begin{aligned} {}^t u_i &= {}^t x_i - {}^0 x_i \\ &= h_j {}^t u_i^j + \frac{t}{2} a_j h_j ({}^t V_{ni}^j - {}^0 V_{ni}^j) \end{aligned} \quad (4.23)$$

Incremental displacement and unit normal vector V can be defined in the following way:

$$\begin{aligned}
u_i &= {}^{t+\Delta t}x_i - {}^tx_i \\
V_{ni} &= {}^{t+\Delta t}V_{ni} - {}^tV_{ni}
\end{aligned} \tag{4.24}$$

Therefore u can be rewritten as:

$$u_i = h_j u_i^k + \frac{t}{2} a_j h_j V_{ni}^j \tag{4.25}$$

The vector tV_n is in the direction of t -axis. However, there is no rotational deformation measured about that axis. So, it is needed two vectors which are orthonormal to the tV_n , such that the rotations about these axes can be used to calculate the nodal direction cosines of the shell element. First orthogonal vector can be defined as:

$${}^tV_1^j = \frac{e_y \times {}^tV_n^j}{|e_y \times {}^tV_n^j|} \tag{4.26}$$

Then the second vector can be easily obtained by the cross product of two vectors.

$${}^tV_2^j = {}^tV_n^j \times {}^tV_1^j \tag{4.27}$$

Using equations (4.26) and (4.27) incremental unit normal vector is

$$V_{ni}^j = {}^tV_{1i}^j \beta_j - {}^tV_{2i}^j \alpha_j \tag{4.28}$$

where α_j and β_j are the incremental rotations of the normal vector about vectors ${}^tV_1^j$ and ${}^tV_2^j$, respectively. Inserting equation (4.28) into equation (4.25) following relation for incremental displacement is obtained.

$$u_i = h_j u_i^j + \frac{t}{2} a_j h_j ({}^tV_{1i}^j \beta_j - {}^tV_{2i}^j \alpha_j) \quad (4.29)$$

Equation (4.29) can be differentiated with respect to local coordinates. In the differentiation, it must be noted that the only dependent variables are the shape functions h_j and t coordinate. So derivative with respect to r can be written as:

$$\begin{aligned} u_{i,r} &= h_{j,r} \left(u_i^j + \frac{-t}{2} a_j {}^tV_{2i}^j \alpha_j + \frac{t}{2} a_j {}^tV_{1i}^j \beta_j \right) \\ &= h_{j,r} \begin{bmatrix} 1 & -\frac{t}{2} a_j {}^tV_{2i}^j & \frac{t}{2} a_j {}^tV_{1i}^j \end{bmatrix} \begin{bmatrix} u_i^j & \alpha_j & \beta_j \end{bmatrix} \end{aligned} \quad (4.30)$$

Similarly, other derivatives can be obtained; therefore the following matrix can be formulated:

$$\begin{pmatrix} u_{i,r} \\ u_{i,s} \\ u_{i,t} \end{pmatrix} = \begin{pmatrix} h_{j,r} \left(1 & -\frac{t}{2} a_j {}^tV_{2i}^j & \frac{t}{2} a_j {}^tV_{1i}^j \right) \\ h_{j,s} \left(1 & -\frac{t}{2} a_j {}^tV_{2i}^j & \frac{t}{2} a_j {}^tV_{1i}^j \right) \\ h_j \left(0 & -\frac{1}{2} a_j {}^tV_{2i}^j & \frac{1}{2} a_j {}^tV_{1i}^j \right) \end{pmatrix} \begin{pmatrix} u_i^j \\ \alpha_j \\ \beta_j \end{pmatrix} \quad (4.31)$$

The derivatives of the other displacement components can be obtained in the same way. However, these derivatives are with respect to local coordinates. To achieve these derivatives chain rule can be used, so derivative with respect to local coordinate system can be represented as a function of derivatives with respect to the global coordinate system. The representation is as follows:

$$\frac{\partial u_i}{\partial r} = \frac{\partial u_i}{\partial x_1} \frac{\partial x_1}{\partial r} + \frac{\partial u_i}{\partial x_2} \frac{\partial x_2}{\partial r} + \frac{\partial u_i}{\partial x_3} \frac{\partial x_3}{\partial r} \quad (4.32)$$

For all three displacement components, following matrix representation can be used for the relation of derivatives:

$$\begin{pmatrix} u_{i,r} \\ u_{i,s} \\ u_{i,t} \end{pmatrix} = \begin{pmatrix} \frac{\partial x_1}{\partial r} & \frac{\partial x_2}{\partial r} & \frac{\partial x_3}{\partial r} \\ \frac{\partial x_1}{\partial s} & \frac{\partial x_2}{\partial s} & \frac{\partial x_3}{\partial s} \\ \frac{\partial x_1}{\partial t} & \frac{\partial x_2}{\partial t} & \frac{\partial x_3}{\partial t} \end{pmatrix} \begin{pmatrix} u_{i,x_1} \\ u_{i,x_2} \\ u_{i,x_3} \end{pmatrix} \quad (4.33)$$

where (3 x 3) matrix on the left-hand side of the equation is known as Jacobean matrix, and represented by J . Therefore derivatives of displacements with respect to global coordinates can be calculated by:

$$\begin{pmatrix} u_{i,x_1} \\ u_{i,x_2} \\ u_{i,x_3} \end{pmatrix} = J^{-1} \begin{pmatrix} h_{j,r} \left(1 - \frac{t}{2} a_j {}^tV_{2i}^j & \frac{t}{2} a_j {}^tV_{1i}^j \right) \\ h_{j,s} \left(1 - \frac{t}{2} a_j {}^tV_{2i}^j & \frac{t}{2} a_j {}^tV_{1i}^j \right) \\ h_j \left(0 - \frac{1}{2} a_j {}^tV_{2i}^j & \frac{1}{2} a_j {}^tV_{1i}^j \right) \end{pmatrix} \begin{pmatrix} u_i^j \\ \alpha_j \\ \beta_j \end{pmatrix} \quad (4.34)$$

Let G be a matrix such that $\mathbf{u}_{i,x} = G_i \mathbf{u}$. Then components of G are:

$$G_{k1}^j = J_{k1}^{-1} h_{j,r} + J_{k2}^{-1} h_{j,s} \quad (4.35a)$$

$$G_{k2,i}^j = \left(\frac{1}{2} a_j {}^tV_{2i}^j \right) \left(-t J_{k1}^{-1} h_{j,r} - t J_{k2}^{-1} h_{j,s} - J_{k3}^{-1} h_j \right) \quad (4.35b)$$

$$G_{k3,i}^j = \left(\frac{1}{2} a_j {}^tV_{1i}^j \right) \left(t J_{k1}^{-1} h_{j,r} + t J_{k2}^{-1} h_{j,s} + J_{k3}^{-1} h_j \right) \quad (4.35c)$$

where the subscript i denote the global coordinate with respect to which the derivatives are taken and kn denotes the row and column of the component.

Linear strains are calculated as follows:

$$e_{ij} = \frac{1}{2} \left(\frac{\partial u_i}{\partial x_j} + \frac{\partial u_j}{\partial x_i} \right) \quad (4.36)$$

Strain vector and corresponding displacement vector can be written down in the following form:

$$\mathbf{e} = \left[{}^t e_{11} \quad {}^t e_{22} \quad {}^t e_{33} \quad 2 {}^t e_{12} \quad 2 {}^t e_{23} \quad 2 {}^t e_{13} \right]^T \quad (4.37)$$

$$u = \left[u_1^1 \quad u_2^1 \quad u_3^1 \quad \alpha_1 \quad \beta_1 \quad \dots u_1^4 \quad u_2^4 \quad u_3^4 \quad \alpha_4 \quad \beta_4 \right]^T$$

Now, using from equation (4.34) to (4.37), linear strain displacement matrix can be obtained as follows:

$$\mathbf{B}_L = \begin{pmatrix} \dots & G_{11}^j & 0 & 0 & G_{12.1}^j & G_{13.1}^j & \dots \\ \dots & 0 & G_{21}^j & 0 & G_{22.2}^j & G_{23.2}^j & \dots \\ \dots & 0 & 0 & G_{31}^j & G_{32.3}^j & G_{33.3}^j & \dots \\ \dots & G_{21}^j & G_{11}^j & 0 & G_{22.1}^j + G_{12.2}^j & G_{23.1}^j + G_{13.2}^j & \dots \\ \dots & 0 & G_{31}^j & G_{21}^j & G_{32.2}^j + G_{22.3}^j & G_{33.2}^j + G_{23.3}^j & \dots \\ \dots & G_{31}^j & 0 & G_{11}^j & G_{32.1}^j + G_{12.3}^j & G_{33.1}^j + G_{13.3}^j & \dots \end{pmatrix} \quad (4.38)$$

For the following stress matrix, non-linear strain displacement matrix can also be obtained in a similar way:

$${}^t \boldsymbol{\tau} = \begin{pmatrix} {}^t \boldsymbol{\tau}_{11} \mathbf{I}_3 & & sym. \\ {}^t \boldsymbol{\tau}_{12} \mathbf{I}_3 & {}^t \boldsymbol{\tau}_{22} \mathbf{I}_3 & \\ {}^t \boldsymbol{\tau}_{13} \mathbf{I}_3 & {}^t \boldsymbol{\tau}_{23} \mathbf{I}_3 & {}^t \boldsymbol{\tau}_{33} \mathbf{I}_3 \end{pmatrix} \quad (4.39)$$

Then non-linear strain displacement matrix can be written as:

$$\mathbf{B}_{NL} = \begin{pmatrix} \dots & G_{11}^j & 0 & 0 & G_{12.1}^j & G_{13.1}^j & \dots \\ \dots & 0 & G_{11}^j & 0 & G_{12.2}^j & G_{13.2}^j & \dots \\ \dots & 0 & 0 & G_{11}^j & G_{12.3}^j & G_{13.3}^j & \dots \\ \dots & G_{21}^j & 0 & 0 & G_{22.1}^j & G_{23.1}^j & \dots \\ \dots & 0 & G_{21}^j & 0 & G_{22.2}^j & G_{23.2}^j & \dots \\ \dots & 0 & 0 & G_{21}^j & G_{22.3}^j & G_{23.3}^j & \dots \\ \dots & G_{31}^j & 0 & 0 & G_{32.1}^j & G_{33.1}^j & \dots \\ \dots & 0 & G_{31}^j & 0 & G_{32.2}^j & G_{33.2}^j & \dots \\ \dots & 0 & 0 & G_{31}^j & G_{32.3}^j & G_{33.3}^j & \dots \end{pmatrix} \quad (4.40)$$

4.5 Matrix Representing Constitutive Relations

To formulate the stiffness matrix of an element, constitutive relations within the element must also be considered. So a matrix should be constructed for these relations. The material nonlinearity is included in the formulation by this matrix.

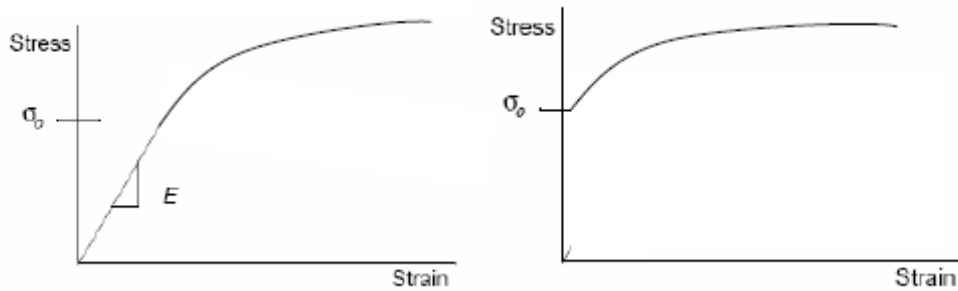


Figure 4.1 Typical elasto-plastic and rigid plastic curves

An elasto–plastic material behavior is assumed in this study. Therefore a yield criterion for the transition between the elastic and plastic regions is needed. Also to define the plastic behavior of the material, a flow rule is required. For the yield condition, Von Mises yield criterion is chosen. It can be written as follows:

$$\frac{1}{3} \left({}^t\tau_y \right)^2 = \sum_i \sum_j \frac{1}{2} \left({}^t\tau'_{ij} \right)^2 \quad (4.41)$$

where ${}^t\tau_y$ is the yield stress and ${}^t\tau'_{ij}$ are the deviatoric stresses at time t . It should be noted that, the material is assumed to be strain hardening, therefore ${}^t\tau_y$ is dependent on the current strain values. Besides, initiation of plastic flow is assumed to be independent of the selected coordinate system, thus the yield criterion is actually a function of invariants of the stress tensor. Moreover, it is assumed that the hydrostatic stress has no effect on yielding, so deviatoric stresses are used to express the yield condition. Actually, the right hand side of equation (4.41) is the second invariant of the deviatoric stress tensor. Therefore, equation (4.41) can be rewritten as follows:

$${}^t f \left(II({}^t\tau'), {}^t\tau_y \right) = \sum_i \sum_j \frac{1}{2} \left({}^t\tau'_{ij} \right)^2 - \frac{1}{3} \left({}^t\tau_y \right)^2 = 0 \quad (4.42)$$

Swift's Law is used as the material plastic flow rule. Swift Law can be shown as:

$$\sigma^{eff} = A \left(B + \epsilon^{eff} \right)^n \quad (4.43)$$

In the above equation, A , B and n are material constants. The subscript eff is the abbreviation of “effective”, and effective strain is an appropriate combination of all strain components. In this study, for the effective strain calculation, the following relation is used:

$$\begin{aligned} \left(\boldsymbol{\varepsilon}^{eff} \right)^2 &= \frac{1}{2} \left[\left(\boldsymbol{\varepsilon}_{11} - \boldsymbol{\varepsilon}_{22} \right)^2 + \left(\boldsymbol{\varepsilon}_{22} - \boldsymbol{\varepsilon}_{33} \right)^2 + \left(\boldsymbol{\varepsilon}_{33} - \boldsymbol{\varepsilon}_{11} \right)^2 \right] \\ &+ 6 \left[\left(\boldsymbol{\varepsilon}_{12} \right)^2 + \left(\boldsymbol{\varepsilon}_{23} \right)^2 + \left(\boldsymbol{\varepsilon}_{13} \right)^2 \right] \end{aligned} \quad (4.44)$$

In the elastic deformation range, Hooke's law applies to the material:

$${}^t \boldsymbol{\tau} = {}^t \mathbf{C}^E {}^t \boldsymbol{\varepsilon}^{el} \quad (4.45)$$

However, it should be noted that Hooke's law is also applicable for elastic strain increments in the elastic–plastic deformation zone, therefore:

$$\nabla {}^t \boldsymbol{\tau} dt = {}^t \mathbf{C}^E d {}^t \boldsymbol{\varepsilon}^{el} = {}^t \mathbf{C}^E \left(d {}^t \boldsymbol{\varepsilon} - d {}^t \boldsymbol{\varepsilon}^{pl} \right) \quad (4.46a)$$

$$\text{where} \quad \nabla {}^t \boldsymbol{\tau}_{ij} = {}^t \dot{\boldsymbol{\tau}}_{ij} - {}^t \boldsymbol{\tau}_{ip} {}^t \Omega_{pj} - {}^t \boldsymbol{\tau}_{jp} {}^t \Omega_{pi} \quad (4.46b)$$

In equation (4.46), $\nabla {}^t \boldsymbol{\tau}$ is Jauman stress rate, which is an objective stress rate tensor. ${}^t \Omega$ is the spin tensor and it physically represents the angular velocity:

$${}^t \Omega_{ij} = \frac{1}{2} \left(\frac{\partial {}^t \dot{u}_j}{\partial {}^t x_i} - \frac{\partial {}^t \dot{u}_i}{\partial {}^t x_j} \right) \quad (4.47)$$

To obtain the stress increments in terms of total strain increments, we need a new constitutive matrix.

$$\nabla {}^t \boldsymbol{\tau} dt = {}^t \mathbf{C}^{EP} d {}^t \boldsymbol{\varepsilon} \quad (4.48)$$

The aim is to construct the ${}^t\mathbf{C}^{\text{EP}}$ matrix. For the first step, the normality rule, a conclusion of Drucker's Postulate, should be recalled to obtain the plastic portion of the strain:

$$d{}^t\boldsymbol{\varepsilon}^{pl} = {}^t\lambda \frac{\partial {}^t f}{\partial {}^t \boldsymbol{\tau}} \quad (4.49)$$

It can be easily seen that the derivative at the right hand side is equal to the deviatoric stress, as von Mises yield criterion is used.

$$\frac{\partial {}^t f}{\partial {}^t \boldsymbol{\tau}} = {}^t \boldsymbol{\tau}' \quad (4.50)$$

In plastic deformation zone, $df = 0$ then

$$\frac{\partial {}^t f}{\partial {}^t \boldsymbol{\tau}} d{}^t \boldsymbol{\tau} + \frac{\partial {}^t f}{\partial {}^t \boldsymbol{\varepsilon}} d{}^t \boldsymbol{\varepsilon} = 0 \quad (4.51)$$

Using equation (4.46), (4.49), (4.50) and (4.51), the scalar ${}^t\lambda$ can be calculated.

$${}^t\lambda = \frac{\left({}^t \boldsymbol{\tau}'\right)^T {}^t \mathbf{C}^E d{}^t \boldsymbol{\varepsilon}}{\left(\frac{\partial {}^t f}{\partial {}^t \boldsymbol{\varepsilon}}\right)^T {}^t \boldsymbol{\tau}' + \left({}^t \boldsymbol{\tau}'\right)^T {}^t \mathbf{C}^E \frac{\partial {}^t f}{\partial {}^t \boldsymbol{\varepsilon}}} \quad (4.52)$$

The partial derivative of function f with respect to strains is

$$\frac{\partial {}^t f}{\partial {}^t \boldsymbol{\varepsilon}} = {}^t H {}^t \boldsymbol{\tau} \quad (4.53)$$

where H can be calculated as follows (E_T being the strain hardening modulus):

$$H = \frac{2}{3} \left(\frac{E E_T}{E - E_T} \right) \quad (4.54)$$

Now, combining equations (4.46), (4.48), (4.52) and (4.53) elasto-plastic material matrix can be constructed:

$${}^t\mathbf{C}^{EP} = {}^t\mathbf{C}^E - \frac{{}^t\mathbf{C}^E {}^t\boldsymbol{\tau}' \left({}^t\boldsymbol{\tau}' \right)^T {}^t\mathbf{C}^E}{\left(H {}^t\boldsymbol{\tau} \right)^T {}^t\boldsymbol{\tau}' + \left({}^t\boldsymbol{\tau}' \right)^T {}^t\mathbf{C}^E H {}^t\boldsymbol{\tau}} \quad (4.55)$$

For the calculation of the elastic material matrix, following relation is used:

$$C_{ijkl}^E = \frac{E \nu}{(1 + \nu)(1 - 2\nu)} \delta_{ij} \delta_{kl} + \frac{E}{2(1 + \nu)} (\delta_{ik} \delta_{lj} + \delta_{il} \delta_{jk}) \quad (4.56)$$

Then elasto-plastic material matrix is

$$\mathbf{C}^{EP} = \frac{E}{1 + \nu} \cdot \begin{pmatrix} \frac{1-\nu}{1-2\nu} - \beta \cdot \tau_{11}^2 & \frac{\nu}{1-2\nu} - \beta \cdot \tau_{11} \tau_{22} & \frac{\nu}{1-2\nu} - \beta \cdot \tau_{11} \tau_{33} & -\beta \cdot \tau_{11} \tau_{12} & -\beta \cdot \tau_{11} \tau_{23} & -\beta \cdot \tau_{11} \tau_{13} \\ \frac{\nu}{1-2\nu} - \beta \cdot \tau_{11} \tau_{22} & \frac{1-\nu}{1-2\nu} - \beta \cdot \tau_{22}^2 & \frac{\nu}{1-2\nu} - \beta \cdot \tau_{22} \tau_{33} & -\beta \cdot \tau_{22} \tau_{12} & -\beta \cdot \tau_{22} \tau_{23} & -\beta \cdot \tau_{22} \tau_{13} \\ \frac{\nu}{1-2\nu} - \beta \cdot \tau_{11} \tau_{33} & \frac{\nu}{1-2\nu} - \beta \cdot \tau_{22} \tau_{33} & \frac{1-\nu}{1-2\nu} - \beta \cdot \tau_{33}^2 & -\beta \cdot \tau_{33} \tau_{12} & -\beta \cdot \tau_{33} \tau_{23} & -\beta \cdot \tau_{33} \tau_{13} \\ -\beta \cdot \tau_{11} \tau_{12} & -\beta \cdot \tau_{22} \tau_{12} & -\beta \cdot \tau_{33} \tau_{12} & -\beta \cdot \tau_{12}^2 & -\beta \cdot \tau_{12} \tau_{23} & -\beta \cdot \tau_{12} \tau_{13} \\ -\beta \cdot \tau_{11} \tau_{23} & -\beta \cdot \tau_{22} \tau_{23} & -\beta \cdot \tau_{33} \tau_{23} & -\beta \cdot \tau_{12} \tau_{23} & -\beta \cdot \tau_{23}^2 & -\beta \cdot \tau_{23} \tau_{13} \\ -\beta \cdot \tau_{11} \tau_{13} & -\beta \cdot \tau_{22} \tau_{13} & -\beta \cdot \tau_{33} \tau_{13} & -\beta \cdot \tau_{12} \tau_{13} & -\beta \cdot \tau_{23} \tau_{13} & -\beta \cdot \tau_{13}^2 \end{pmatrix} \quad (4.57)$$

$$\text{Where } \beta = \frac{3}{2} \frac{1}{\tau_y^2} \frac{1}{1 + \frac{2 E E_T}{3 E - E_T} \frac{1}{E}}$$

4.6 Contact Algorithm

Contact of surfaces is the most challenging part of modeling of a metal forming simulation. Commercial programs use several different contact types to meet different conditions in different applications. User should choose the appropriate one among the alternatives.

In this study, the most suitable contact algorithm seems to be the penalty function method. This method is used to search the contact between nodes and surfaces. The surfaces of tools are assumed to be rigid, and nodes of blank are checked if they are in contact with the surfaces of die or punch. When a contact is determined, the penetration into the tool surface is used to calculate the normal component (according to tool surface) of contact force acting on the blank. The tangential component is evaluated appropriate friction laws.

In this method, point data description of the tool surface is adopted. Shape of the tool is expressed by Cartesian coordinate point data (x,y,z) , as shown in Fig.4.2. Contact is searched between the finite element node, and the projections of the tool surface patches on xy -, yz -, and xz -planes. On the xy -plane for example, the x -coordinate lines and y -coordinate lines form a series of cells. The contact conditions are checked between the finite element node and these cells. The cell, which holds the projection of the finite element node, is found. The Cartesian coordinates of the finite element node are (X_d, Y_d, Z_d) as shown in Fig.4.2. The cell is then labeled as (i, j, k, l) . The surface z coordinates of the four points are denoted as (z_i, z_j, z_k, z_l)

Using these points, two vectors that are orthogonal to each other can be defined. From these vectors, the surface normal $n=Ai+Bj+Ck$ can be calculated. After that the distance of the finite element node z_d can be found.

$$z_d = \frac{|AX_d + BY_d + CZ_d + d|}{\sqrt{A^2 + B^2 + C^2}} \quad (4.58)$$

where $Ax+By+Cz+d = 0$ is the equation of the plane "ijkl".

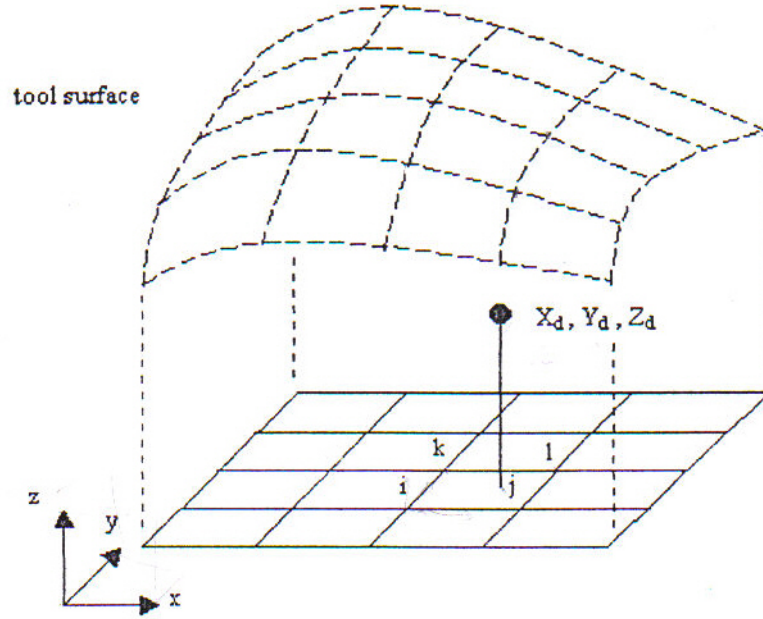


Figure 4.2 Point data description of tool surface with global search of contact

After z_d is found, according to the initial relative position of the tool and sheet, it can be determined whether the sheet contacts with the tool surface. To take the sheet thickness into account, the contact is checked with the z coordinates of the upper and lower node Z_d^{upper} , Z_d^{lower} and z_d .

Then, if the tool surface is above the sheet, the sheet will be in contact with the tool on the upper sheet surface in case of $Z_d^{\text{upper}} > z_d$. The penetration is calculated as follows:

$$P_d = Z_d^{upper} - z_d \quad (4.59)$$

If the tool surface is above the sheet, the sheet will be in contact with the tool on the upper sheet surface in case of $Z_d^{lower} < z_d$. The penetration is calculated then:

$$P_d = z_d - Z_d^{lower} \quad (4.59)$$

If the upper or lower node is found in contact with the tool, the contact force acting on the upper or lower node is decomposed into tool's surface normal and tangential directions. So are the internal force, velocity and acceleration of the node.

$$\begin{aligned} T &= T_n + T_t \\ R_{int} &= (R_{int})_n + (R_{int})_t \end{aligned} \quad (4.60)$$

$$\dot{u} = \dot{u}_n + \dot{u}_t$$

$$\ddot{u} = \ddot{u}_n + \ddot{u}_t$$

The magnitude of normal component of contact force is directly proportional to the penetration of node:

$$T_n = \psi P_d \quad (4.61)$$

In the above equation, T_n is the normal component of contact force, P_d is the penetration of blank node into tool surface, and ψ is the penalty

factor. The penalty factor represents the stiffness of the contacting element, such that,

$$\psi = \frac{A_s K}{l} \quad (4.62)$$

Where A_s is the element area, l is the maximum element length, and K is the Young's volume modulus of material.

Tangential component of the contact force is calculated according to Coulomb's law of friction. Normal component of the contact force is used in these calculations:

The contact search is performed different in several areas. For example, in the flange region, only die surface is considered in contact analysis. In the same way, under the punch head, blank can only penetrate into the punch, so only contact with the punch surface is searched. The reason for this approach is to increase the computational efficiency of the program. Contact search is very time consuming, therefore, minimizing the contact areas by defining non-contacting surfaces beforehand, used CPU time significantly decreases.

After both components of the contact force are known, these are combined and rearranged according to the global coordinate system. Then the results are added to the global external force vector.

4.7 Solution Scheme

The dynamic-explicit methods are based on the solution of a dynamic problem, even if it a quasi-static as in most application of metal forming. A

simple one dimensional mass-spring-damper system is considered to express to bases of these methods.

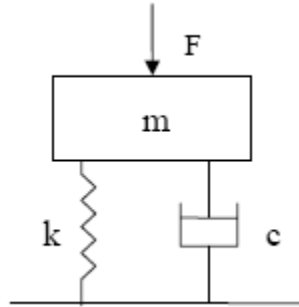


Figure 4.3 A mass–spring–damper system

The equation of motion for the free body diagram of mass is given as

$$m\ddot{u} + c\dot{u} + ku = f(t) \quad (4.63)$$

where m is the mass of the body, c is the damping coefficient of the damper, k is the stiffness of the spring, u , \dot{u} , and \ddot{u} are the instantaneous displacement, speed and acceleration of mass at time t , respectively, and $f(t)$ is the external force as a function of time.

The equation of motion can be solved using central difference method:

$${}^t\ddot{u} = \frac{1}{\Delta t^2} \left({}^{t+\Delta t}u - 2{}^tu + {}^{t-\Delta t}u \right) \quad (4.64a)$$

$${}^t\dot{u} = \frac{1}{2\Delta t} \left({}^{t+\Delta t}u - {}^{t-\Delta t}u \right) \quad (4.64b)$$

Substituting equations (4.64) into equation (4.63) and rearranging yields

$$\left(\frac{m}{\Delta t^2} + \frac{c}{2\Delta t} \right) {}^{t+\Delta t}u = f(t) - k{}^tu + \frac{2m}{\Delta t^2} {}^tu - \left(\frac{m}{\Delta t^2} - \frac{c}{2\Delta t} \right) {}^{t-\Delta t}u \quad (4.65)$$

The solution of displacement at time $t + \Delta t$ only depends on the displacement of the known states at times t and $t - \Delta t$. This time discretization scheme is named as dynamic explicit integration of the equation of motion. In case of the implicit integration methods, the solution depends also on the displacements of the unknown state at time $t + \Delta t$, which is usually expressed as dependency of the stiffness term on the unknown displacements [38].

The above solution scheme can also be applied to the general equation for the displacement based non-linear finite element analysis. Recall equation (4.20)

$$\mathbf{M}\ddot{\mathbf{U}} = \mathbf{R}_{\text{ext}} - \mathbf{R}_{\text{int}} \quad (4.20)$$

Adopting the same procedures to this equation, the following equality is reached:

$$\begin{aligned} \frac{1}{\Delta t^2} \mathbf{M}^{t+\Delta t} \mathbf{U} = \\ \mathbf{R}_{\text{ext}} - \mathbf{R}_{\text{int}} + \frac{2}{\Delta t^2} \mathbf{M}^t \mathbf{U} - \frac{1}{\Delta t^2} \mathbf{M}^{t-\Delta t} \mathbf{U} \end{aligned} \quad (4.66)$$

This equation can be solved for $^{t+\Delta t}\mathbf{U}$, using known $^t\mathbf{U}$ and $^{t-\Delta t}\mathbf{U}$. The initial conditions for nodal displacements, velocities, internal and external forces at the time $t=0$ are given; however the nodal displacements at $t=-\Delta t$ are also required at the very first step and it can be obtained from

$$^{-\Delta t}\mathbf{U} = {}^0\mathbf{U} - \Delta t {}^0\dot{\mathbf{U}} + \frac{\Delta t^2}{2} {}^0\ddot{\mathbf{U}} \quad (4.67)$$

where the initial accelerations are given by

$$\mathbf{M} {}^0\ddot{\mathbf{U}} = {}^0\mathbf{R}_{\text{ext}} - {}^0\mathbf{R}_{\text{int}} \quad (4.68)$$

To increase the computational efficiency the consistent mass matrices given in equation (4.18) are approximated by diagonal (lump) matrices: Equation (4.66) is uncoupled on the left hand side and no factorization is necessary. Furthermore, this approximation has proven itself quite useful since on one hand the central difference method is known to shorten the vibration period whereas the use of lumped matrices increase this period, thus a balanced total effect is obtained at the end [38].

Lumped mass matrix is obtained by placing mass particles at the nodes of the element, such that the total mass of the element is equal to the summation of mass values at the nodes. To obtain the lump mass matrix, total mass of the element must be computed. Then diagonal of the consistent mass matrix should be calculated. The final step is scaling of the diagonal elements by an appropriate coefficient to satisfy the conservation of mass. At the end a diagonal mass matrix is constructed.

For the four node shell element used in this study, the lumped mass matrix is calculated for each nodal point as follows:

$$\mathbf{M} = \frac{m}{4} \begin{bmatrix} 1 & 0 & 0 & 0 & 0 & 0 & \dots \\ 0 & 1 & 0 & 0 & 0 & 0 & \dots \\ 0 & 0 & 1 & 0 & 0 & 0 & \dots \\ 0 & 0 & 0 & \frac{(l_s + t^2)}{12} + \left(\frac{l_s}{2}\right)^2 & 0 & 0 & \dots \\ 0 & 0 & 0 & 0 & \frac{(l_r + t^2)}{12} + \left(\frac{l_s}{2}\right)^2 & 0 & \dots \\ \dots & \dots & \dots & \dots & \dots & \dots & \dots \end{bmatrix} \quad (4.69)$$

In representation above, l_s and l_r are the current element length values along r- and s-directions, and t is the current element thickness. The last two terms of the matrix are mass moments of inertia taken at the nodal positions of the element.

The explicit algorithm integrates through time by using small time increments. The central difference operator is conditionally stable and the stability limit for the operator with including the damping can be simply stated as

$$\Delta t < \frac{2}{\omega_{\max}} \left(\sqrt{1 + \zeta^2} - \zeta^2 \right)$$

where ω_{\max} is the maximum eigen-frequency of the system, and ζ is the fraction of critical damping. The above equation is valid for linear systems but it can be used as an estimate for nonlinear systems such as elasto-plastic metal forming problems. It is estimated that the critical time step for non-linear problems is about 50 - 80 % lower than the one computed for the linear systems [38].

In a finite element simulation, the critical time step can be also approximated for each element at each step by

$$\Delta t < \frac{L}{c} \quad (4.70)$$

where c is the elastic wave speed of material (speed of sound in that material) and L is the characteristic element dimension. The elastic wave speed is obtained from

$$c = \sqrt{\frac{2G(1-\nu)}{\rho(1-2\nu)}} \quad (4.71)$$

Calculation of each increment in dynamic-explicit methods is very robust and less time consuming than implicit methods; however, too small time steps result in unacceptable high number of increments, which make the dynamic-explicit methods infeasible. Two numerical tricks are applied to avoid this.

The total process time is reduced by exaggerating speed of moving tool or increasing the gradient of loading curves. In order to compensate the undesired effects of artificial inertia forces numerical damping is applied. This treatment is not suggested and an additional precaution should be taken for the analysis involving strain rate sensitive materials. In addition, increase in

the density of the material leads a reduction in the total number of increments since it reduces the sound of speed in the material and hence increases the minimum allowable time step. The additional artificial inertia forces cannot be reduced by introducing numerical artificial damping but these forces may be taken over by the rigid dies since in deep drawing most of the workpiece is supported by the dies [38]. Therefore, dynamic-explicit methods can be applied to the sheet metal forming processes successfully from this point of view.

4.8 Comparison of Implicit and Explicit Methods

Implicit methods satisfy the static equilibrium in the unknown final configuration of a time increment and enable a full static solution with convergence control. The increment size can be very large depending on the contact condition and the CPU time increases drastically as the element number increases because of the matrix inversion operation and accurate time integration scheme. This leads to the problem such as the divergence of the solution and the singularity of the stiffness matrix.

On the other hand, the most important advantage of the dynamic-explicit method is its robustness and independency of the stiffness term on the unknown displacement. The computational speed is faster and memory requirement is less than the static implicit methods. In addition, the region of the wrinkles is accurately determined in dynamic-explicit methods. However, the integration scheme is only valid if the mass matrix is lumped. Furthermore, the speed advantages can hold only if element computations are as few as possible. This is satisfied only by using single quadrature elements having rather poor stress and strain accuracy. It is claimed that the error introduced by a lumped mass matrix is compensated by a reduced integration scheme of the elements; however, this causes some disadvantages that the local stresses and spring-back is not accurately calculated and there is possibility to have hourglass (zero energy) modes.

CHAPTER 5

THEORETICAL RESULTS OF SIMULATIONS

In this study, the developed finite element program is used to simulate two different cup drawing operations: circular cup drawing and square cup drawing. The simulations are carried out using two symmetry axes because both cases are symmetric according to any two perpendicular axes. Therefore only $\frac{1}{4}$ of tools and blank are modeled.

The modeling operation is carried out in two steps. First, using a solid modeling program, 3-D models of tools and blank are constructed. Then, the constructed models are input to the commercial finite element program PAM-STAMP for meshing purposes. Using PAM-STAMP die and punch are meshed automatically. Maximum element size is set to be 5 mm for die and punch set.



Figure 5.1 Die–punch sets for circular and square cup drawing

Simulations for circular and rectangular cup drawing are carried out using five different mesh size. For this purpose, meshing process of circular and rectangular blank is carried out five times for each with element sizes from 5 mm to 1mm. The number of nodes and elements produced is given as tabulated below.

Table 5.1 Number of nodes and element used in analysis

Element Size (mm)	Circular Blank		Rectangular Blank	
	<i>Node</i>	<i>Element</i>	<i>Node</i>	<i>Element</i>
5	113	104	81	64
3	276	262	196	169
2	625	604	441	400
1	2433	2392	1681	1600

Material properties are also needed for blank modeling of blank. As stated before, elasto-plastic material model is used. For plastic flow simulation, Swift's rule is adopted in the formulations. Constants in Swift's rule, yield strength, modulus of elasticity and Poison's ratio are presented below. These are the properties of material used in experiments by Şenalp [40].

Table 5.2 Material constants used in simulations

$A \text{ (kN/mm}^2\text{)}$	0.667
$B \text{ (mm/mm)}$	0.054
n	0.361
$Y \text{ (kN/mm}^2\text{)}$	0.268
$E \text{ (kN/mm}^2\text{)}$	200
ν	0.3

In all simulations friction constant is taken as 0.04 according to the experiments carried out by Şenalp [40].

The punch is assumed to travel 10 mm/min. Both cups are drawn to a depth of 15 mm for each mesh. The program uses no blank-holding force in order to simulate the wrinkling case. For circular and square cup drawing, a total of 10 runs are performed with five different meshes for each case.

In order to verify the results, commercial program PAM-STAMP is used. The meshes are already prepared with PAM-STAMP, therefore same meshes are used. The material properties are also entered into the program manually, to achieve the same simulation conditions as with the developed code. Again, five runs are performed for circular and square cup drawing each.

For comparison, pictures of deformed meshes are taken at for different stages of drawing: 1mm, 5 mm, 10 mm, 15 mm. Besides, nodal point displacement histories of three nodes are traced. Displacements of nodes along x, y and z axis are compared between developed code and PAM-STAMP results.

In addition, the results obtained using developed code are also compared with experimental results. The experiments are carried out by Şenalp [40]. Experimental results are available for only square cup drawing; therefore comparison is limited with square cup drawing case.

Comparison with experimental results is carried out using thickness strain values. Measurements are taken at drawing depths 4 mm and 10.5 mm. The strains are read on the line connecting the center of blank and midpoint of side, and on diagonal line. The strain values at these depths are compared according to their initial positions with respect to center of blank.

Besides wrinkling analysis, code is used to solve deep drawing cases. Deep drawing runs are carried out for square cup drawing with element sizes 3mm, 2mm and 1mm. All the parameters are the same as previous cases. Blank-holder is modeled in the same way as other tools. Blank-holding force used is 750 kg.

The results obtained for deep drawing cases are compared with the values of experiments carried out by Şenalp [40]. Experimental readings are taken at 5mm and 10 mm drawing depth, again on a line connecting the center of blank and midpoint of side and on diagonal line.

5.1 Results for square cup drawing with blank–holder (element size 3 mm)

In this simulation, a square blank is drawn into a square cup. For modeling blank, element size is chosen to be 3 mm. A constant 250 kgf blank holder load is applied. The drawing is completed as punch travels 15 mm. Deformed shapes of blank at four different drawing depth are presented below.

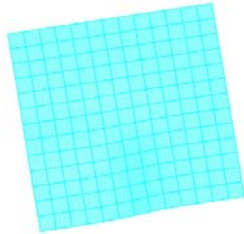
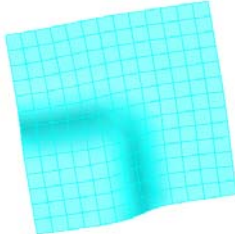
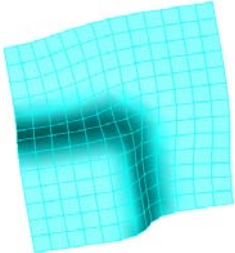
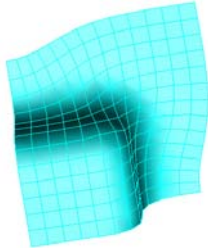
	Developed Code
a)	 A square grid of cyan lines, slightly tilted and distorted, representing a deformed shape at 1mm drawing depth.
b)	 A square grid of cyan lines, showing a more pronounced L-shaped deformation at the bottom-left corner, representing a deformed shape at 5mm drawing depth.
c)	 A square grid of cyan lines, showing a deeper L-shaped deformation at the bottom-left corner, representing a deformed shape at 10mm drawing depth.
d)	 A square grid of cyan lines, showing the most pronounced L-shaped deformation at the bottom-left corner, representing a deformed shape at 15mm drawing depth.

Figure 5.2 Deformed shapes at a) 1mm b) 5mm c) 10mm d) 15mm drawing depths

5.2 Results for square cup drawing with blank–holder (element size 2 mm)

In this simulation, a square blank is drawn into a square cup. For modeling blank, element size is chosen to be 2 mm. A constant 250 kgf blank holder load is applied. The drawing is completed as punch travels 15 mm. Deformed shapes of blank at four different drawing depth are presented below.

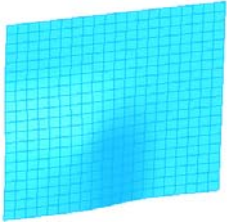
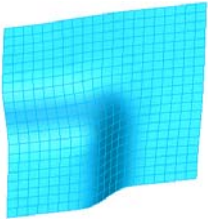
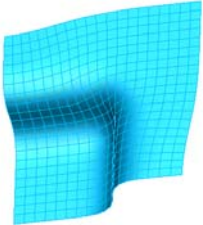
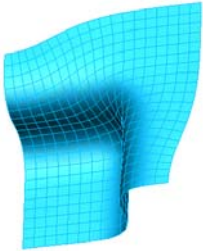
	Developed Code
a)	
b)	
c)	
d)	

Figure 5.3 Deformed shapes at a) 1mm b) 5mm c) 10mm d) 15mm drawing depths

5.3 Results for square cup drawing with blank–holder (element size 1 mm)

In this simulation, a square blank is drawn into a square cup. For modeling blank, element size is chosen to be 1 mm. A constant 250 kgf blank holder load is applied. The drawing is completed as punch travels 15 mm. Deformed shapes of blank at four different drawing depth are presented below.

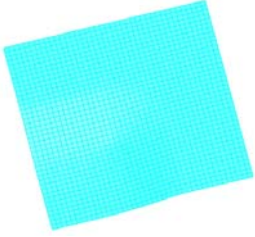
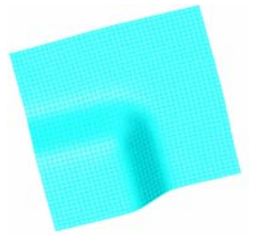
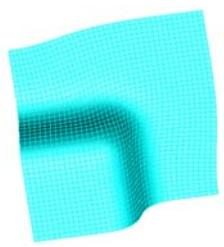
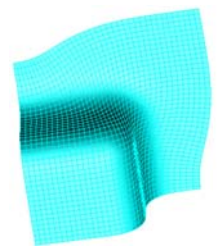
	Developed Code
a)	
b)	
c)	
d)	

Figure 5.4 Deformed shapes at a) 1mm b) 5mm c) 10mm d) 15mm drawing depths

5.4 Comparison of square cup drawing with blank holder case with experimental results

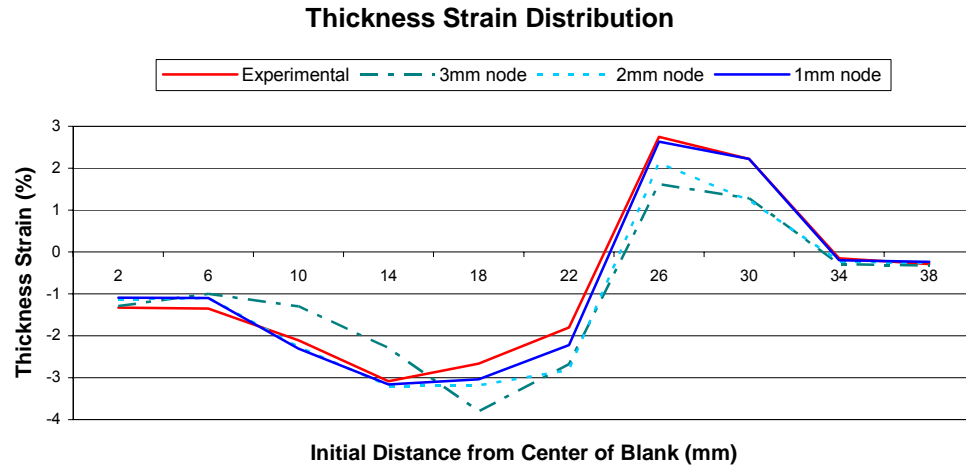


Figure 5.5 Thickness strain distribution along line connecting center of blank and midpoint of side at 5 mm drawing depth

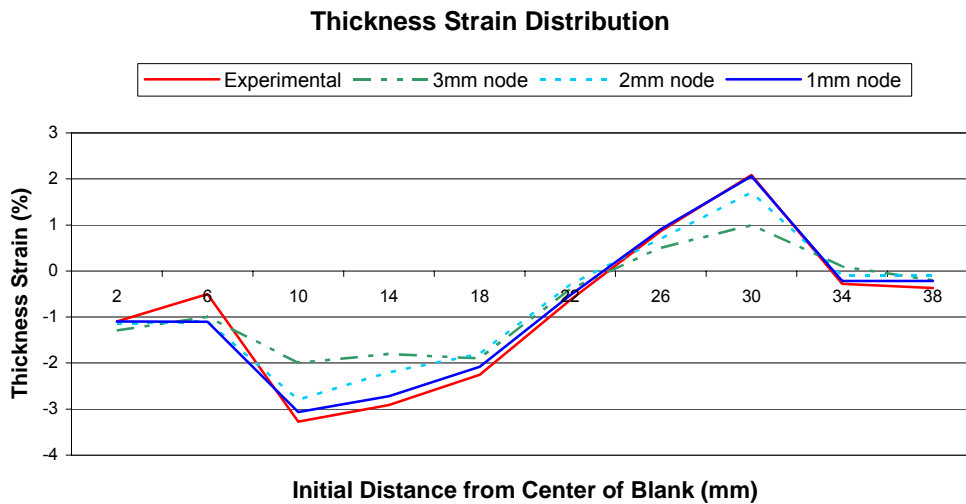


Figure 5.6 Thickness strain distribution along diagonal line at 5 mm drawing depth

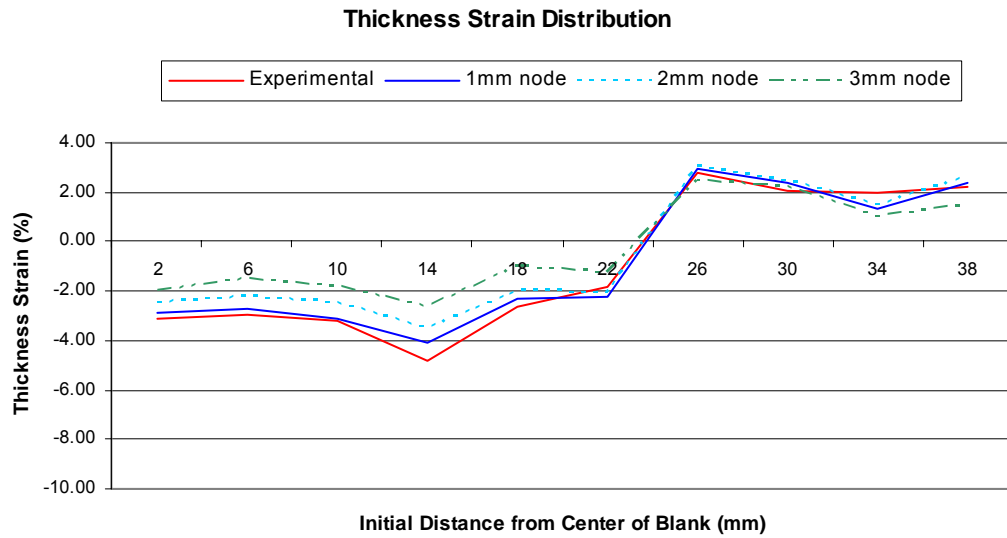


Figure 5.7 Thickness strain distribution along line connecting center of blank and midpoint of side at 10 mm drawing depth

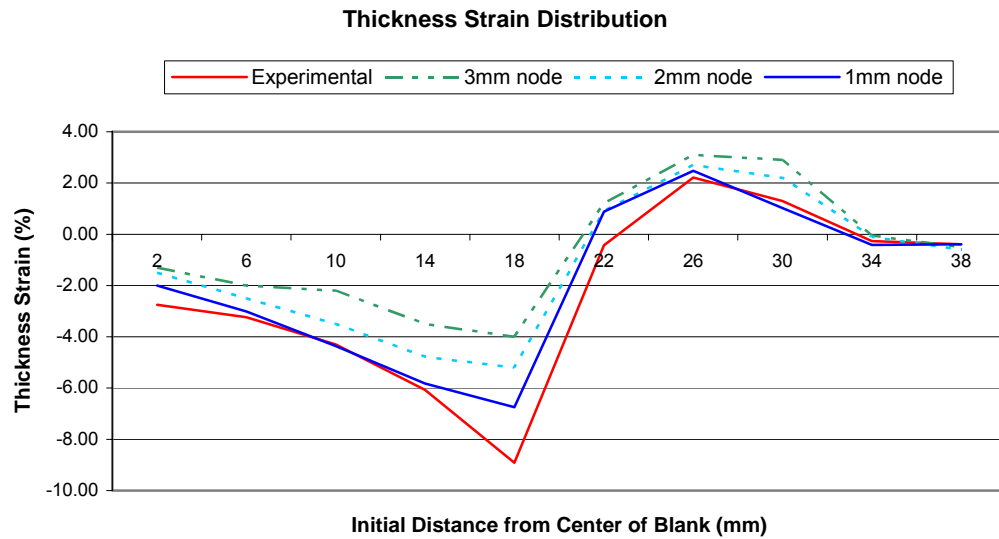


Figure 5.8 Thickness strain distribution along diagonal line at 10 mm drawing depth

5.5 Results for circular cup drawing (element size 5 mm)

In this simulation, a circular blank is drawn into a cylindrical cup. For modeling blank, element size is chosen to be 5 mm. No blank holder force is applied in order to analyze wrinkling. The drawing is completed as punch travels 15 mm. Analysis with the same conditions are conducted using PAM-STAMP. Nodal point displacement results of developed code at the nodes shown below are compared with the results of PAM-STAMP.

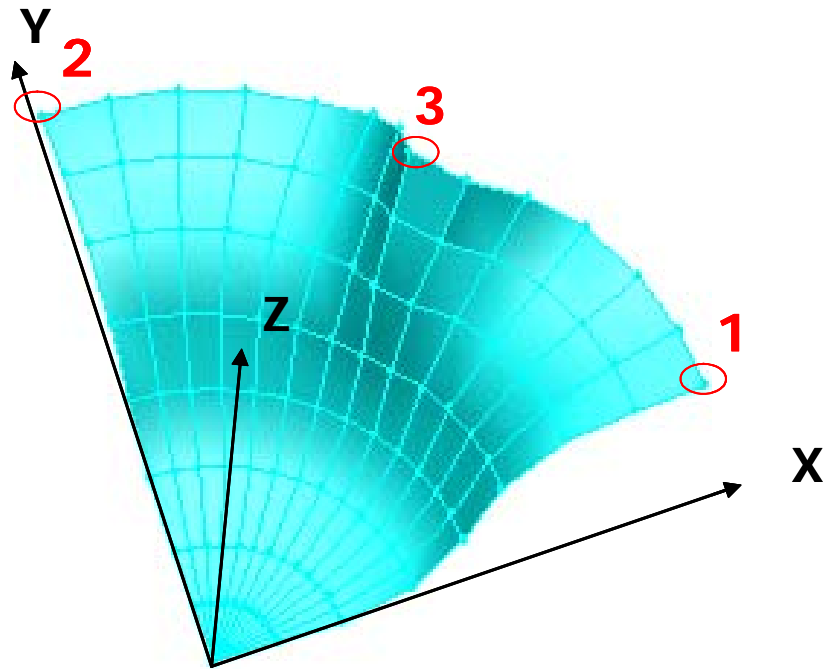


Figure 5.9 Orientation of circular blank with element size 5 mm

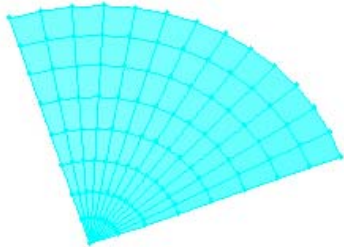
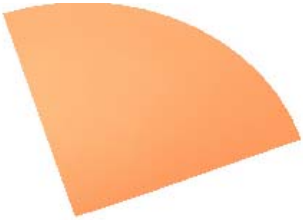
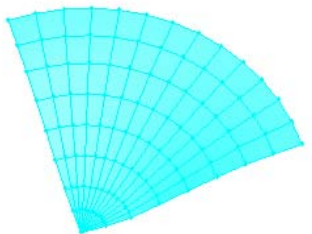
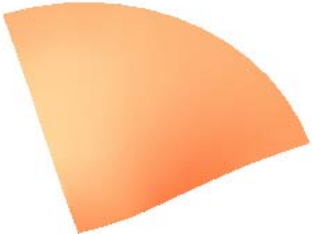
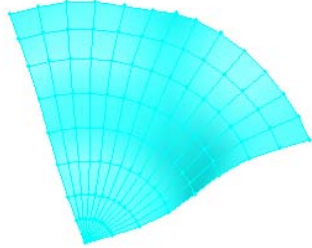
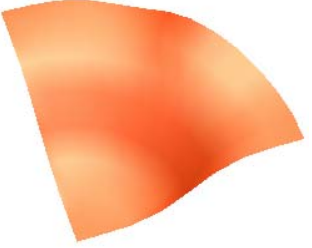
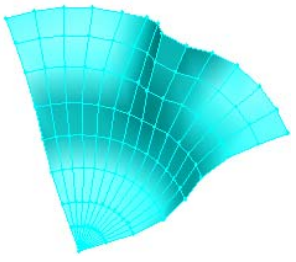
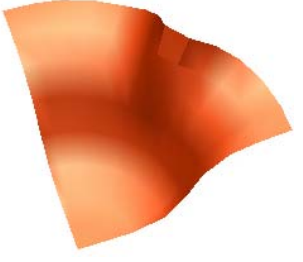
	Developed Code	PAM-STAMP
a)		
b)		
c)		
d)		

Figure 5.10 Deformed shapes at a) 1mm b) 5mm c) 10mm d) 15mm drawing depths

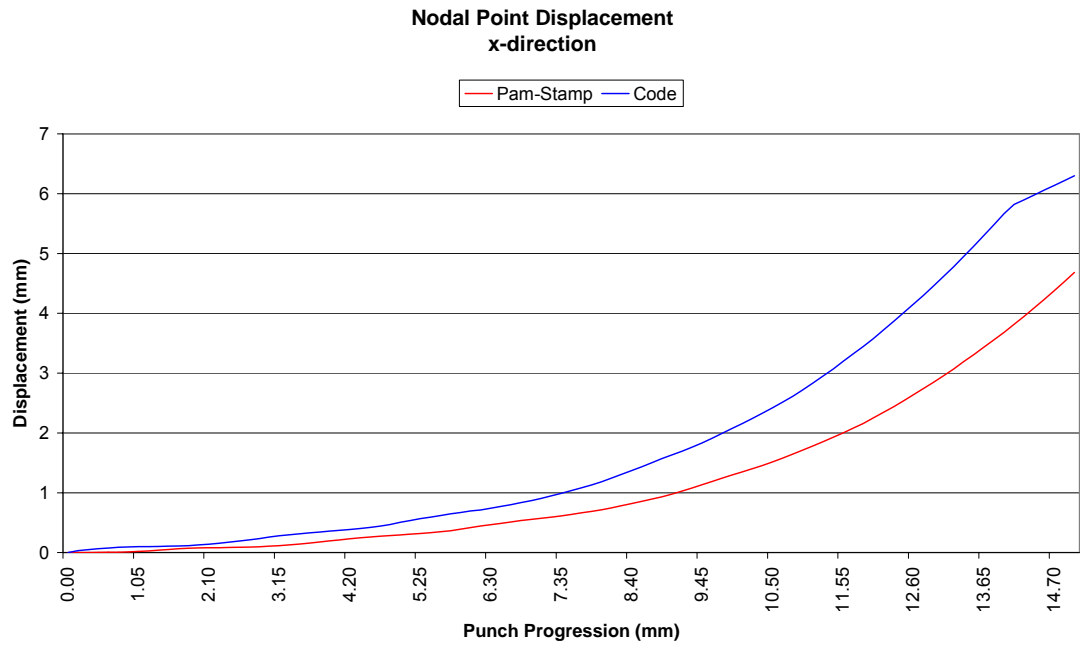


Figure 5.11 Displacement of node 1 in x-direction for 5 mm element size

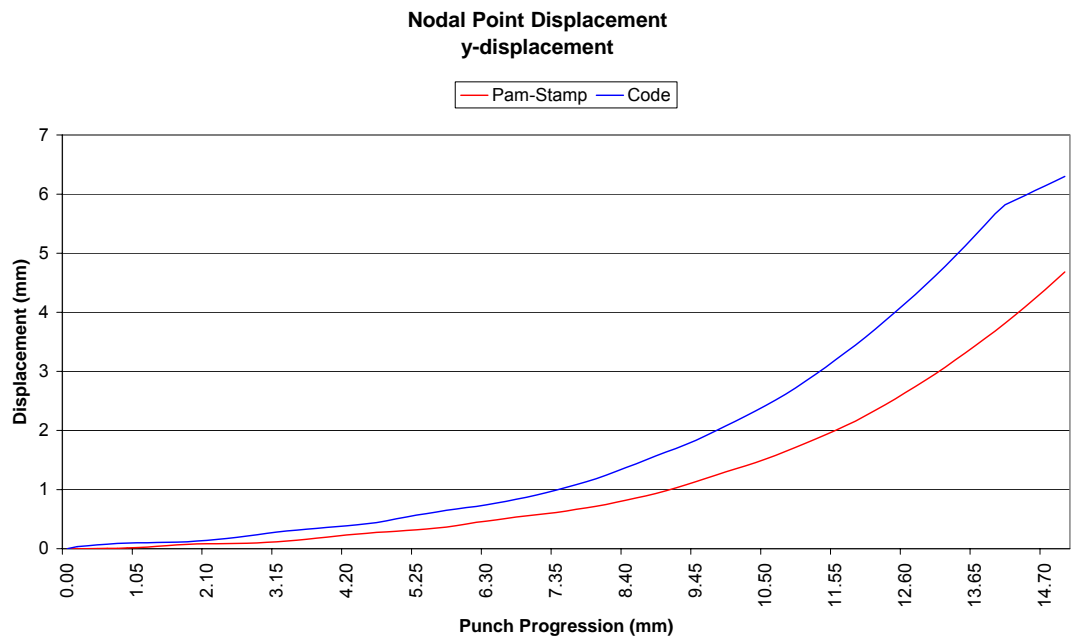


Figure 5.12 Displacement of node 2 in y-direction for 5 mm element size

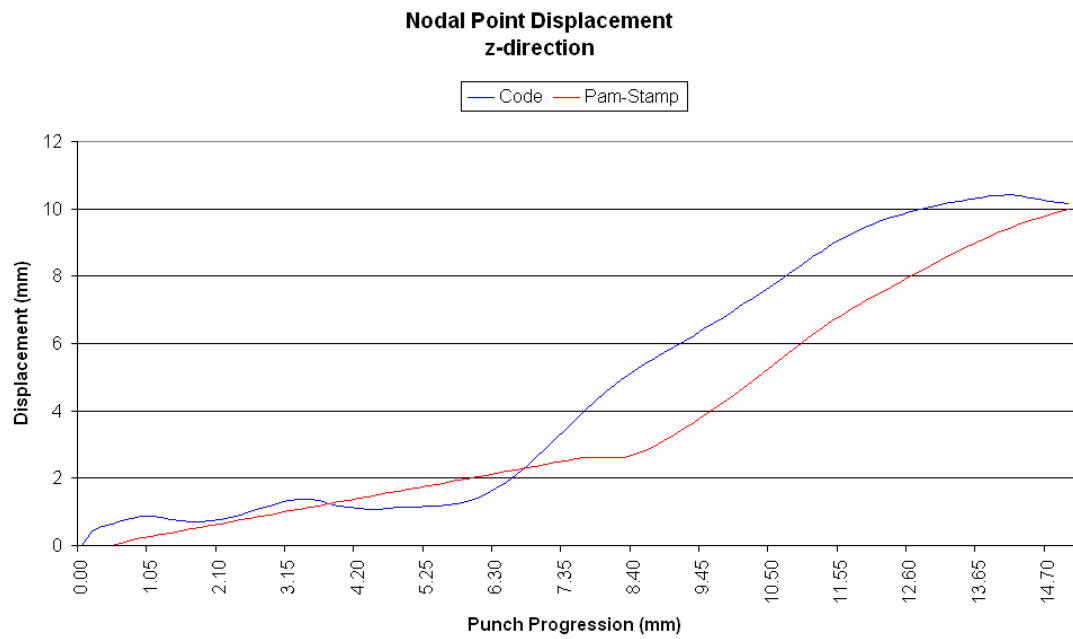


Figure 5.13 Displacement of node 3 in z-direction for 5 mm element size

5.6 Results for circular cup drawing (element size 3 mm)

In this simulation, a circular blank is drawn into a cylindrical cup. For modeling blank, element size is chosen to be 3 mm. No blank holder force is applied in order to analyze wrinkling. The drawing is completed as punch travels 15 mm. Analysis with the same conditions are conducted using PAM-STAMP. Nodal point displacement results of developed code at the nodes shown below are compared with the results of PAM-STAMP.

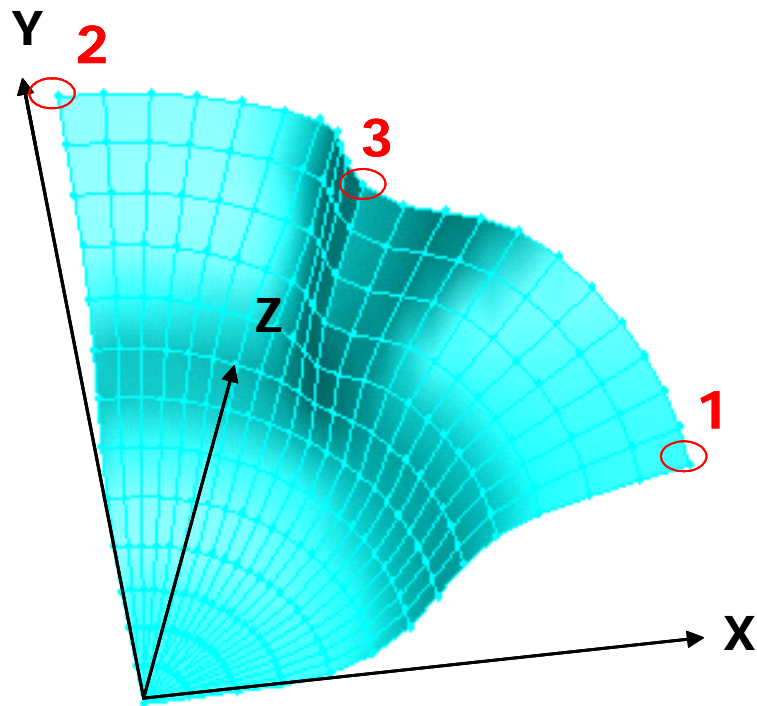


Figure 5.14 Orientation of circular blank with element size 3 mm

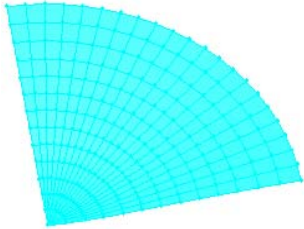
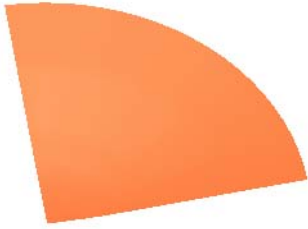
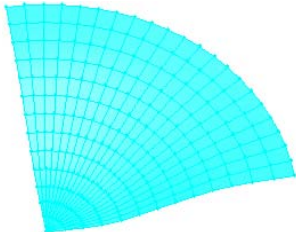
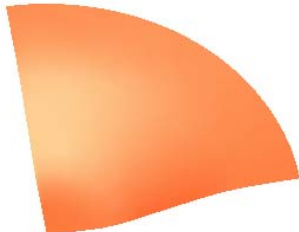
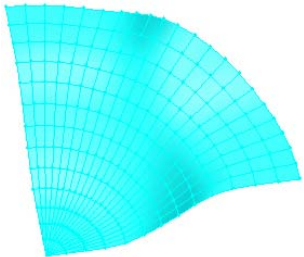
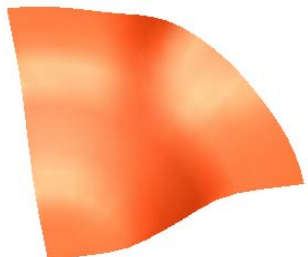
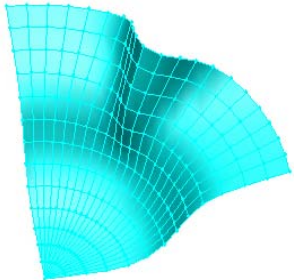
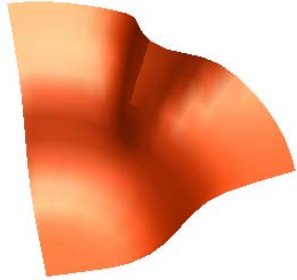
	Developed Code	PAM-STAMP
a)		
b)		
c)		
d)		

Figure 5.15 Deformed shapes at a) 1mm b) 5mm c) 10mm d) 15mm drawing depths

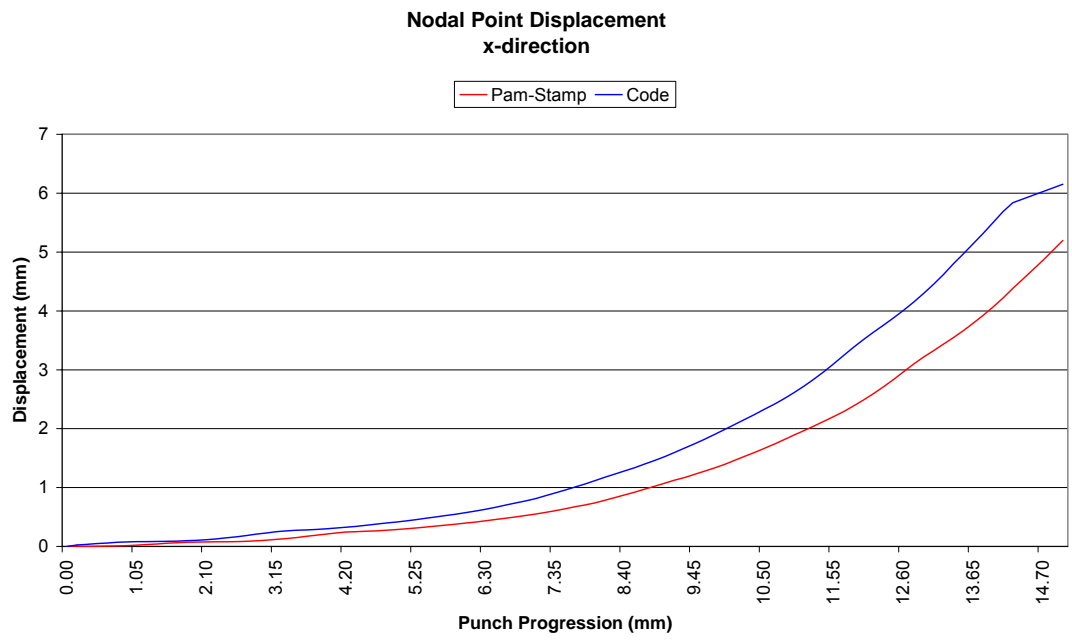


Figure 5.16 Displacement of node 1 in x-direction for 3 mm element size

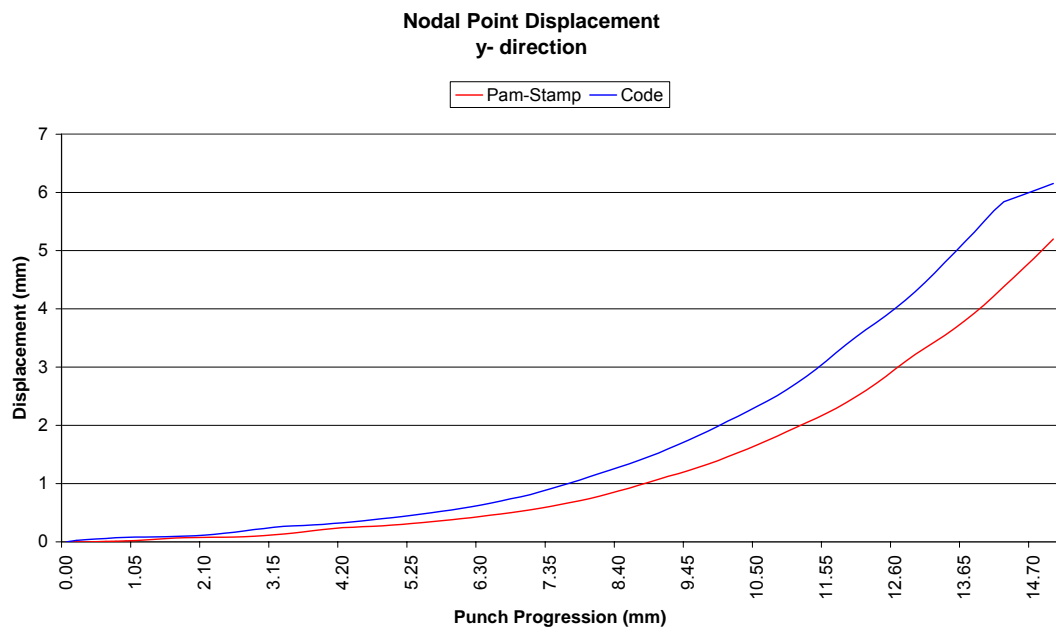


Figure 5.17 Displacement of node 2 in y-direction for 3 mm element size

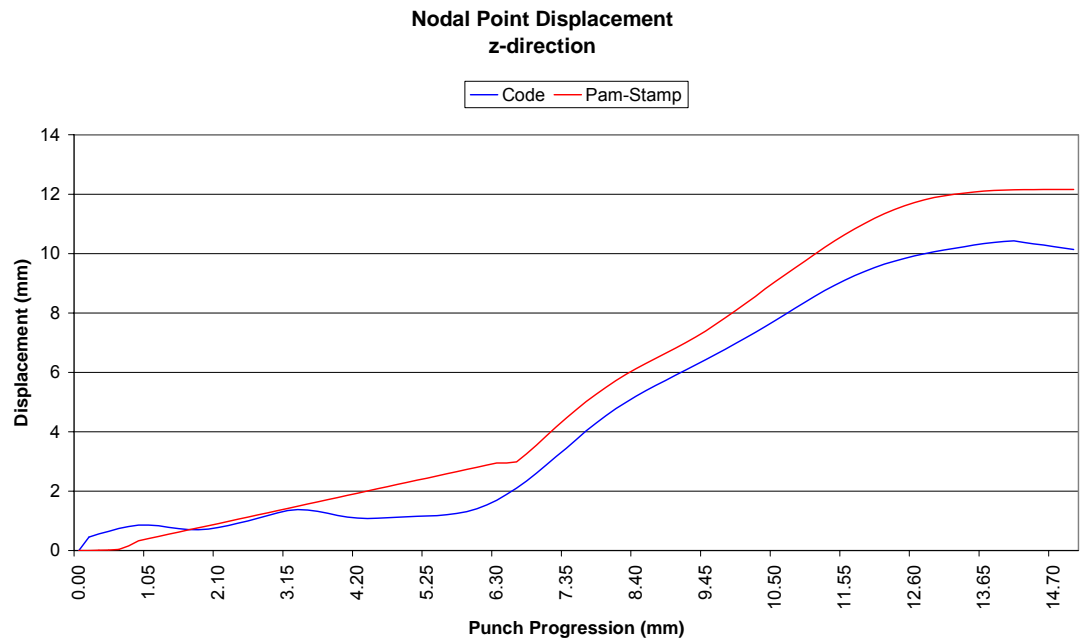


Figure 5.18 Displacement of node 3 in z-direction for 3 mm element size

5.7 Results for circular cup drawing (element size 2 mm)

In this simulation, a circular blank is drawn into a cylindrical cup. For modeling blank, element size is chosen to be 5 mm. No blank holder force is applied in order to analyze wrinkling. The drawing is completed as punch travels 15 mm. Analysis with the same conditions are conducted using PAM-STAMP. Nodal point displacement results of developed code at the nodes shown below are compared with the results of PAM-STAMP.

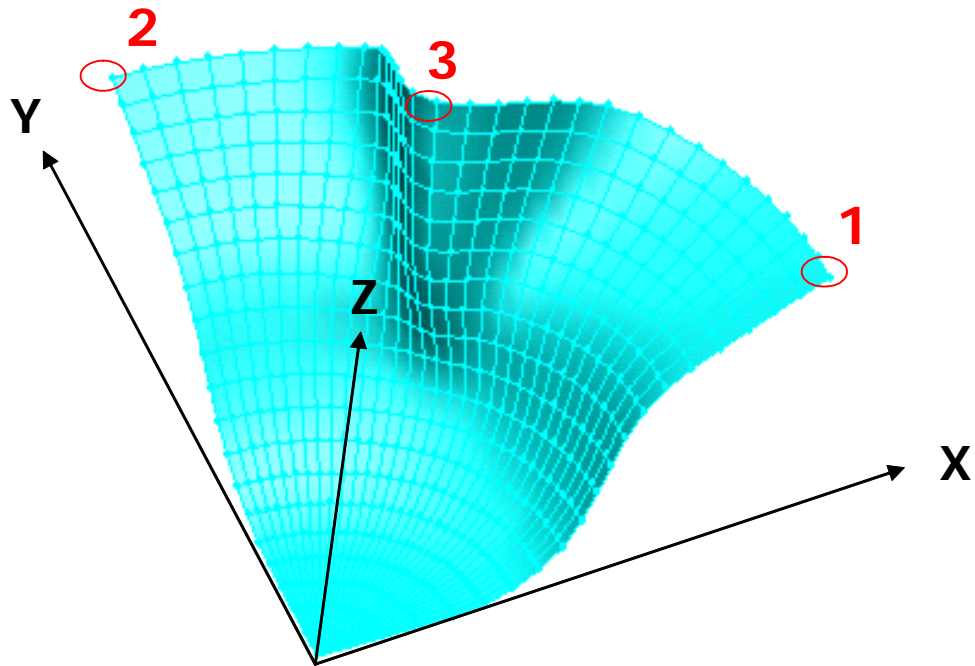


Figure 5.19 Orientation of circular blank with element size 2 mm

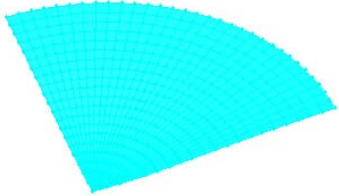

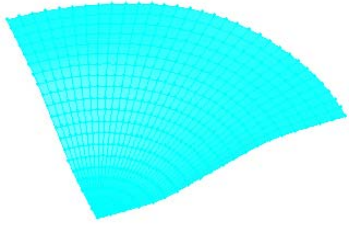
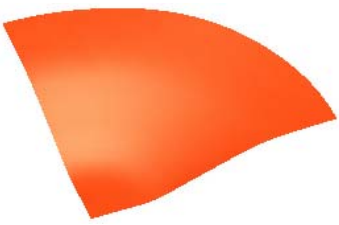
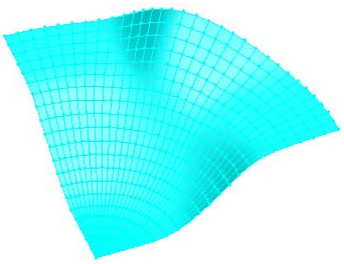
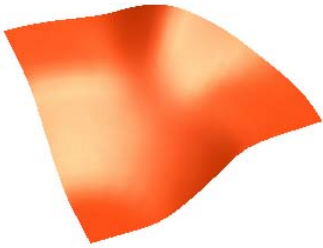
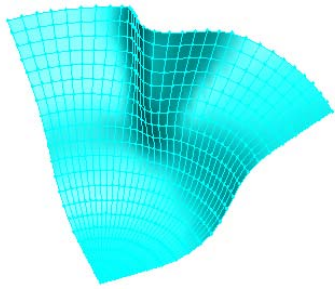
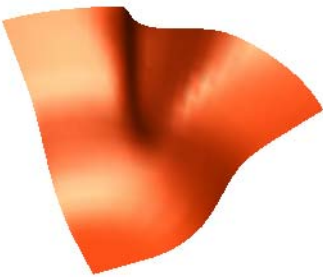
	Developed Code	PAM-STAMP
a)		
b)		
c)		
d)		

Figure 5.20 Deformed shapes at a) 1mm b) 5mm c) 10mm d) 15mm drawing depths

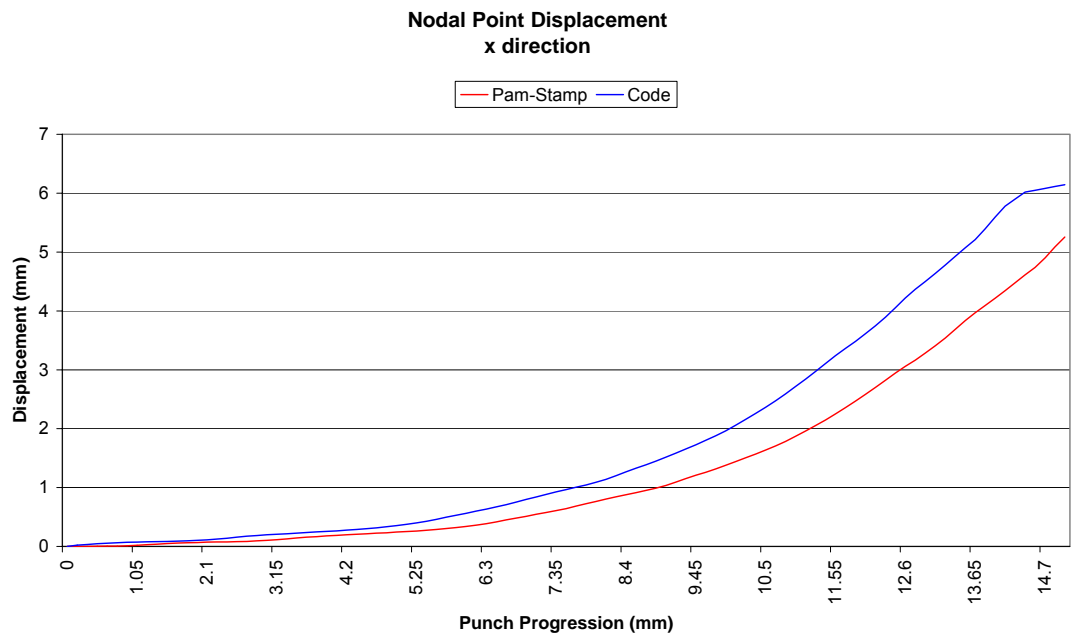


Figure 5.21 Displacement of node 1 in x-direction for 2 mm element size

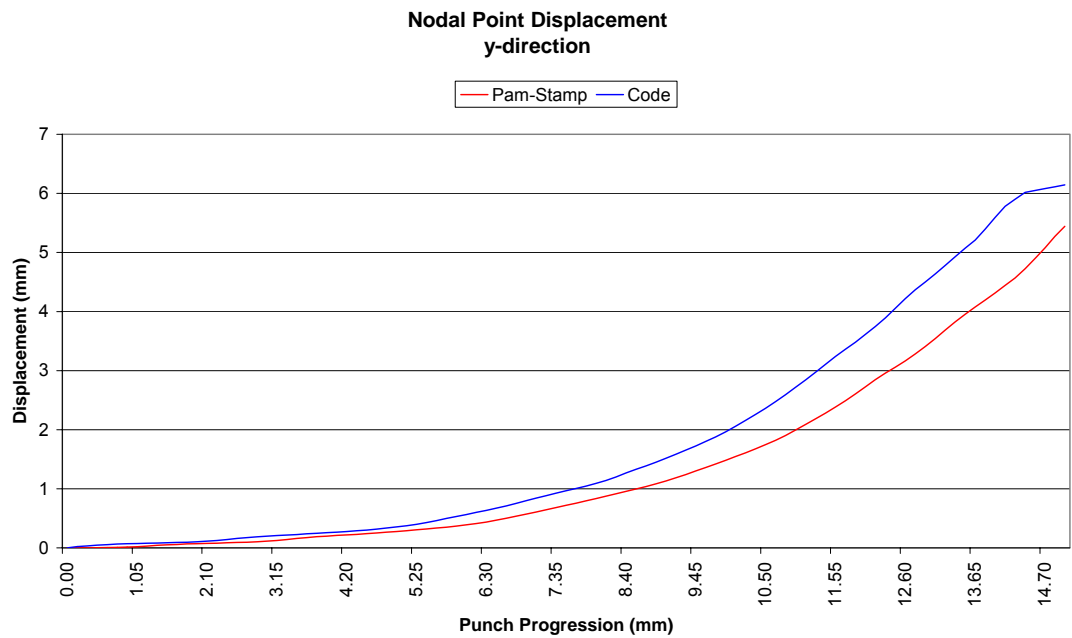


Figure 5.22 Displacement of node 2 in y-direction for 2 mm element size

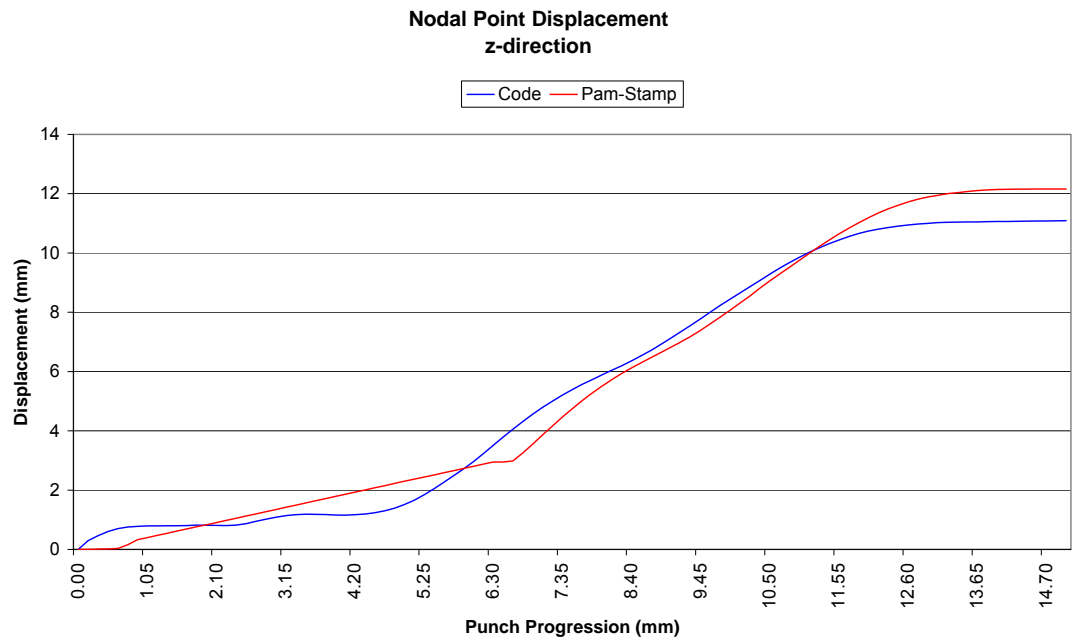


Figure 5.23 Displacement of node 3 in z-direction for 2 mm element size

5.8 Results for circular cup drawing (element size 1 mm)

In this simulation, a circular blank is drawn into a cylindrical cup. For modeling blank, element size is chosen to be 1 mm. No blank holder force is applied in order to analyze wrinkling. The drawing is completed as punch travels 15 mm. Analysis with the same conditions are conducted using PAM-STAMP. Nodal point displacement results of developed code at the nodes shown below are compared with the results of PAM-STAMP.

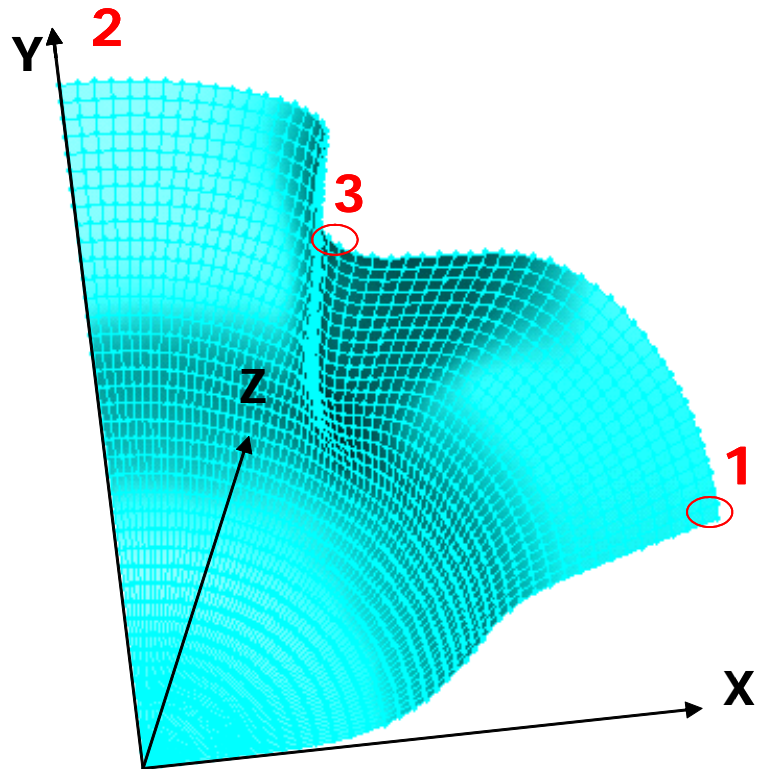


Figure 5.24 Orientation of circular blank with element size 1 mm

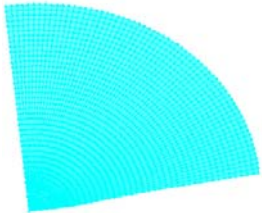

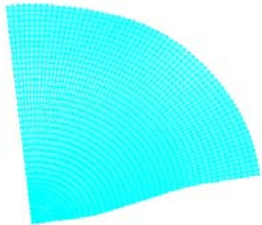

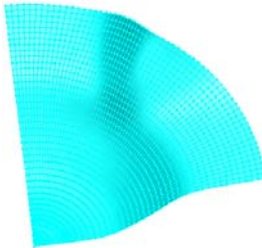
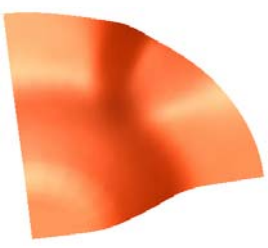
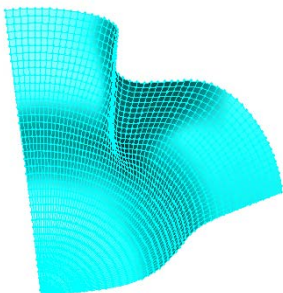
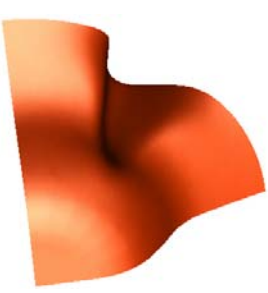
	Developed Code	PAM-STAMP
a)		
b)		
c)		
d)		

Figure 5.25 Deformed shapes at a) 1mm b) 5mm c) 10mm d) 15mm drawing depths

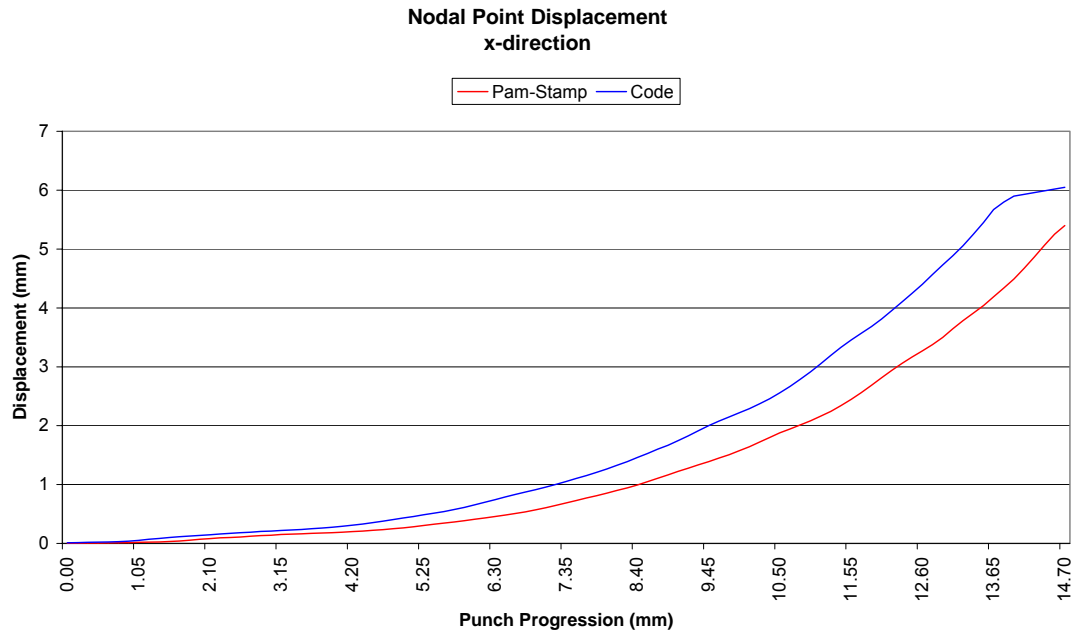


Figure 5.26 Displacement of node 1 in x-direction for 1 mm element size

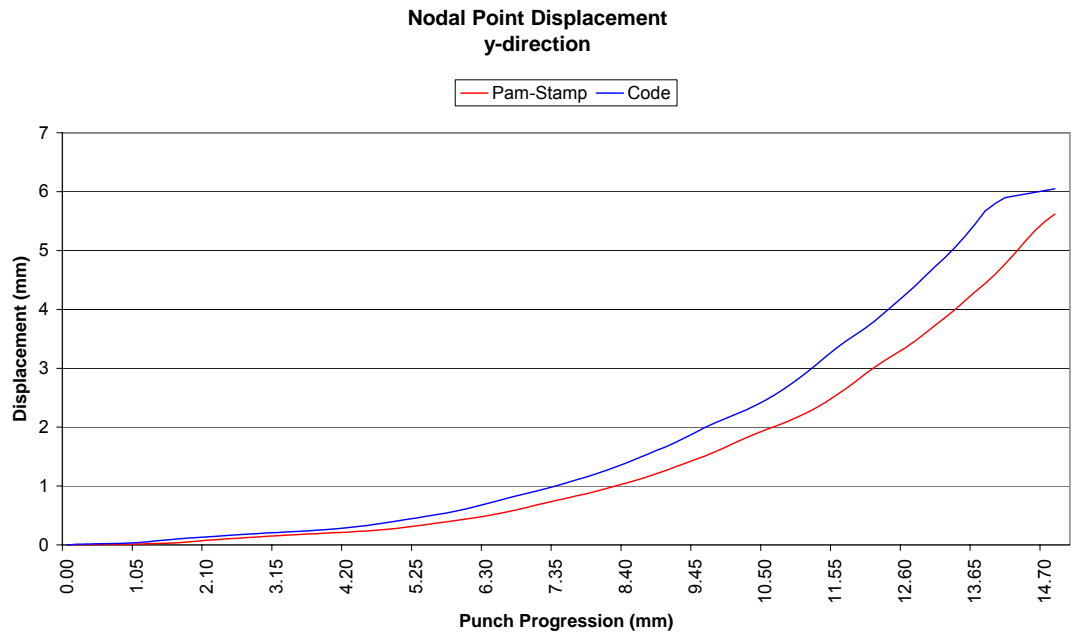


Figure 5.27 Displacement of node 2 in y-direction for 1 mm element size

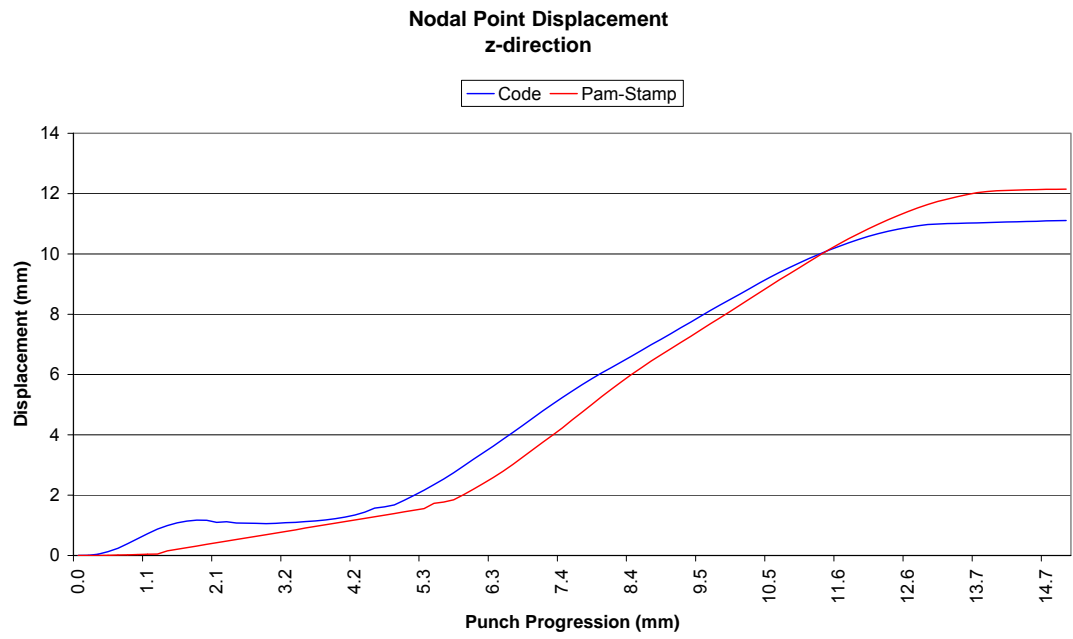


Figure 5.28 Displacement of node 3 in z-direction for 1 mm element size

5.9 Results for square cup drawing (element size 3mm)

In this simulation, a square blank is drawn into a square cup. For modeling blank, element size is chosen to be 3 mm. No blank holder force is applied in order to analyze wrinkling. The drawing is completed as punch travels 15 mm. Analysis with the same conditions are conducted using PAM-STAMP. Nodal point displacement results of developed code at the nodes shown below are compared with the results of PAM-STAMP.

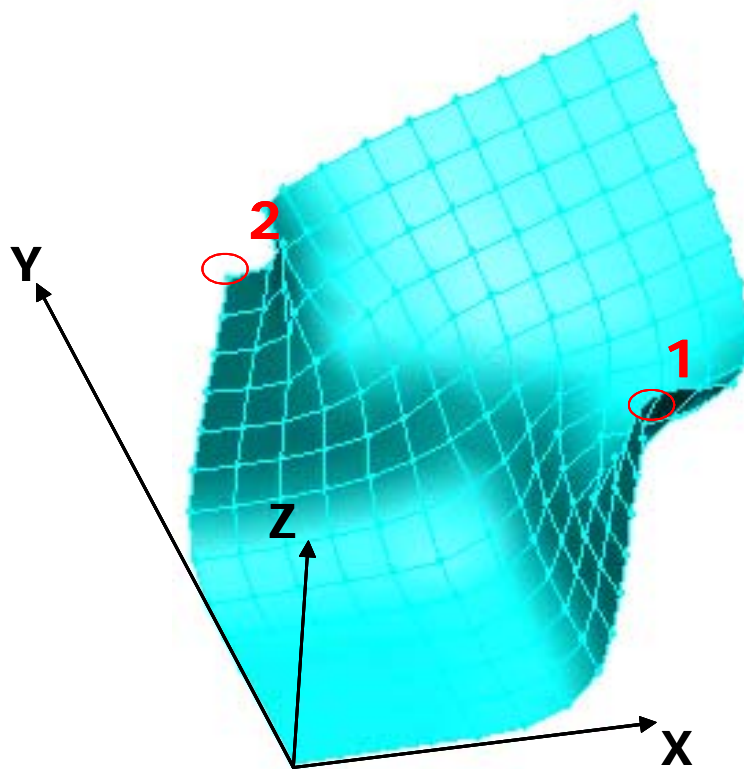


Figure 5.29 Orientation of square blank with element size 3 mm

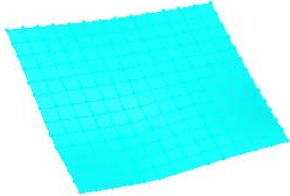
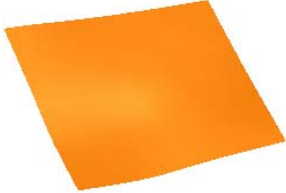
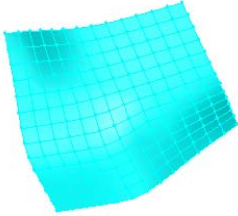
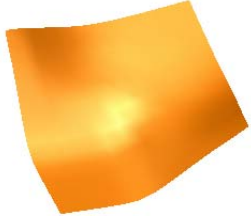
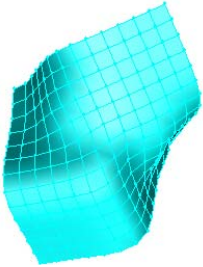

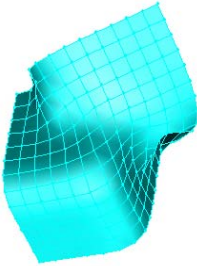

	Developed Code	PAM-STAMP
a)		
b)		
c)		
d)		

Figure 5.30 Deformed shapes at a) 1mm b) 5mm c) 10mm d) 15mm drawing depths

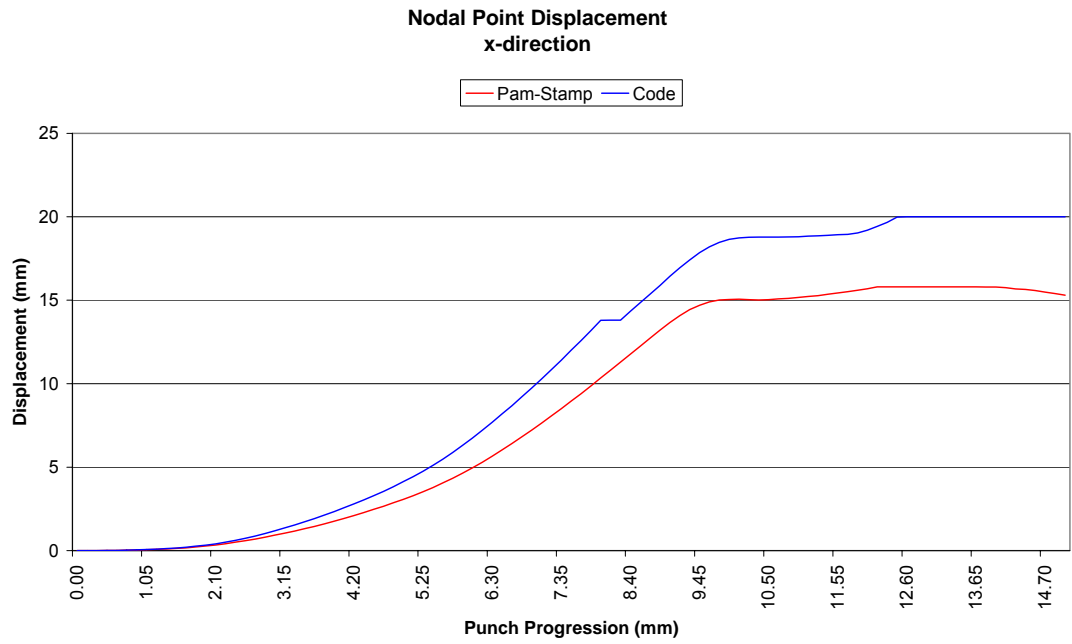


Figure 5.31 Displacement of node 1 in x-direction for 3 mm element size

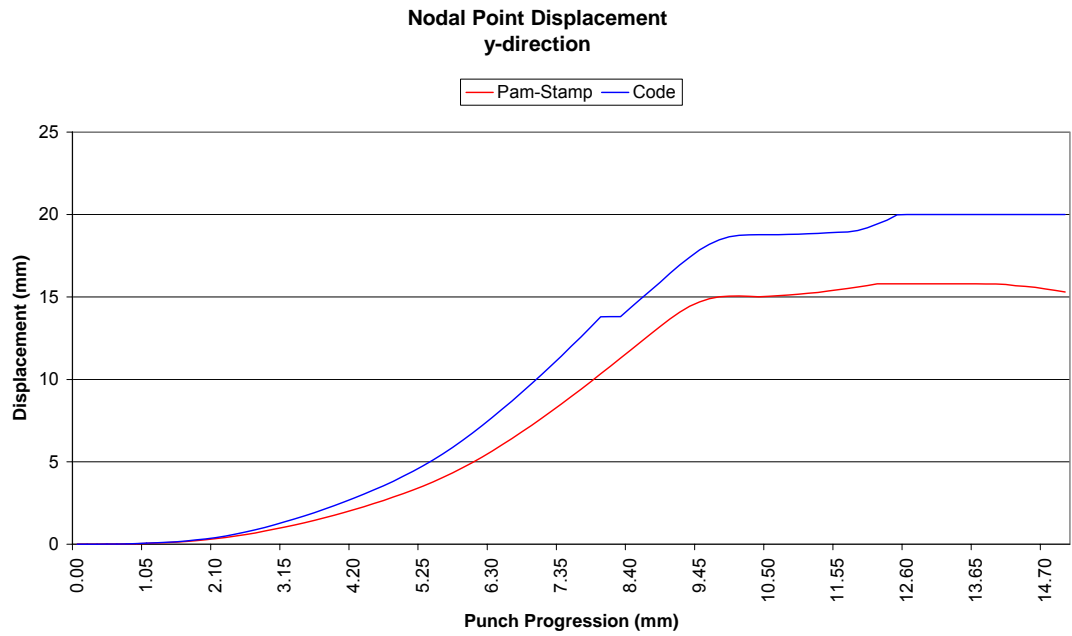


Figure 5.32 Displacement of node 2 in y-direction for 3 mm element size

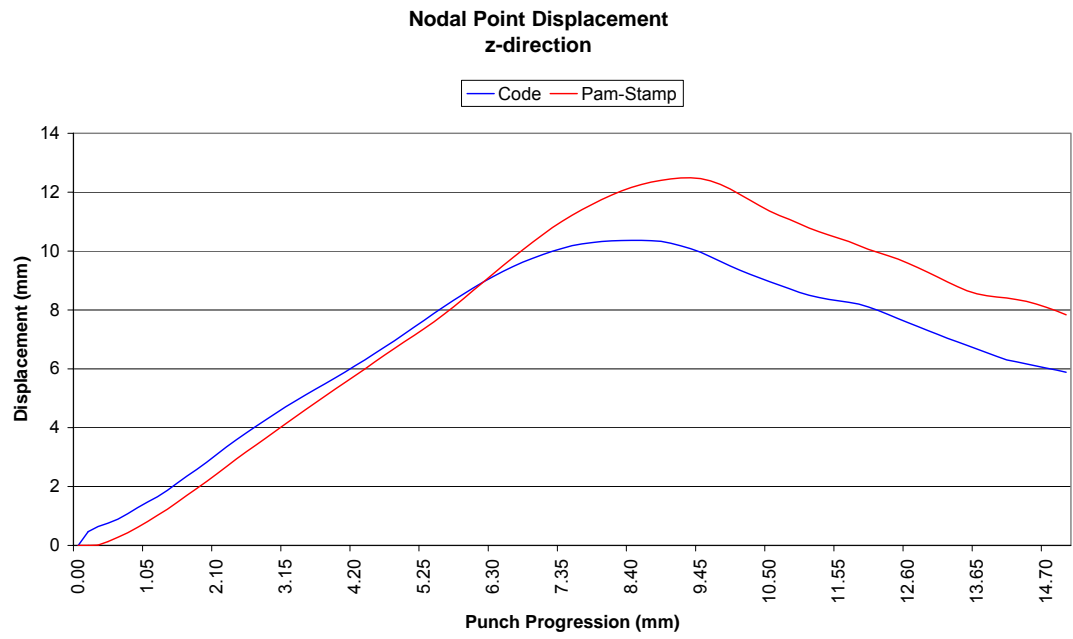


Figure 5.33 Displacement of node 2 in z-direction for 3 mm element size

5.10 Results for square cup drawing (element size 2mm)

In this simulation, a square blank is drawn into a square cup. For modeling blank, element size is chosen to be 2 mm. No blank holder force is applied in order to analyze wrinkling. The drawing is completed as punch travels 15 mm. Analysis with the same conditions are conducted using PAM-STAMP. Nodal point displacement results of developed code at the nodes shown below are compared with the results of PAM-STAMP.

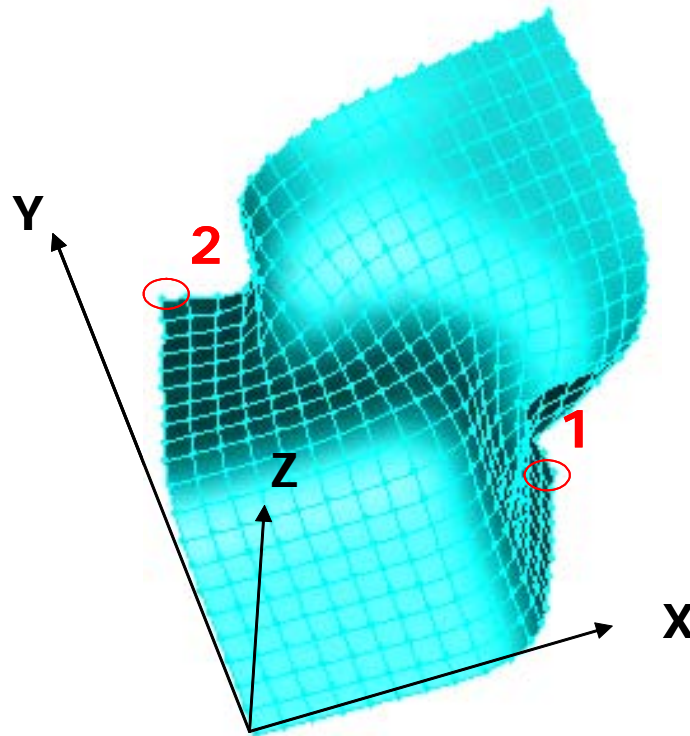


Figure 5.34 Orientation of square blank with element size 2 mm

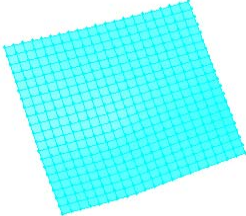

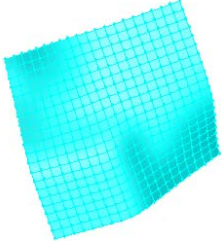

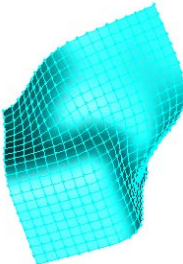

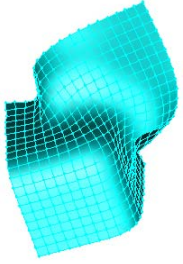

	Developed Code	PAM-STAMP
a)		
b)		
c)		
d)		

Figure 5.35 Deformed shapes at a) 1mm b) 5mm c) 10mm d) 15mm drawing depths

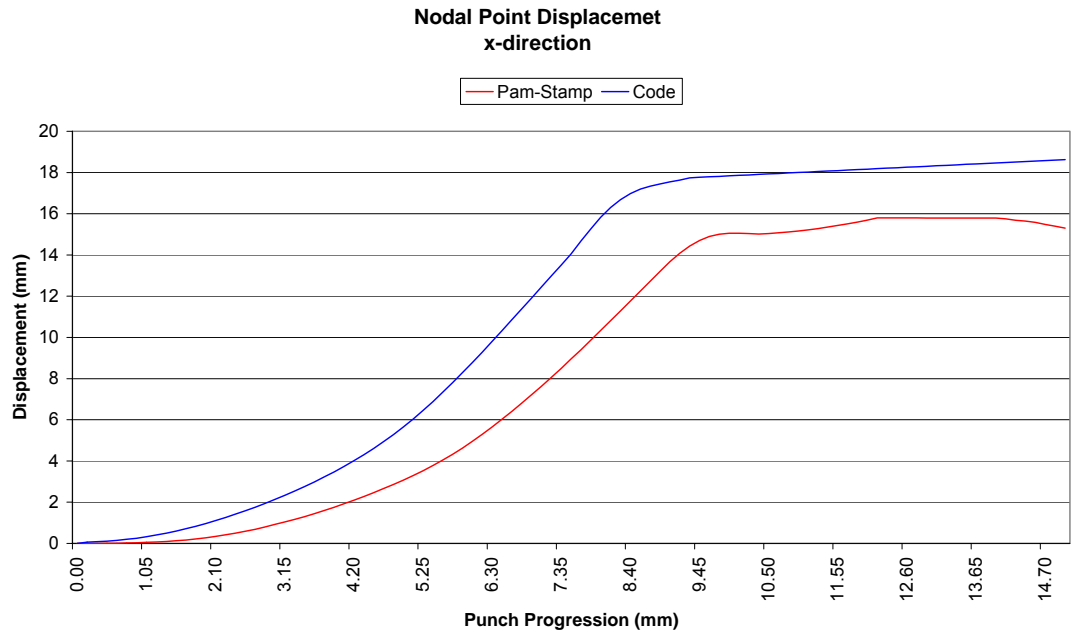


Figure 5.36 Displacement of node 1 in x-direction for 2 mm element size

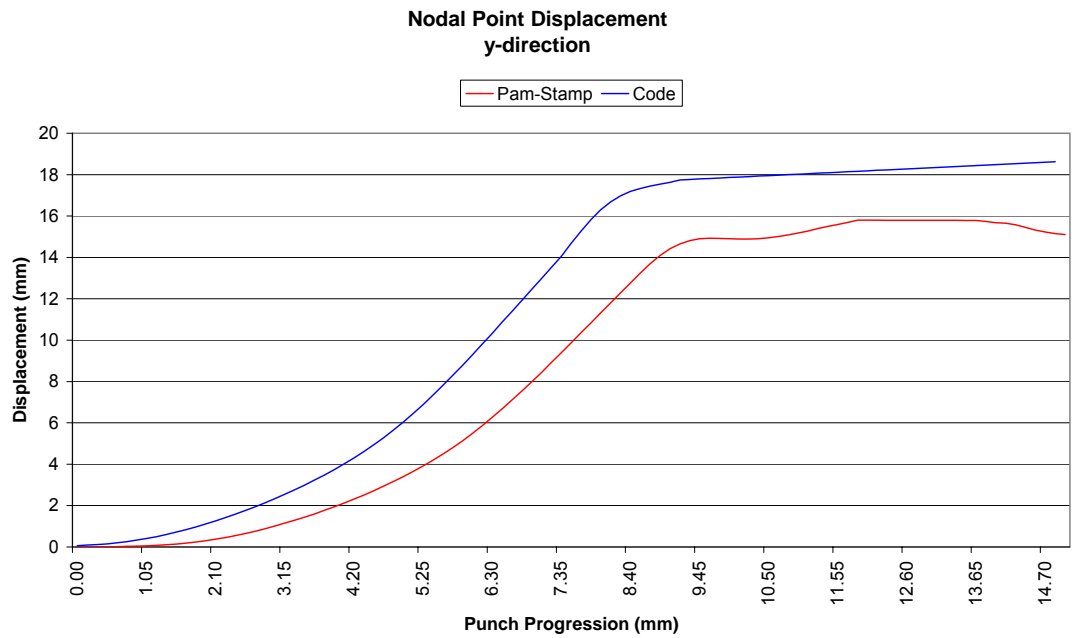


Figure 5.37 Displacement of node 2 in y-direction for 2 mm element size

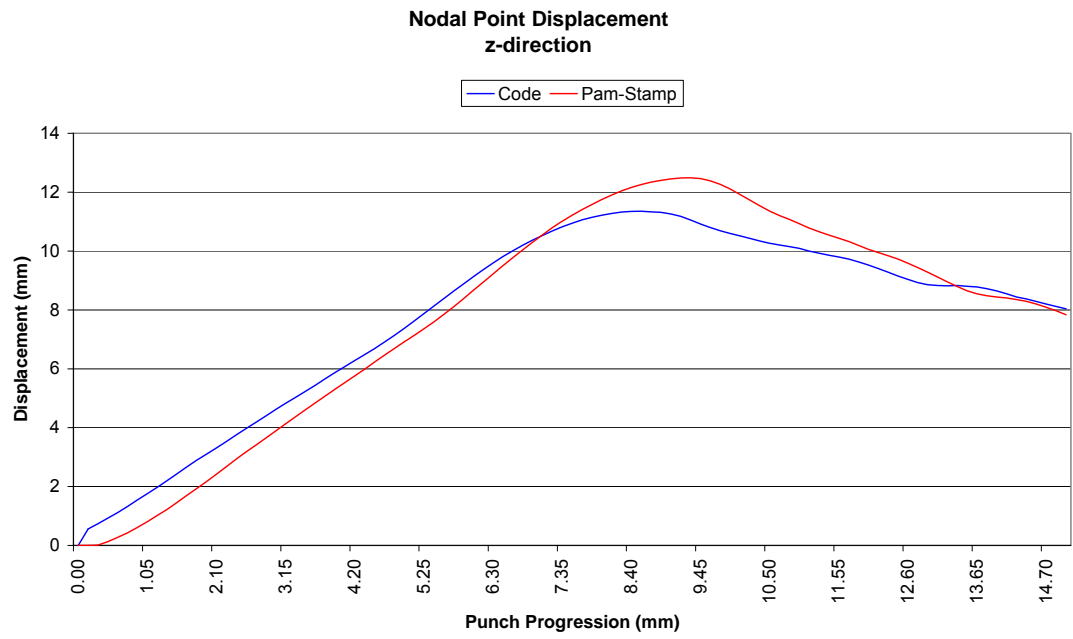


Figure 5.38 Displacement of node 2 in z-direction for 2 mm element size

5.11 Results for square cup drawing (element size 1mm)

In this simulation, a square blank is drawn into a square cup. For modeling blank, element size is chosen to be 1 mm. No blank holder force is applied in order to analyze wrinkling. The drawing is completed as punch travels 15 mm. Analysis with the same conditions are conducted using PAM-STAMP. Nodal point displacement results of developed code at the nodes shown below are compared with the results of PAM-STAMP.

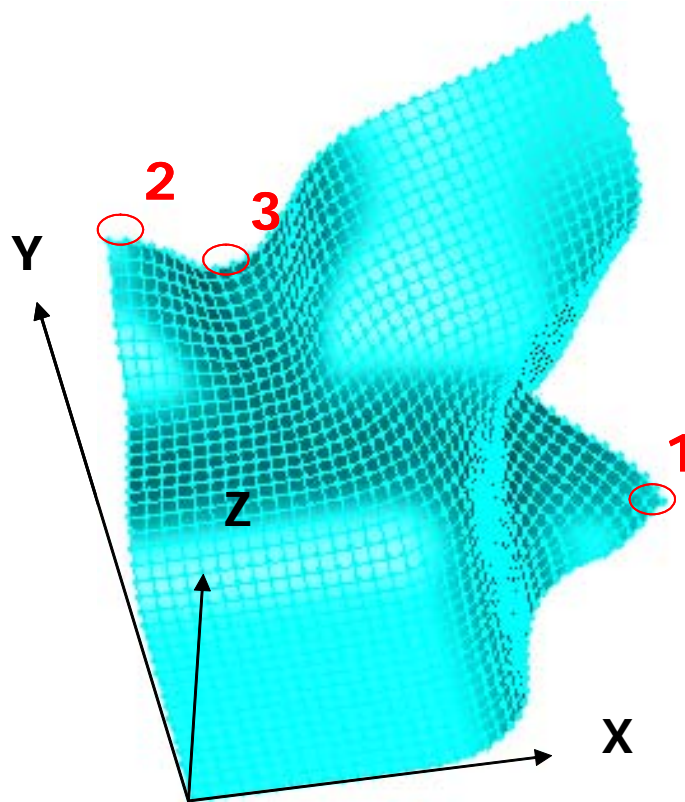


Figure 5.39 Orientation of square blank with element size 1 mm



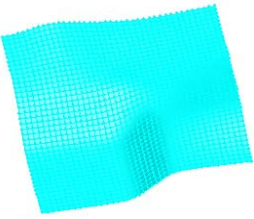
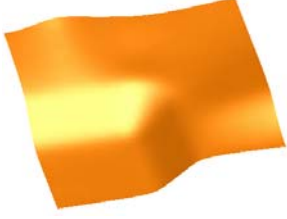
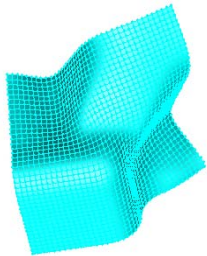

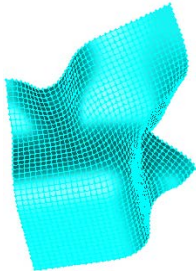
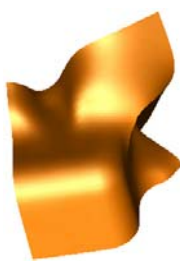
	Developed Code	PAM-STAMP
a)		
b)		
c)		
d)		

Figure 5.40 Deformed shapes at a) 1mm b) 5mm c) 10mm d) 15mm drawing depths

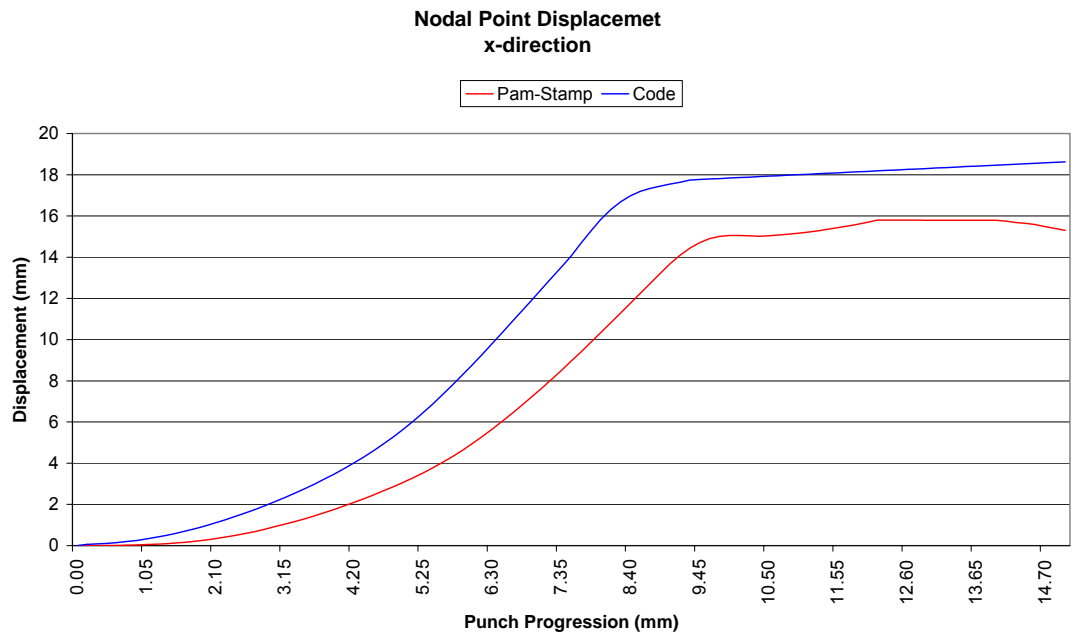


Figure 5.41 Displacement of node 1 in x-direction for 1 mm element size

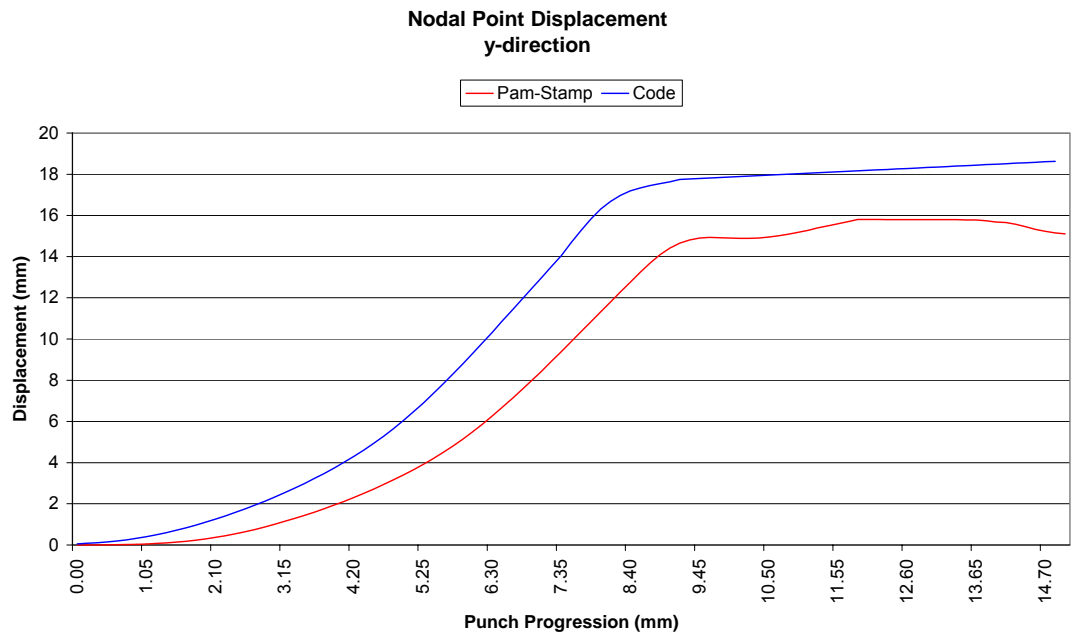


Figure 5.42 Displacement of node 2 in y-direction for 1 mm element size

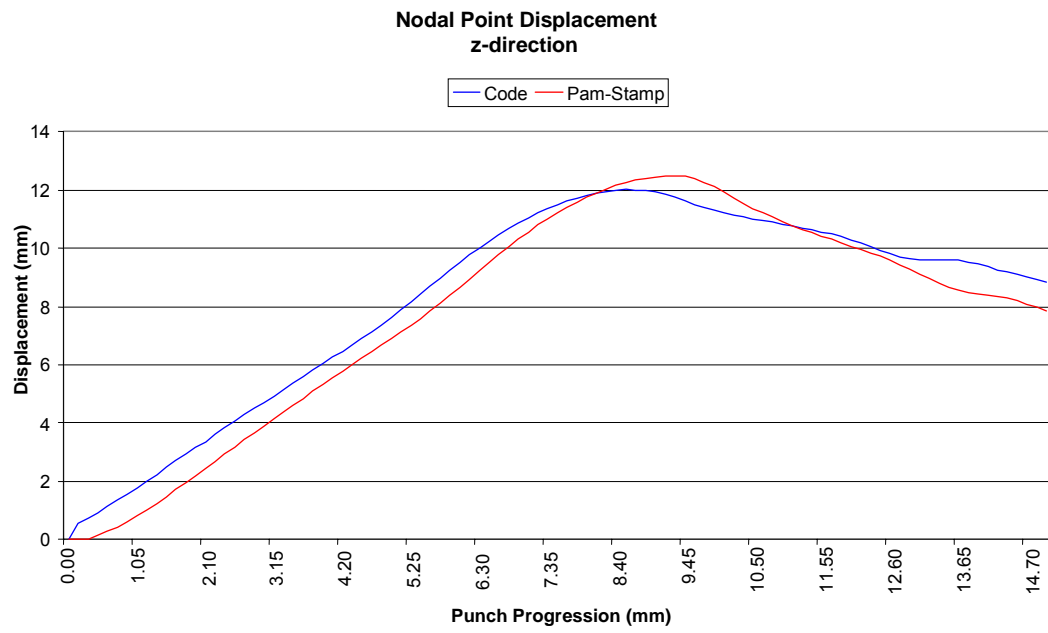


Figure 5.43 Displacement of node 3 in z-direction for 1 mm element size

5.12 Comparison of square cup drawing case with experimental results

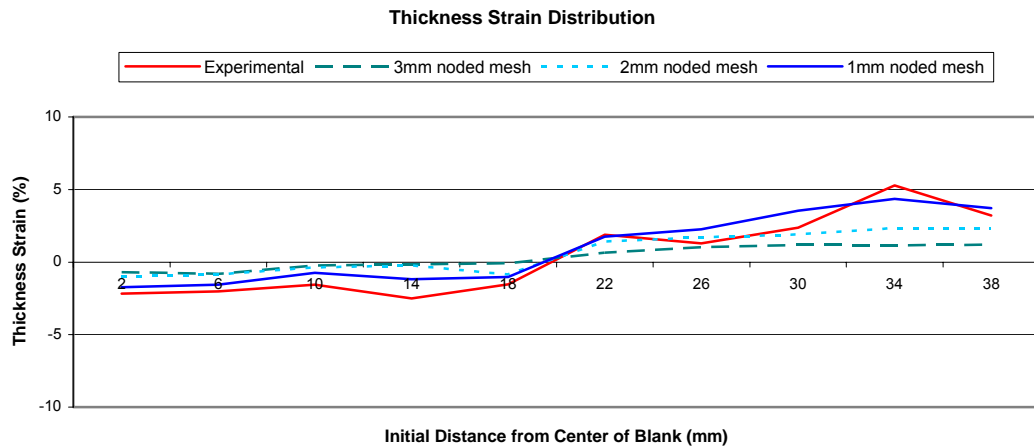


Figure 5.44 Thickness strain distribution along line connecting center of blank and midpoint of side at 4 mm drawing depth

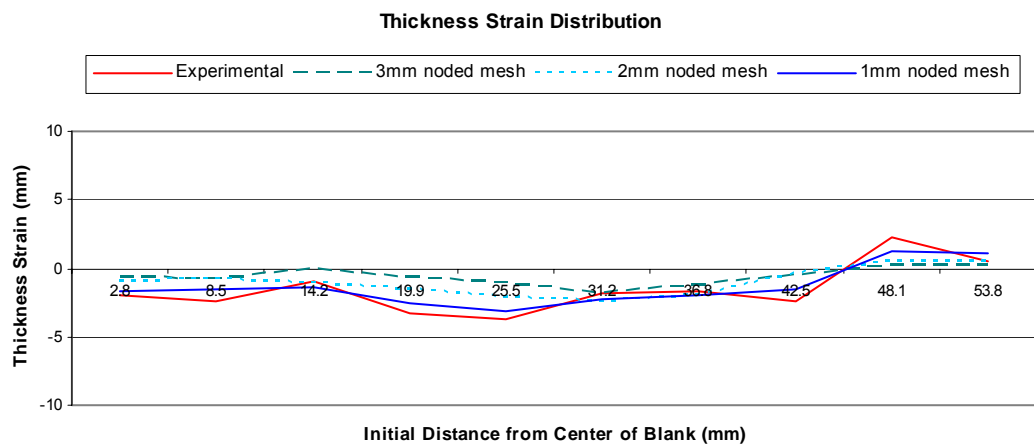


Figure 5.45 Thickness strain distribution along diagonal line at 4 mm drawing depth

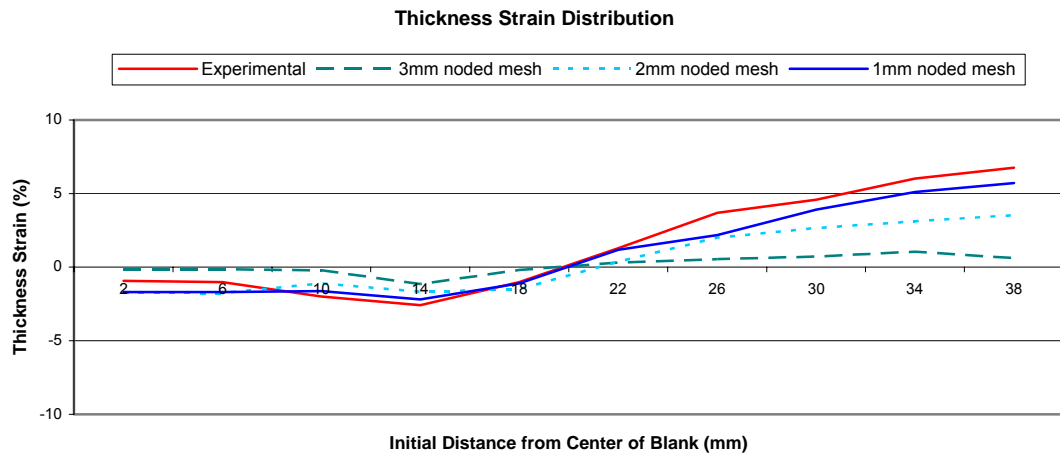


Figure 5.46 Thickness strain distribution along line connecting center of blank and midpoint of side at 10.5 mm drawing depth

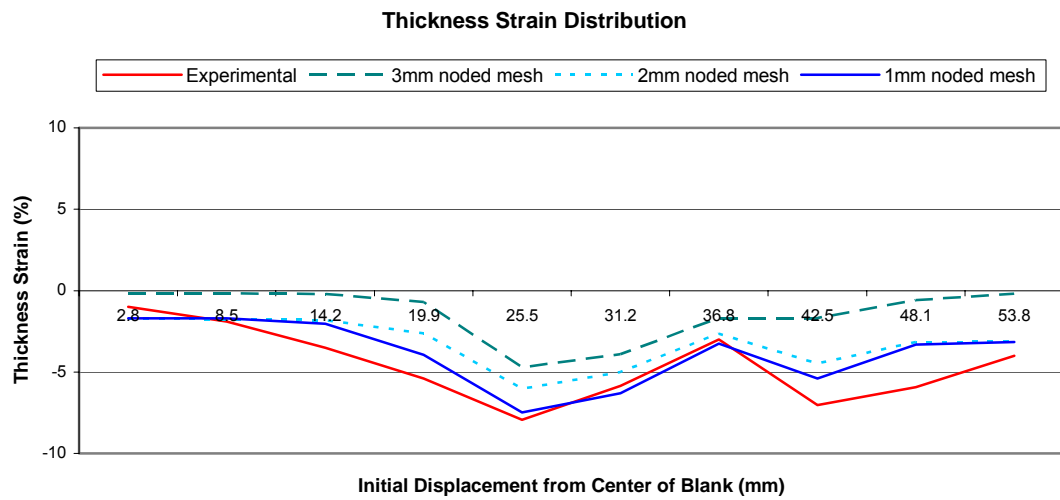


Figure 5.47 Thickness strain distribution along diagonal line at 10.5 mm drawing depth

5.13 Simulations with changing blank holder load

In these simulations, a square blank is drawn into a square cup. For modeling blank, element size is chosen to be 1 mm. Changing blank holder force is applied in order to analyze how wrinkle number change with increasing force and at what force level wrinkling occurrence stops. The drawing is completed as punch travels 15 mm for all simulations. Applied blank holder forces are 25 kgf, 50 kgf, 100 kgf, 150 kgf, 200 kgf and 215 kgf.

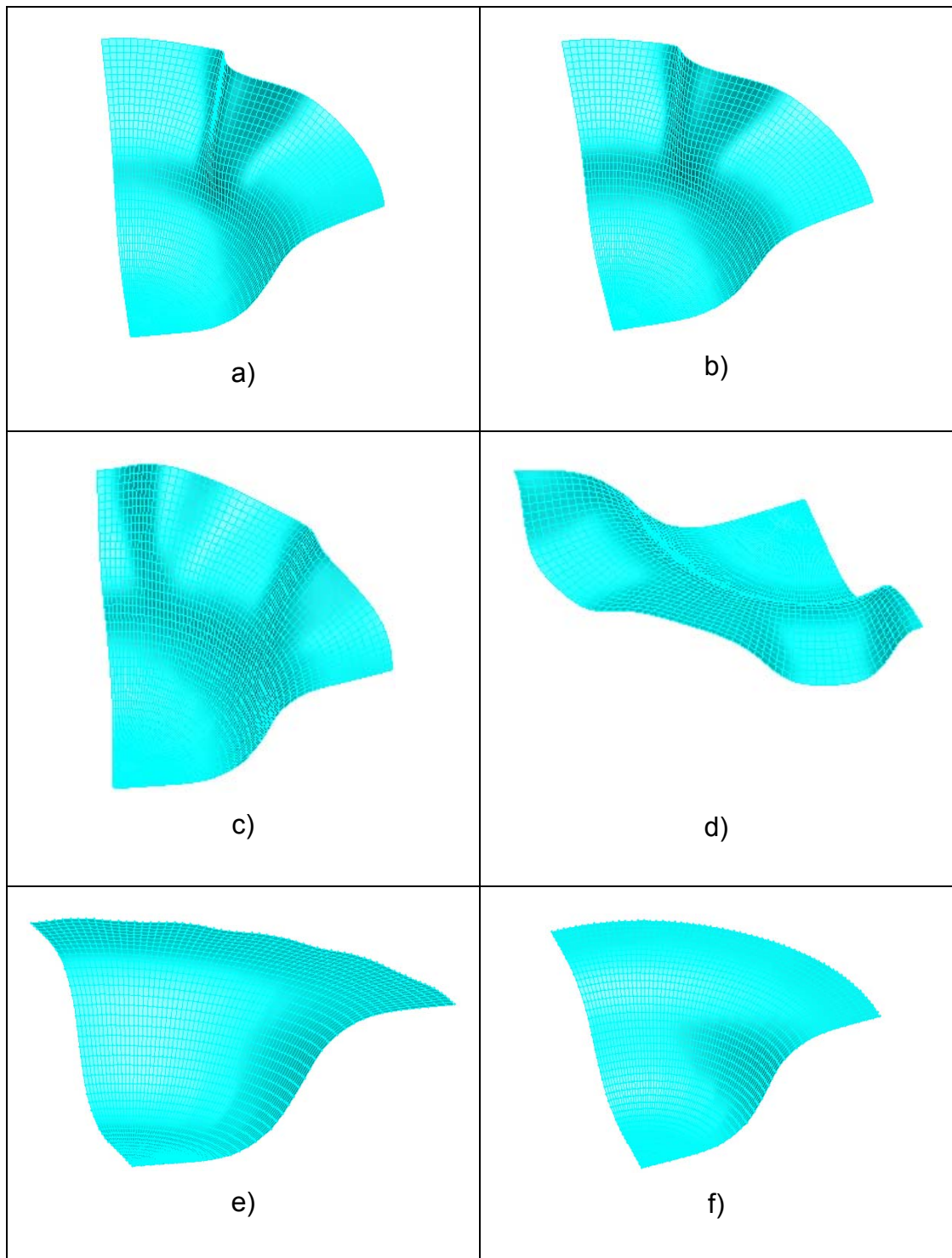


Figure 5.48 Deformed shapes at 15 mm drawing depth for a) 25kgf b) 50 kgf
c) 100 kgf d) 150 kgf e) 200 kgf f) 215 kgf

CHAPTER 6

DISCUSSION

In this study, a finite element program is developed to analyze the wrinkling behavior in deep-drawing operations. Tool and blank geometry are needed to be input to the program. The program calculates the displacements of nodes of blank. Using these displacements, incremental, total and effective strains are calculated. According to constitutive laws, incremental, total, deviatoric, mean and equivalent stresses are found in post calculation phase. Results of nodal displacements are rearranged to be displayed in ANSYS.

The program is tested for square and circular cup drawing with different finite element meshes. The results are compared with both experimental findings and the results of the commercial program PAM-STAMP. Comparison with PAM-STAMP is based on nodal displacement values, whereas the experimental results are compared according to the strains in thickness direction.

All simulations are carried out using $\frac{1}{4}$ symmetry. Appropriate boundary conditions are applied at symmetry planes. The material properties for simulations are chosen to represent the material properties of stainless steel used in the experiments. These values are presented by Şenalp [40] according to conducted tests during his Ph.D. study.

A total of 11 runs are conducted, 4 for circular cup drawing, 4 for square cup drawing and 3 for square cup drawing with blank-holder. 4 different element size is used for meshing: 1 mm, 2 mm, 3 mm and 5 mm.

Considering the results for circular cup drawing, it is observed that as element size decreases, solutions of both developed code and PAM-STAMP converges. As represented in Chapter 5, results obtained are in good agreement with the commercial program. In all mesh types, this agreement can be observed, however, with decreasing mesh size the results become closer to converging values.

In square cup drawing, however, the run performed with 5 mm element size did not give reasonable results. The main reason for this is thought to be the coarse mesh. 5 mm element size is very big to simulate the behavior of material. Actually, this can be understood observing the figures of 3 mm element sized mesh results. Even with this mesh size, sharp corners take place in blank. Therefore it can be deduced that for simulation of square cup drawing using such tool geometry, 5 mm element size is much larger than suitable. The same conclusion can be reached for square cup drawing with blank-holder using same element size.

The results for square cup drawing with other element size, however are seem be in good agreement with result obtained from PAM-STAMP simulations. As in the circular cup drawing case, the results converge to same values as mesh size decreases.

Moreover, the results of developed code for square cup drawing are also compared with the experimental results. This comparison is based on thickness strains. The experimental values are available for two cup heights, 6 mm and 7.5 mm. The thickness strains are measured along the line

connecting the center of blank and midpoint of side, and along the diagonal of blank for both cup heights.

In this comparison, the effect of mesh size on the results can be observed easier. As the mesh size decreases, the results of developed code become much closer to the experimental values. The results are in good agreement especially for element sizes 2 mm and 1 mm.

The results obtained for square cup drawing with blank-holder are also compared with the experimental findings. The comparison is made at two cup drawing heights, 5 mm and 10 mm; and based on the thickness strain values. The values are measured on the diagonal line and the line connecting center of blank and midpoint of side on the experimental part. The appropriate values are considered from the developed code.

To find the necessary blank holder load to prevent wrinkling, several simulations are carried out with changing blank holder load. At the end of 6 simulations, it is found that a blank holder force of 215 kgf is enough to prevent wrinkling. The blank holder forces used in these simulations are 25 kgf, 50 kgf, 100 kgf, 150 kgf, 200 kgf and 215 kgf. For loads of 25 kgf and 50 kgf, it is observed that 4 wrinkles occur, where the amplitude is less for the latter load. For loads 100 kgf and 150 kgf, wrinkle number increases to 8, and again for the higher load amplitude is smaller. For load of 200 kgf, wrinkle number becomes 16. For load of 215 kgf, no wrinkle occurs. The number of wrinkles and magnitude of amplitude with increasing force is as expected.

The results are in good agreement with the experimental values. As the mesh size decreases results converge to the same values, and become closer with the experimental findings. Especially, the results of 1 mm noded mesh seem to be very accurate. However, the results for all meshes catch the general trend line seen in the experiments.

Although the numerical solutions obtained from the developed code seem to be in good agreement with both the experimental results and PAM-STAMP solutions, there are small discrepancies between them. There may be several causes for this. One of them is the friction model used. The Coulomb friction model is used, and it is taken constant everywhere. However, in the experiments it may not be possible to lubricate the all surfaces properly. Another reason may be the material model. The mechanical properties of materials is not possible to be modeled perfectly.

Experimentation procedure can be another factor for the differences between the numerical solutions and the experimental results. If there is a little misalignment of the punch, this results in nonsymmetrical parts.

There may also be some reading errors during the measurements on the drawn parts. This is one of the main reasons for discrepancies.

In spite of these effects, the solutions obtained by developed code seem to simulate the real conditions well enough. All cases are in good agreement with both experimental results and simulations of commercial program PAM-STAMP.

CHAPTER 7

CONCLUSION

As a conclusion, the study based on explicit formulation of time step integration for the analysis of deep drawing operation is successfully finished. The explicit finite element code is generated using C++ programming language. Axisymmetric blanks are defined using quadrilateral shell elements with 4 nodes and 5 d.o.f s at each node. Dynamic equilibrium equations with the given boundary conditions are constructed. Gaussian quadrature technique is used for numerical integrations. Isotropic elasto-plastic material model with Von Mises yield criterion is used. Updated Lagrangian formulation is adopted to calculate displacements. Stresses are related to strains by constitutive laws. Contact algorithm is developed using penalty function method. The analysis is made for deep drawing of square and circular cups without the blank-holder. Results are compared with the available experiments and results of commercial program PAM-STAMP.

The behavior of sheet-metals for large strain and large displacement can efficiently be modeled with the developed code. Wrinkling experiments conducted by Şenalp [40] yield very similar results with the numerical results obtained from the developed code. The thickness strain variations obtained from the experiments and from developed code are in good agreement. The program can also simulate the metal forming operation with blank holder force application. The results obtained for drawing case with blank-holder applications are also in good agreement with experimental findings.

CHAPTER 8

SUGGESTIONS FOR FUTURE WORK

Throughout the study it is observed that some of the areas can further be investigated and developed:

- Wrinkling as a function of blank holder load can be attempted.
- Effect of drawbead on wrinkling can be investigated.
- Investigations on nonsymmetric workpieces can be conducted.
- Different element models can be developed.
- Residual stress prediction can be attempted.
- Anisotropy can be included in material modeling.
- Strain rate effect can be taken into account.
- Redrawing of the parts can be considered.
- Remeshing can be applied.
- Variable blank holder load can be applied.

REFERENCES

- [1] Johnson W., Mellor P.B., "Engineering Plasticity", Ellis Horwood Ltd., 1983.
- [2] Kaftanoğlu B., "Plastic Analysis of Flange Wrinkling in Axisymmetrical Deep-Drawing". Proceedings of the 21st International Machine Tool Design and Research Conference, 1980, pp.21–28.
- [3] Ramaekers J.A.H, de Winter A., Kessels M.W.H., "Deepdrawability of a Round Cylindrical Cup", IDDRG'94, 1994, pp.403–412.
- [4] Kang S., Im S., "Finite Element Analysis of Wrinkling Membranes", Journal of Applied Mechanics, Vol.64, June 1997, pp.263–269.
- [5] Cao J., Boyce M.C., "A Predictive Tool for Delaying Wrinkling and Tearing Failures in Sheet Metal Forming", Transactions of the ASME, Vol.119, October 1997, pp.354–365.
- [6] Park S.H., Yoon J.W., Yang D.Y., Kim Y.H., "Optimum Blank Design in Sheet Metal Forming by the Deformation Path Iteration Method", International Journal of Mechanical Sciences, Vol.41, 1999, pp.1217–1232.
- [7] Cao J., "Prediction of Plastic Wrinkling Using the Energy Method", Journal of Applied Mechanics, Vol.66, September 1999, pp.646–652.
- [8] Kawka M., Olejnik L., Rosochowski A., Sunaga H., Makinouchi A., "Simulation of Wrinkling in Sheet Metal Forming", Journal of Materials Processing Technology, Vol.109, 2001, pp.283–289.

- [9] Kim J.B., Yoon J.W., Yang D.Y., Barlat F., "Investigation into Wrinkling Behavior in the Elliptical Cup Deep Drawing Process by Finite Element Analysis Using Bifurcation Theory", *Journal of Material Processing Technology*, Vol.111, 2001, pp.170–174.
- [10] El-Morsy A., Manabe K., Kang D.B., Hwang J.K., "FE Analysis on Temperature and Deformation of Magnesium Alloy Sheet in Warm Deep-Drawing Process", *Proceedings of the 5th International Conference and Workshop on Numerical Simulation of 3D Sheet Forming Processes*, Vol.1, 2002, pp.171–176.
- [11] Nalawade V.V., Deshpande A.S., "Deep Drawing of Cylindrical Cups – An Improved, Dedicated Program and Its Validation", *Proceedings of the 5th International Conference and Workshop on Numerical Simulation of 3D Sheet Forming Processes*, Vol.1, 2002, pp.273–278.
- [12] Alves J.L., Oliveira M.C., Menezes L.F., "Study of the Influence of the Refinement of a 3–D Finite Element Mesh in Draw-In Ears and Wrinkles of a Deep Drawn Cylindrical Cup", *Proceedings of the 5th International Conference and Workshop on Numerical Simulation of 3D Sheet Forming Processes*, Vol.1, 2002, pp.301–306.
- [13] Cho J.W., Yang D.Y., "A Mesh Refinement Scheme for Sheet Metal Forming Analysis", *Proceedings of the 5th International Conference and Workshop on Numerical Simulation of 3D Sheet Forming Processes*, Vol.1, 2002, pp.307–312.
- [14] Selman A., Meinders T., Huétink J., van den Boogard A.H., "Comprehensive Adaptive Mesh Refinement in Wrinkling Prediction Analysis", *Proceedings of the 5th International Conference and Workshop on Numerical Simulation of 3D Sheet Forming Processes*, Vol.1, 2002, pp.355–359.
- [15] Lejeune A., Boudeau N., Gelin J.C., "Wrinkling Predictions in Metal Forming", *Proceedings of the 5th International Conference and Workshop on Numerical Simulation of 3D Sheet Forming Processes*, Vol.1, 2002, pp.549–555.
- [16] Nakamura Y., Ohata T., Nakamachi E., Katayama T., Ueda T., "Study of Optimum Drawbead Design in Sheet Metal Forming", *Proceedings of the 5th International Conference and Workshop on Numerical Simulation of 3D Sheet Forming Processes*, Vol.1, 2002, pp.585–590.

- [17] Weili X., Huibao W., Yuying Y., Wang Z.R., "A Simplified Method of Wrinkling Simulation", *Journal of Materials Processing Technology*, Vol.121, 2002, pp.19–22.

- [18] Cao J., Wang X., "An Analytical Model for Plate Wrinkling Under Tri-Axial Loading and Its Application", *International Journal of Mechanical Sciences*, Vol.42, 2000, pp.617–633.

- [19] Chu E., Xu Y., "An Elastoplastic Analysis of Flange Wrinkling in Deep Drawing Process", *International Journal of Mechanical Sciences*, Vol.43, 2001, pp.1421–1440.

- [20] Zeng X.M., Mahdavian S.M., "Critical Conditions of Wrinkling in Deep Drawing at Elevated Temperature", *Journal of Materials Processing Technology*, Vol.84, 1998, pp.38–46.

- [21] Morimoto H., Nakamachi E., "Elastic/Crystalline Viscoplastic Finite Element Analysis of the Deep Drawing Process, Taking Account of Texture Structure", *Furukawa Review*, No.18, 1999, pp.119–124.

- [22] Kim J.B., Yoon J.W., Yang D.Y., "Investigation into Wrinkling Behavior of Thin Sheets in the Cylindrical Cup Deep Drawing Process Using Bifurcation Theory", *International Journal for Numerical Methods in Engineering*, Vol.56, 2003, pp.1673–1705.

- [23] Nordlund P., Häggblad B., "Prediction of Wrinkle Tendencies in Explicit Sheet Metal-Forming Simulations", *International Journal for Numerical Methods in Engineering*, Vol.40, 1997, pp.4079–4095.

- [24] Kim J.B., Yang D.Y., Yoon J.W., Barlat F., "The Effect of Plastic Anisotropy on Compressive Instability in Sheet Metal Forming", *International Journal of Plasticity*, Vol.16, 2000, pp.649–676.

- [25] Wang X., Cao J., "On the Prediction of Side-Wall Wrinkling in Sheet Metal Forming Processes", *International Journal of Mechanical Sciences*, Vol.42, 2000, pp.2369–2394.

- [26] Cao J., Boyce M.C., "Wrinkling Behavior of Rectangular Plates under Lateral Constraints", *International Journal of Solids and Structures*, Vol.34, No.2, pp.153–176.

- [27] Correia J.P.M., Ferron G., "Wrinkling Predictions in the Deep-Drawing Process of Anisotropic Metal Sheets", *Journal of Material Processing Technology*, Vol.128, 2002, pp.178–190.
- [28] Wang X., Cao J., Li M., "Wrinkling Analysis in Shrink Flanging", *Journal of Manufacturing Science and Engineering*, Vol.123, August 2001, pp.426–432.
- [29] Hematian J., Wild P.M., "The Effects of Tooling Imperfections on the Initiation of Wrinkling in Finite Element Modeling of a Deep Drawing Process", *Journal of Engineering Materials and Technology*, Vol.123, October 2001, pp.442–446.
- [30] Xiong Z.Q., Xie L.S., "Study on the Theory and Application of the Energy Method for Analyzing Compressive Instability in Sheet Forming", *Journal of Materials Processing Technology*, Vol.129, 2002, pp.255–260.
- [31] Lee C., Cao J., "Shell Element Formulation of Multi-Step Inverse Analysis for Axisymmetric Deep Drawing Process", *International Journal for Numerical Methods in Engineering*, Vol.50, 2001, pp.681–706.
- [32] Evangelista S.H., Lirani J., Al-Qureshi H.A., "Implementing a Modified Marciniak-Kuczynski Model Using the Finite Element Method for the Simulation of Sheet Metal Deep Drawing", *Journal of Materials Processing Technology*, Vol.130–131, 2002, pp.135–144.
- [33] Cao J., Wang X., Mills F.J., "Characterization of Sheet Buckling Subjected to Controlled Boundary Constraints", *Journal of Manufacturing Science and Engineering*, Vol.124, August 2002, pp.493–501.
- [34] Cho J.W., Yang D.Y., Chung W.J., "A Simplified Approach for Incorporating the Thickness Stress in the Analysis of Sheet Metal Forming Using Shell Elements", *International Journal for Numerical Methods in Engineering*, Vol.53, 2002, pp.2311–2327.
- [35] Gantar G., Pepelnjak T., Kuzman K., "Optimization of Sheet Metal Forming Process by the Use of Numerical Simulations", *Journal of Materials Processing Technology*, Vol.130–131, 2002, pp.54–59.
- [36] Chuan-Taoa W., Kinzelb G., Altan T., "Failure and Wrinkling Criteria and Mathematical Modeling of Shrink Stretch Flanging Operations in

Sheet–Metal Forming”, Journal of Materials Processing Technology, Vol.53, Issues 3–4, September 1995, pp.759–780.

[37] Miseikeh C.H., “Wrinkling of Membranes, Plates and Shells”, Ph.D. Thesis, McGill University, Department of Civil Engineering and Applied Mechanics, Montréal, February 1997.

[38] Bathe K.J., “Finite Element Procedures in Engineering Analysis”, Prentice-Hall Inc., 1982.

[39] D. Banabic, H.J. Bunge, K. Pöhlandt, A.E. Tekkaya: “Formability of Metallic Materials”, Springer, Berlin, 2000

[40] Şenalp A.Z, “Computer–Aided Wrinkling Analysis of Non–Axisymmetric Parts in Sheet Metal Forming”, Ph.D Thesis, Middle East Technical University, Mechanical Engineering Department, Ankara, May 1998.